

Cell size and growth regulation in the *Arabidopsis thaliana* apical stem cell niche

Lisa Willis^{a,b,1}, Yassin Refahi^{a,1}, Raymond Wightman^a, Benoit Landrein^a, José Teles^a, Kerwyn Casey Huang^{b,c}, Elliot M. Meyerowitz^{a,d,e}, and Henrik Jönsson^{a,f,g,2}

^aThe Sainsbury Laboratory, University of Cambridge, Cambridge CB2 1LR, United Kingdom; ^bDepartment of Bioengineering, Stanford University, Stanford, CA 94305; ^cDepartment of Microbiology and Immunology, Stanford University School of Medicine, Stanford, CA 94305; ^dHoward Hughes Medical Institute, California Institute of Technology, Pasadena, CA 91125; ^eDivision of Biology and Biological Engineering 156-29, California Institute of Technology, Pasadena, CA 91125; ^fComputational Biology and Biological Physics, Lund University, 223 62 Lund, Sweden; and ^gDepartment of Applied Mathematics and Theoretical Physics, Centre for Mathematical Sciences, University of Cambridge, Cambridge CB3 0DZ, United Kingdom

Edited by Natasha V. Raikhel, Center for Plant Cell Biology, Riverside, CA, and approved November 3, 2016 (received for review October 11, 2016)

Cell size and growth kinetics are fundamental cellular properties with important physiological implications. Classical studies on yeast, and recently on bacteria, have identified rules for cell size regulation in single cells, but in the more complex environment of multicellular tissues, data have been lacking. In this study, to characterize cell size and growth regulation in a multicellular context, we developed a 4D imaging pipeline and applied it to track and quantify epidermal cells over 3–4 d in *Arabidopsis thaliana* shoot apical meristems. We found that a cell size checkpoint is not the trigger for G2/M or cytokinesis, refuting the unexamined assumption that meristematic cells trigger cell cycle phases upon reaching a critical size. Our data also rule out models in which cells undergo G2/M at a fixed time after birth, or by adding a critical size increment between G2/M transitions. Rather, cell size regulation was intermediate between the critical size and critical increment paradigms, meaning that cell size fluctuations decay by ~75% in one generation compared with 100% (critical size) and 50% (critical increment). Notably, this behavior was independent of local cell-cell contact topologies and of position within the tissue. Cells grew exponentially throughout the first >80% of the cell cycle, but following an asymmetrical division, the small daughter grew at a faster exponential rate than the large daughter, an observation that potentially challenges present models of growth regulation. These growth and division behaviors place strong constraints on quantitative mechanistic descriptions of the cell cycle and growth control.

cell size | cell growth | cell cycle | homeostasis | plant stem cells

How cells coordinate growth and division to achieve a particular cell size remains a fundamental question in biology. Our understanding of this basic property of cells is limited, in part, by the lack of quantitative data on cellular growth and size kinetics over multiple generations, especially in higher eukaryotes (1). Classical studies of cell size homeostasis focused on whether division occurred upon reaching a critical size or after a fixed time period has elapsed (2, 3). However, time-lapse studies of single-celled organisms spanning a range of bacteria (4–7) and the yeast *Saccharomyces cerevisiae* (8) have recently indicated that cell size is regulated by the addition of a fixed volume increment between divisions. Identification of the size regulation behavior constrains the set of feasible molecular scenarios for how growth and division are coordinated with the cell cycle (8–10). In multicellular tissues, the loss of growth and division/cell cycle coordination could have an impact on the organism's development, yet, to the best of our knowledge, cell growth and size kinetics have never before been measured over generations in a tissue context. The experimental challenges are particularly acute because interdivision times are often on the order of tens of hours, cells have a diversity of shapes necessitating digital reconstruction in three dimensions to measure size accurately, and tissues are often difficult to access for imaging while keeping the organism alive. Further, the assumption, central to previous quantitative

studies, of a fixed environment in which homeostasis is achieved, is generally invalid in multicellular tissues, where patterns of cellular differentiation can modulate growth and division.

The *Arabidopsis thaliana* shoot apical meristem (SAM) is a multicellular tissue whose central zone harbors stem cells that proliferate throughout the plant's life span, dividing in-plane to produce the epidermis of all above-ground organs. As cells proliferate radially outward from the SAM's central zone into the peripheral zone, they remain fixed in position relative to one another, experience a gradient of the stem cell reporter *CLAVATA3*, initiate developmental programs, increase their growth rates, and decrease their interdivision times (11–16). These tissue-level growth kinetics are common to several plant species (13, 16, 17). Current models of the SAM and other tissues have assumed that cells trigger cytokinesis upon reaching a critical size (18–20). SAM cells recover their normal mean size following a genetically induced transient size increase, indicating some degree of size regulation (21), although whether size is regulated by the critical size, critical increment, or some other rule remains untested. Further, it is not known if size regulation acts upon cell volume, surface area [as reported for fission yeast (22)], or some other metric (e.g., anticlinal surface area). Moreover, whether size regulation is dependent on cellular parameters such as cell shape or growth rate, tissue-level properties such as cell-cell contact topology, or position within the SAM has not been determined.

Significance

How does a cell decide when to divide or initiate DNA replication? How does it regulate its own growth? These fundamental questions are not well understood in most organisms; this lack of understanding is particularly true for multicellular eukaryotes. Following classical studies in yeast, we have quantified the key aspects of cell growth and division dynamics in the *Arabidopsis* apical stem cell niche. Our results disprove various theories for plant stem cell size/cell cycle regulation, such as that cell cycle progression is triggered when a prefixed critical size is attained, and constitute the necessary first step in the development of integrative mechanistic theories for the coordinated regulation of cell cycle progression, cell growth, and cell size in plants.

Author contributions: L.W., Y.R., and H.J. designed research; L.W., Y.R., R.W., B.L., and J.T. performed research; L.W., Y.R., R.W., J.T., and H.J. contributed new reagents/analytic tools; L.W., Y.R., J.T., K.C.H., E.M.M., and H.J. analyzed data; and L.W., Y.R., R.W., K.C.H., E.M.M., and H.J. wrote the paper.

The authors declare no conflict of interest.

This article is a PNAS Direct Submission.

Freely available online through the PNAS open access option.

¹L.W. and Y.R. contributed equally to this work.

To whom correspondence should be addressed. Email: henrik.jonsson@slcu.cam.ac.uk.

This article contains supporting information online at www.pnas.org/lookup/suppl/doi:10.1073/pnas.1616768113/-DCSupplemental.

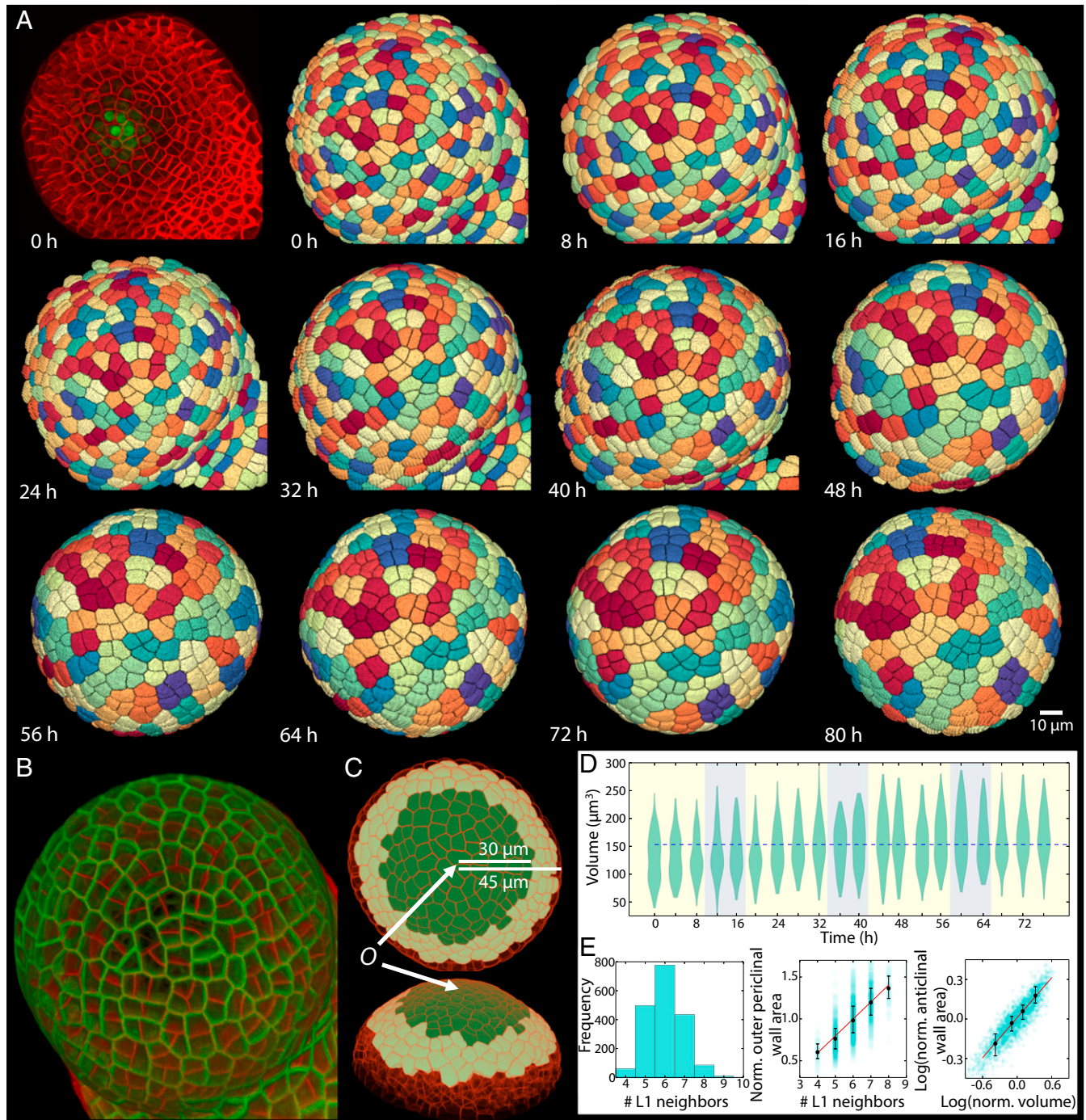


Fig. 1. Four-dimensional pipeline for single-cell quantification and lineage tracking over multiple cellular generations to characterize cell growth and size kinetics. (A) Time-lapse confocal stacks were acquired for each SAM every 4 h for 0 to ~80 h (every 8 h is shown). Plants were grown on NPA to inhibit growth of floral primordia that would have obstructed time-lapse imaging. The membrane reporter pUBQ10::acyl-YFP (red in top left panel) permitted accurate cellular segmentations and tracking using the MARS/ALT software (Materials and Methods), as well as quantification of cell size metrics. Cells are colored according to lineage, demonstrating that lineage tracking is ~100% accurate. A CLAVATA3 nuclear-bound reporter (green in top left panel) permitted nuclear segmentations. (B) Snapshot of SAM 1 at 48 h with all L1 division planes formed between 24 h and 48 h colored in red. (C) Cells within 30 μm of the center of the SAM, defined by O where O corresponds to the peak of CLAVATA3 expression, which coincides with lowest cellular growth rates, are regarded as the central zone and are included in the analysis; for sister asymmetry statistics, cells within 45 μm of the SAM's center are included in the analysis. (D) Distributions of L1 central zone cell volumes at each time point over the ~3-d time lapse, with light/dark cycles shaded in yellow/blue for SAM 3. The blue dashed line shows the time-averaged mean of cell volumes. There was a shift-up in volume after ~36 h of imaging (SI Appendix, Fig. S9). (E) Distribution of the number of L1 neighbors surrounding a cell (Left) and the linear relationship between the number of L1 neighbors (N_{neigh}) and outer periclinal wall area (A_{op}), $N_{\text{neigh}} \approx -0.15 + 0.2 A_{\text{op}}$ (Center) are in agreement with previously published data (SI Appendix, Table S1). (Right) Scaling between cell volume and anticlinal wall area is $V \sim A_{\text{op}}^{0.5}$, as demonstrated by the slope of 0.5 for $\log(V/\text{mean}(V))$ vs. $\log(A_{\text{op}}/\text{mean}(A_{\text{op}}))$; this scaling relationship is expected, given the in-plane growth and division of L1 cells (SI Appendix, Text S1). In each panel, data from all time points have been amalgamated for SAM 3 ($n = 1,867$) and black dots and error bars show medians and interquartile ranges, respectively. The corresponding data for other SAMs are provided in SI Appendix, Fig. S1 and Table S1. norm., normalized.

The rule for cell size regulation, together with growth kinetics over the cell cycle, determines a cell's interdivision time, and hence impact on the durations of its cell cycle phases. At least in some environmental conditions, various bacteria (23, 24) and budding yeast (8, 25, 26) grow at constant rates per unit size (constant relative growth rates) throughout the cell cycle, and metazoan lymphoblasts (27) and human osteosarcoma cells (28) grow at constant relative rates during certain cell cycle phases, whereas fission yeast has been reported to show bilinear growth (two distinct phases of a constant absolute growth rate) (29). In plant tissues where wall–wall contacts between cell neighbors impose additional growth constraints compared with single cells, constant relative growth rates have been tacitly assumed (12, 14, 30), but this assumption and whether growth rate varies through the cell cycle have not been tested experimentally.

Here, we develop a pipeline for high-throughput quantification of the size of epidermal cells in tissues of the *A. thaliana* SAM while tracking their growth over multiple generations. We applied this pipeline to characterize growth kinetics and to determine the nature of size regulation in the multicellular SAM context. Our data revealed that cells regulate their size by a mode intermediate between critical size and critical increment independent of position within the tissue, and that cell growth kinetics vary according to asymmetrical division of the mother cell.

Results

Neither a Cell Size Nor an Interdivision Time Checkpoint Is the Trigger for the G2/M Transition or Cell Division. Using our 4D quantification pipeline, we tracked 1,013 complete cell cycles between cell birth and division within the epidermal (L1) cell layer of the central zone over 3–4 d among SAMs grown on naphthalylphthalamic acid (NPA), which inhibited the initiation of floral primordia (31), and in 16-h light/8-h dark cycles (Fig. 1A–D and

Movies S1 and S2). The central zone is defined to be <30 μm from the center of the SAM (Fig. 1C); the CLAVATA3 signal is maximum at the center and decreases to ~0 over this range (Movies S1 and S2). The mean interdivision time was 21–31 h among SAMs, which is similar to a previous time-lapse imaging study of SAMs not grown on NPA (15). Our data confirmed reported distributions of L1 cell neighbor numbers, outer periclinal wall areas, and the linear relation (Lewis' law) between number of neighbors and outer periclinal wall area (32–35) (Fig. 1E and SI Appendix, Figs. S1 and S2 and Table S1). Our data also confirmed the power-law scaling of cell volume \sim (anticlinal wall area) $^{1/2}$ (Fig. 1E) that is expected, given the in-plane growth of L1 cells (SI Appendix, Text S1). In all SAMs ($n = 6$), cell volume and total surface area in the central zone did not vary with radial distance from the SAM center, whereas the proportions of surface area allocated to the outer periclinal and anticlinal walls increased and decreased, respectively (Fig. 2A and SI Appendix, Figs. S3–S7), demonstrating spatial variation of these size metrics and of mean cell shape. This result demonstrates that cell growth rate, which increases with distance from the SAM center, can be up-regulated independent of mean cell volume and surface area.

The methods used to deduce whether cells divide at a critical size, after a specific time period has elapsed, or after adding a critical increment rely on the assumption of homeostasis, and variations in mean cell size in space or time can create correlations among cell cycle variables that lead to erroneous conclusions about size regulation (SI Appendix, Fig. S8). Thus, to infer the mode of SAM cell size regulation correctly, given the spatiotemporal variability in cell size measurements, it was critical to devise cell cycle statistics that do not vary in space or time. First, because cell volumes in the L1 central zone did not vary with space (SI Appendix, Fig. S3) but increased marginally (~20%)

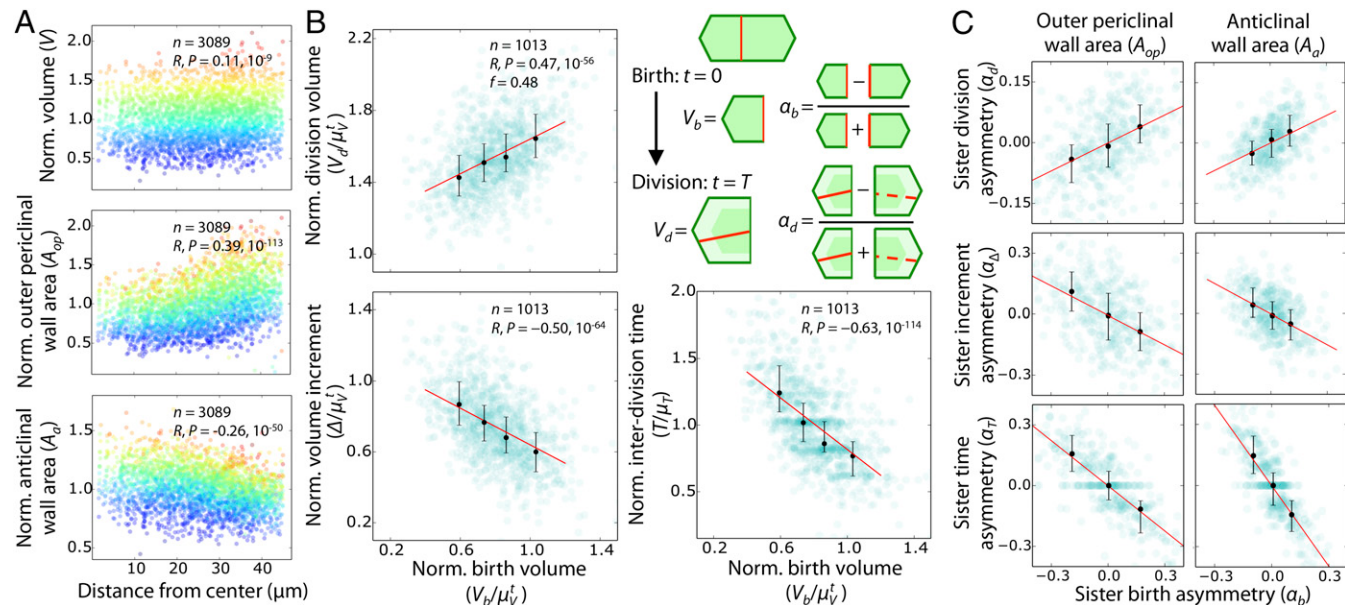


Fig. 2. G2/M transition and division are not triggered when the cell reaches a critical size, when the cell adds a critical increment, or when a specific time period has elapsed. (A) Although mean cell volume remained constant across the SAM, cell outer periclinal and anticlinal wall areas increased and decreased with distance from the SAM's center, respectively. Data points are colored according to cell volume. (B) Normalized cell birth volume (V_b/μ_V^3) was positively correlated with normalized division volume (V_d/μ_V^3) with a slope of $f \approx 0.5$, whereas normalized birth volume was negatively correlated with normalized volume increment (Δ/μ_V^3). Further, normalized birth volume was negatively correlated with interdivision time (T/μ_T). (C) Asymmetry in sister-cell birth sizes [$\alpha_d = (S_d - S^{sis}_d)/(S_d + S^{sis}_d)$] for outer periclinal wall areas (A_{op} ; $R = 0.46, P = 10^{-22}, n = 415$) and anticlinal wall areas (A_d ; $R = 0.55, P = 10^{-34}, n = 415$). Similarly, the asymmetry in sister birth sizes correlated negatively with both the asymmetry in sister size increments (α_d vs. α_s ; $R = -0.48, P = 10^{-25}$ for outer periclinal walls; $R = -0.47, P = 10^{-23}$ for anticlinal walls) and interdivision times (α_d vs. α_T ; $R = -0.77, P = 10^{-82}$ for outer periclinal walls; $R = -0.79, P = 10^{-91}$ for anticlinal walls) (SI Appendix, Table S5). In each panel, red lines show least-square linear fits; black error bars show medians and interquartile ranges; and N , R , and P give the sample size, the Pearson correlation coefficient, and the corresponding P value, respectively.

during the time lapse (*SI Appendix*, Fig. S9), we normalized cell volumes (V) at time t by the average volume of L1 central zone cells (μ_V^t) at time t . Second, we quantified sister-cell asymmetries as the differences between sister size metrics normalized by their sum; for example, the asymmetry in anticlinal wall area A_a is $\alpha_b = (A_{a,b} - A_{a,b}^{sis})/(A_{a,b} + A_{a,b}^{sis})$, where $A_{a,b}$ and $A_{a,b}^{sis}$ are the anticlinal wall areas at birth of two sister cells. Because a sister pair is born and divides at approximately the same position and time, these sister size asymmetry statistics have no spatiotemporal variation (*SI Appendix*, Figs. S10–S14 and Table S2).

In each SAM, for cells that were tracked over a complete cell cycle, both birth volume (V_b) and normalized birth volume (V_b/μ_V^t) were positively correlated with division volume (V_d) and normalized division volume (V_d/μ_V^t), respectively (with division being defined by the appearance of a new cell membrane/wall; for each plant, $n = 100\text{--}296$ cell cycles; $P \sim 10^{-16}\text{--}10^{-4}$ in *SI Appendix*, Table S3 and $P = 10^{-41}$ and 10^{-56} for nonnormalized and normalized pooled data in Fig. 2B). These correlations argue against an absolute cell volume checkpoint triggering division. Because our data show that G2/M occurs ≈ 40 min before division (*SI Appendix*, Table S4), whereas the mean interdivision time is 21–31 h (*SI Appendix*, Table S1), division events are essentially concurrent with G2/M, so G2/M also cannot be triggered by a cell volume checkpoint. Our sister size asymmetry statistics corroborate this result for total wall area, and outer periclinal, inner periclinal, and anticlinal wall areas ($n = 415$ sister pairs that underwent complete cell cycles that began < 45 μm from the SAM center; $P < 10^{-21}$ in Fig. 2C and *SI Appendix*, Table S5). Moreover, the strong negative correlations between birth volume and volume increment and between normalized birth volume and normalized volume increment ($P = 10^{-64}$ for pooled data in Fig. 2B and *SI Appendix*, Table S3), indicate that plant stem cells do not add a fixed size between divisions; this result was again corroborated for wall surface areas by sister size asymmetry statistics ($P < 10^{-22}$ in Fig. 2C and *SI Appendix*, Table S5). Thus, no critical size or critical increment checkpoint is imposed at G2/M or division.

Furthermore, in each SAM, strong negative correlations were observed between normalized birth volume and normalized interdivision time (T/μ_T , where μ_T is the mean interdivision time across a SAM) ($P = 10^{-114}$ for pooled data, Fig. 2B), and between sister size asymmetry at birth (α_b) and interdivision time asymmetry, $\alpha_T = (T - T^{sis})/(T + T^{sis})$ ($P < 10^{-66}$ in Fig. 2C and *SI Appendix*, Table S5). Thus, there is not an interdivision time checkpoint triggering the G2/M transition, indicating that cells do not simply grow for a fixed period between divisions. Because the durations of our experiments are finite, spanning the mean interdivision time by approximately threefold (*SI Appendix*, Table S1), cells with shorter interdivision times are inevitably overrepresented at the end of the experiment (*SI Appendix*, Fig. S15). To address this potential source of bias, we verified that the statistics were unaffected after recomputation using only data from cells born in the first half of the experiment (*SI Appendix*, Table S6). Taken together, our data reveal that neither division nor the G2/M transition is triggered by the cell reaching a critical size, adding a critical increment, or after a critical time has elapsed since birth.

Cells Grow at a Constant Rate per Unit Size, with the Smaller Sister from an Asymmetrical Division Growing at a Higher Relative Rate than the Larger Sister. We next computed statistics to reveal the nature of cell growth kinetics over the cell cycle. Averaged over the sample, the absolute growth rate of cell volume ($dV/dt \times \mu_T/\mu_b$, where μ_b is the mean birth volume) increased by a factor of ~ 1.8 over the first 80% of the cell cycle, whereas the relative growth rate (growth rate per unit volume, $dV/dt \times \mu_T/V$) remained nearly constant with a slight reduction within the final 20% of the cell cycle (Fig. 3A), indicating that volume grows at a rate proportional

to volume through $> 80\%$ of the cell cycle. This result continued to hold when the spatiotemporal growth rate variation across the SAM (*SI Appendix*, Fig. S16) was taken into account (*SI Appendix*, Fig. S17). Next, we determined the growth kinetics of different components of the cell wall. The planar growth of epidermal cells and their slow rates of shape change over the cell cycle necessitate power-law scalings among cell volume and wall area measurements (*SI Appendix*, Table S7). Such scalings combine with constant volumetric relative growth rates to predict that cells grow in proportion to their size, whether size is measured by volume, anticlinal wall area, periclinal wall area, or total wall area; this prediction was confirmed by our wall area measurements (*SI Appendix*, Text S1 and Fig. S18). Finally, we quantified how nuclear volume changes with cell size: The nuclear-localized CLAVATA3 reporter pCLV3::dsRED-N7 permitted the segmentation of nuclei within the approximately six to nine central cells positioned < 8 μm from the SAM center (*SI Appendix*, Supplemental Materials and Methods). These data show that nuclei grew continually throughout the cell cycle and scaled approximately proportionally with cell volume (Fig. 3B and C), occupying $30 \pm 7\%$ of cell volume.

We noticed that following asymmetrical divisions, the ratio of large/small daughter cell sizes decreased over the course of the cell cycle (Fig. 4A and *SI Appendix*, Table S8). This decrease occurred because the small sister grew at a faster relative rate than its larger sister (Fig. 4B). Division volume asymmetry, defined by $(V_b - V_b^{sis})/(V_b + V_b^{sis})$, was strongly correlated with both cell birth volume ($R = 0.87$, $P = 10^{-242}$) and the normalized difference between a cell's volume and the cell volume of its nonsister neighbors, defined by $(V - V^{ns-neigh})/(V + V^{ns-neigh})$, where $V^{ns-neigh}$ is the mean volume of nonsister neighbors ($R = 0.47$, $P = 10^{-280}$; *SI Appendix*, Fig. S19). To determine whether the difference in relative growth rates between sister cells is driven by a dependence on birth volumes, on cells having differently sized neighbors, or on division asymmetry of mother cells, we first restricted our analysis to cells generated by symmetrical divisions [cells with $|(V_b - V_b^{sis})/(V_b + V_b^{sis})| \leq 0.11$, to include $\sim 50\%$ of data in the analysis] and found that relative growth rate then did not depend significantly on birth volume (Kruskal–Wallis: $H = 3$, $P = 0.4$) or on the relative sizes of nonsister neighbors (Kruskal–Wallis: $H = 5$, $P = 0.14$) (*SI Appendix*, Fig. S20 and Table S8). Second, we determined that the dependence of relative growth rates on asymmetrical divisions persisted when the data were restricted to either cells of intermediate birth volumes ($H = 73$, $P = 10^{-15}$ for $|V_b/\text{mean}(V_b) - 1| \leq 0.16$, to include $\sim 50\%$ of data) or cells with sizes similar to the average size of their nonsister neighbors [$H = 43$, $P = 10^{-9}$ for $|(V - V^{ns-neigh})/(V + V^{ns-neigh})| \leq 0.11$, to include $\sim 50\%$ of data] (*SI Appendix*, Fig. S20 and Table S8). In sum, there is no dependence of relative growth rate on either birth volume or the volume difference between a cell and its nonsister neighbors for cells generated by symmetrical divisions, whereas for cells born close to the average volume, the dependence of relative growth rate on asymmetrical division of the mother cell is strong; these data indicate that the difference in sister-cell relative growth rates is driven primarily by the asymmetrical division, and, consequently, there is a negative correlation between asymmetrical division and relative growth rate and between cell birth size and relative growth rate. Results for inner and outer periclinal wall areas were similar, but for anticlinal and total wall areas, the relative growth rate no longer depended significantly on asymmetrical division after the analysis was restricted to data subsets as described above (*SI Appendix*, Table S8).

Beyond the position dependence of relative growth rates as cells proliferate away from the central zone, we found no evidence that relative growth rates are inherited from mother to daughter cells (*SI Appendix*, Fig. S21), although it is possible that noise in our data precludes detection of such an inheritance. We

could discern no strong and consistent impact across the SAMs of light/dark cycling on growth rates or division patterns (*Movies S3* and *S4* and *SI Appendix*, Fig. S22); this observation may be due either to the frequent interruptions of the light/dark cycles during image acquisition or to the suppression of signaling responses to light that are partly mediated by auxin (36), and thus may be partly suppressed in NPA-grown plantlets. Regardless, our data indicate that the difference in relative growth rates between sister cells resulted from asymmetrical divisions, and, because the small sister grew more between divisions than the large sister, the higher relative growth rate of the small sister resulted in more similar sister interdivision times (Fig. 4B).

Size Regulation in the SAM Is Cell-Autonomous Rather than Position-Dependent. In a multicellular tissue, it is feasible that the mode of cell size regulation varies according to interactions between neighboring cells or when cells are subject to a chemical/hormonal gradient. For single-celled organisms in homeostatic environments, the various modes of size regulation can all be captured by a single equation:

$$V_d = f V_b + \mu_b (2-f) + Z, \quad [1]$$

where Z is Gaussian noise with mean 0 and SD $(4\sigma_d^2 - f^2\sigma_b^2)^{1/2}$, where σ_b and σ_d are the coefficients of variation of V_b and V_d , respectively; and f defines the mode of cell size regulation. The expression $f = 0$ gives division size $= V_d = \text{constant} + \text{noise}$, which corresponds to the critical size mode; $f = 1$ gives size increment $= V_d - V_b = \text{constant} + \text{noise}$, which corresponds to the critical increment mode; and $f = 2$ gives interdivision time $= \mu_T \times$

$\log_2(V_d/V_b)$ (given that cells grow at a constant relative rate) $= \mu_T \times \log_2(2 + \mu_b/V_b \times Z) \approx \text{constant} + \text{noise}$, which corresponds to specific time mode (4, 37). The finding that cell volume grows at a constant relative rate implies that cell volume increases exponentially with time, so $V(t) = V_b e^{gt}$ where, necessarily, $g = \ln 2/\mu_T$ because, in homeostatic environments, cells double their volume, on average, over a cell cycle. Our pooled data from all SAM cells tracked over a complete cell cycle and from sister-cell pairs tracked over a complete cell cycle both give $f \approx 0.5$ (Fig. 2B and *SI Appendix*, Text S2 and Tables S3 and S5). Therefore, plant stem cells regress to their mean target size over several generations, with fluctuations decaying to one-fourth of their initial value over one cell cycle on average: Subtracting the mean cell size at division ($2\mu_b$) from either side of Eq. 1 with $f = 0.5$ gives that (fluctuation away from mean division size) $= (V_d - 2\mu_b) = 0.5(V_b - \mu_b) = 0.5 \times (\text{fluctuation away from mean birth size})$; because cells divide in half, on average, to produce newborn cells in the next generation, therefore (fluctuation away from mean birth size in the next generation) $= 0.25 \times (\text{fluctuation away from mean birth size})$. This rate is intermediate between the critical increment and critical size modes: The same calculation shows that for critical size ($f = 0$), fluctuations decay to 0 within one generation, whereas for critical increment ($f = 1$), fluctuations decay to one-half of their initial value within one generation.

To establish whether the relation $V_d \approx 0.5 V_b + \mu_b \times (1.5 + \text{noise})$ is robust and independent of cells' spatiotemporal positions, we removed 50% of the data at random or according to whether cells are born (i) early/late during the time lapse, (ii) small/large compared with the mean birth size, (iii) during light

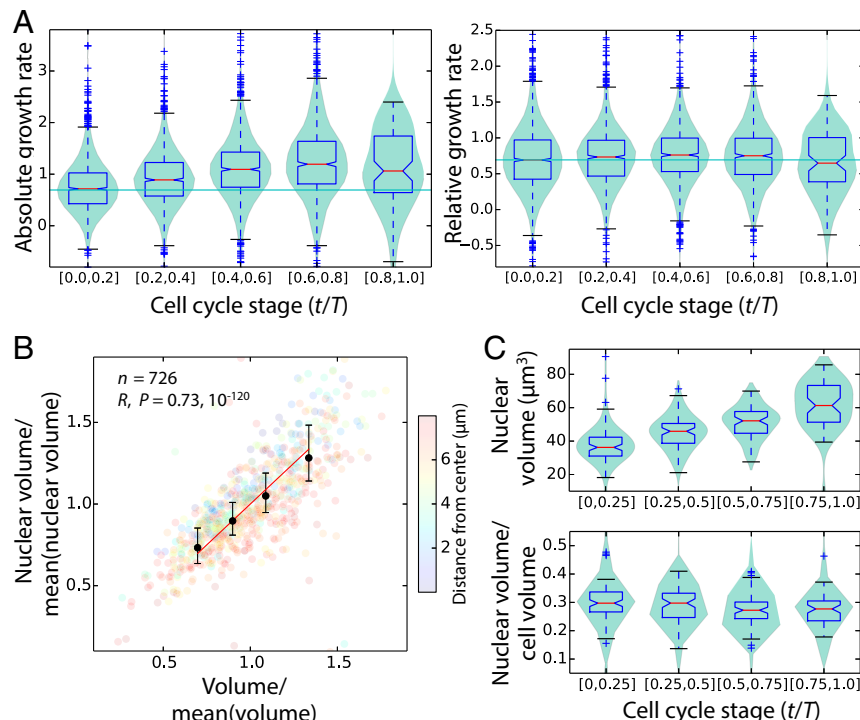


Fig. 3. Cells grow at a rate proportional to their size, and nuclei grow continually through most of the cell cycle. (A) Absolute volumetric growth rate increased by ~1.8-fold over the first 80% of the cell cycle, whereas the volumetric relative growth rate remained constant throughout the cell cycle at the expected value of $\ln(2)$ (green horizontal line) for V/V_b ($n = 4,299$). Cell cycle stage is defined as time from birth of a cell, t , divided by its cell cycle duration, T . Growth rates during mitosis/new cell wall formation are omitted. (B) Nuclear volume was approximately proportional to cell volume as it varied over an approximately twofold range [red line corresponds to $y = x$; a least-square linear fit gives nuclear volume/mean(nuclear volume) = $0.86 \times$ cell volume/mean (cell volume) + 0.13]. The plot includes data from all time points and all cells within a radius of 8 μm ($n = 726$): The CLAVATA3 signal diminished with distance from the SAM center, rendering nuclear volume segmentations inaccurate beyond ~8 μm (*Movies S1* and *S2* and *SI Appendix*, Fig. S23). Black error bars show medians and interquartile ranges. (C) Nuclei grew continually throughout the cell cycle, so that the average nuclear volume/cell volume ratio remained approximately constant at ~30%. Each plot includes data from all completed cell cycles that began within a radius of 8 μm ($n = 332$).

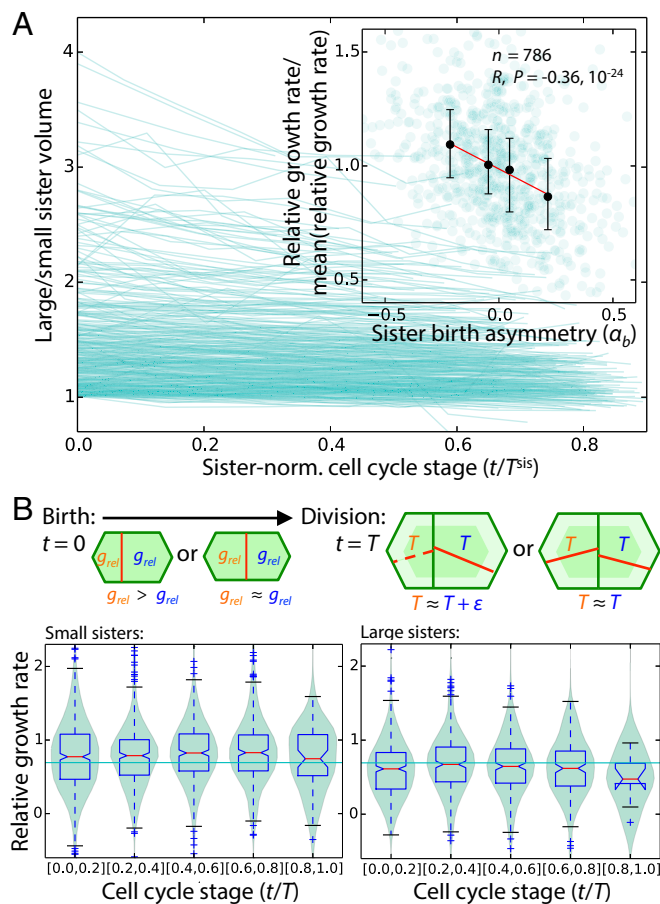


Fig. 4. Smaller daughters grow at a faster rate per unit size than their larger sisters following asymmetrical divisions. (A) Ratio of large to small sister-cell volumes decreased over the course of the cell cycle among mother cells that divided asymmetrically (time since birth, t , is normalized by the average of sister interdivision times, T^{sis}). (Inset) Degree of asymmetrical division, $\alpha_b = (V - V^{\text{sis}}_b)/(V_b + V^{\text{sis}}_b)$, was negatively correlated with the cell's average relative growth rate over its cell cycle (black error bars show medians and interquartile ranges, red line is least-square linear fit to the medians). (B) Smaller sisters born of an asymmetrical division ($\alpha_b \leq -0.11$; $n = 1,586$) grew at an above-average constant relative rate throughout their cell cycle, whereas larger sisters ($\alpha_b \geq 0.11$; $n = 1,054$) grew at a below-average constant relative rate; the schematic illustrates that this growth pattern results in sisters having more similar interdivision times.

or dark periods, (iv) in the inner/outer region of the central zone, (v) with comparatively small/large neighboring cells, or (vi) with a comparatively small/large number of L1 neighbors. In all cases, there is little effect on f (SI Appendix, Table S6). Through this inspection, we excluded several phenomenological hypotheses that may have accounted for $f \approx 0.5$. For example, if cell division were triggered once cells attained both a critical size and a critical increment where the critical increment (μ_b) is approximately half of the critical size ($2 \times \mu_b$), then small cells ($V_b < \mu_b$) would, on average, reach the critical increment first; thus, they would divide upon reaching a critical size, giving $f \approx 0$, whereas large cells ($V_b > \mu_b$) would reach the critical size first and then divide upon reaching a critical increment, giving $f \approx 1$, thus accounting for $f \approx 0.5$ across the whole population. However, there was no such trend in our data (Fig. 2B and SI Appendix, Table S6). Similarly, division is not triggered when cells attain either a critical size or a critical increment; then small cells ($V_b < \mu_b$) would give $f \approx 1$, whereas large cells ($V_b > \mu_b$) would give $f \approx 0$. If a subset of cells divided at a particular point in the light/dark cycle according to a circadian

rhythm, then cells born at this point would divide after a specific time had elapsed, giving $f \approx 2$; again, no such trend is apparent in our data (Fig. 2B and SI Appendix, Table S6). Furthermore, we could discern no clear cell division spatial pattern or tendency for synchronization from movies of different SAMs (Movies S3 and S4). Because asymmetrical division of the mother cell affects relative growth rate of the two daughter cells (Fig. 4B), we assessed whether size regulation depends on division asymmetry. When our data were split according to whether cells were born of a symmetrical or asymmetrical division, we again obtained $f \approx 0.5$ (SI Appendix, Table S6).

The fact that f does not vary with cell position within the meristem's central zone, the size of neighboring cells, or other spatial variables suggested a cell-autonomous mode of size regulation. To test this hypothesis further, we compared our experimental data with simulations of cell size kinetics parameterized by Eq. 1, with all simulation parameters prescribed by our experimental measurements and with cells growing at constant relative rates that depend on mother-cell division asymmetry (SI Appendix, Text S3). All statistics were closely recapitulated, with no fitting parameters (Fig. 5 and SI Appendix, Table S9). The close agreement between our simulations and experiments indicates that a cell-autonomous mode of G2/M regulation is consistent not only with the mean trends (Fig. 5 B, i–iii) but also with most of the variability (Fig. 5 B, iv–vi) in our data. The simulation noise value of ~ 0.23 indicates that $\sim 60\%$ of cells miss their target mean division size ($\approx 0.5V_b + 1.5\mu_b$) by $<12\%$, in approximate agreement with previous noise measurements for single-celled organisms (6); this plausible degree of size regulation and the frequency of asymmetrical division together account for the variability in cell size (compare Fig. 2B with Fig. 5A, Inset). Further, the dependence of relative growth rate on asymmetrical division of the mother cell was sufficient to account for the quantitative dependencies among cell cycle variables determined by birth volume and interdivision time (Fig. 5 B, iii and vi).

Discussion

In this study, we have refuted the long-standing unexamined assumption that epidermal cells in the SAM undergo G2/M and divide at a critical size, or after a fixed time period has elapsed (Fig. 2 B and C). Instead, cells follow a size regulation rule that is intermediate between dividing at a critical size and adding a critical increment, causing cell size fluctuations from the mean to decay by $\sim 75\%$ in one generation. Cells in the SAM experience molecular gradients, alter growth rates depending on position, and are subject to cell–cell contact constraints, yet our analyses indicate that the size regulation rule persists independent of position within the tissue or cell–cell contact topologies. In other eukaryotes, both G1/S and G2/M are subject to size checkpoints (2, 38, 39). Cell size and ploidy increase together when the endocycle, which bypasses mitosis, is implemented in *A. thaliana* sepals (40) and other differentiated tissues or by blocking division with the microtubule inhibitor oryzalin (13), indicating that the trigger for G1/S may affect regulation of the cell size/ploidy ratio rather than cell size per se (41). Our results indicate that in the SAM, where cells are diploid, G1/S is not triggered by the attainment of a critical size or critical cell size/ploidy ratio, because such regulation would contradict the positive correlations between birth and division sizes (Fig. 2 B and C).

We showed that during the cell cycle, cells expand continually at a rate proportional to their size at least until the final $<20\%$ of their cell cycle, with nuclei also growing continually at a similar rate until mitosis (Fig. 3 B and C). Because in *Arabidopsis* shoot apices G1, S, and G2, phases have been reported to last for $\sim 50\%$, $\sim 25\%$, and $\sim 15\%$ of the cell cycle (42), our data imply that nuclei grow through each of these phases, as in other organisms (43, 44). Following an asymmetrical division, the small daughter grew at a faster rate per unit size than the large daughter

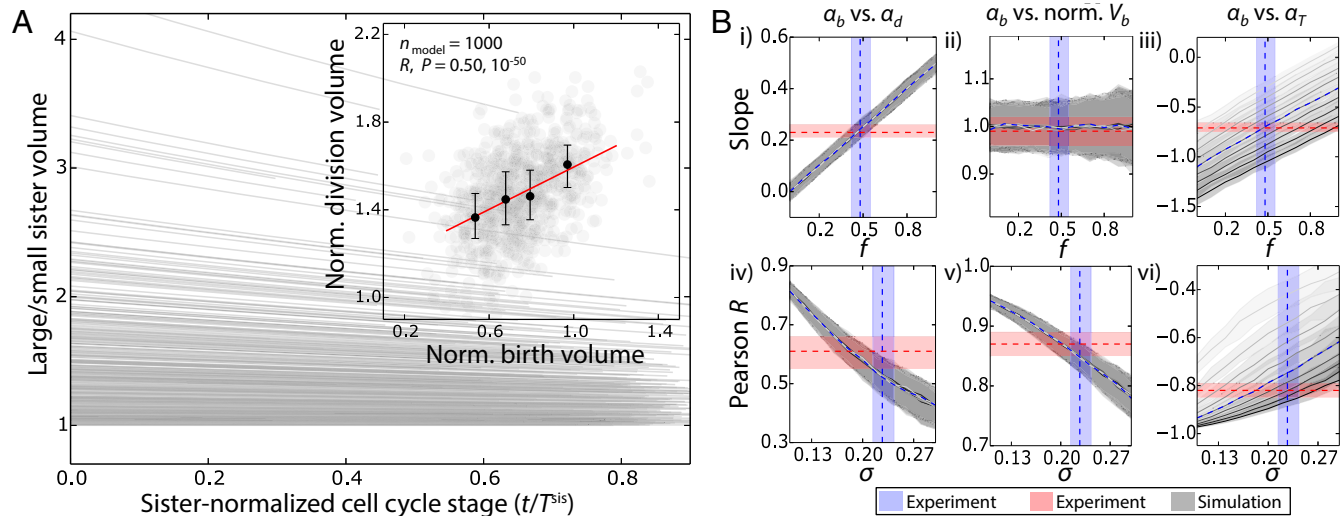


Fig. 5. Our experimental data are consistent with cell-autonomous growth and size regulation in the SAM, with no apparent dependence on cell position. (A) Simulation with no free parameters closely recapitulated all experimental data. In the simulation, division size depended on birth size according to Eq. 1 and cells grew exponentially in proportion to their size over the cell cycle, with smaller sisters growing at a faster relative rate than their larger sister; parameters were set to their experimentally measured values [compare Fig. 4A (main panel and *Inset*) with Fig. 2B and *SI Appendix, Text S3 and Table S9*], and the sample size, n_{model} , was set close to the sample size of the experimental data. (B) Simulation recapitulated experimentally measured fitted slopes (*i*–*iii*) and Pearson R values (*iv*–*vi*) only when simulation parameters were set close to their experimentally measured values. Experimentally measured medians and 90% confidence intervals are shown by dashed lines and shaded regions for fitted slopes and Pearson R values in red and for simulation parameters f (size regulation rule) and σ (noise) in blue (*SI Appendix, Text S3*). The effect of varying the strength of growth rate dependence on asymmetrical division, g_{asym} , is shown in each panel by different gray shades ($g_{\text{asym}} = -0.03$ to $0.1 \times i$, $i = 0, \dots, 8$ increases with opacity of gray; shaded regions, which are overlapping in *i*, *ii*, *iv*, and *v*, show 90% confidence intervals from simulations). The discrepancies between simulated and experimental Pearson R values indicate that the experimentally measured noise (σ) may be overestimated by ~10%. These plots show that our experimental data and simulations are nontrivially consistent with one another.

(Fig. 4 *A* and *B*). Although it is challenging to infer dependences from these data due to the tight correlations among variables, the simplest interpretation of our analyses (*SI Appendix, Fig. S20*) is that the difference in per unit size growth rates between sisters is driven primarily by the asymmetrical division of the mother cell rather than by other size-related metrics with which asymmetrical division is correlated. This phenomenon is not straightforwardly accounted for by a cell wall growth rate that depends on elastic stress or strain of the wall, a mechanism that partially controls growth rate and is modulated by turgor (45–48). How this sister-cell growth heterogeneity can be integrated with the report that growth heterogeneity is induced by neighbor interactions (30) is a future challenge. A feasible mechanism features a master regulator of growth with the following dynamics: (*i*) its concentration is fixed through the cell cycle and is proportional to the per unit size growth rate; (*ii*) upon mitosis, the growth regulator is degraded or synthesized to attain a specific concentration; and (*iii*) upon division, the regulator is partitioned equally in number between the two daughters perhaps via titration against DNA (41). Such a mechanism would impart a higher concentration of the master regulator to the smaller sister.

Molecular mechanisms regulating cell size in budding and fission yeast have recently been characterized. In fission yeast, the peripheral membrane protein kinase cdr2p has been reported to regulate cell surface area to a critical value at G2/M (22). In the SAM, our data show that cell surface area and volume are regulated by a mode intermediate between critical size and critical increment. In budding yeast daughter cells, through cyclin-dependent kinase (CDK)/cyclin activity inhibition, the transcriptional inhibitor Whi5 controls cell size at G1/S via a dilution process whereby Whi5 is synthesized at a roughly constant rate through S/G2/M, which lasts for an approximately fixed time, and is then diluted out by growth during G1, triggering S-phase when it falls below a specific concentration (49). This or a similar mechanism can potentially implement the critical increment mode of size regulation (8). Such

a diluter mechanism may account for a regulatory mode that is intermediate between critical increment and critical size as identified in this study, but with modification such as inhibitor degradation during the cell cycle. *A. thaliana* has no structural *whi5* or *cdr2p* homologs, but the *A. thaliana* homolog of human retinoblastoma (RBR1) plays a functional role that is similar to Whi5 (50, 51). It would be informative to quantify the spatiotemporal dynamics of RBR1 through the cell cycle. Because it is feasible that different cellular components are subject to different size regulatory rules, a second scenario that could account for size regulation intermediate between critical size and critical increment is that the cytoplasm grows to a critical size, whereas the nucleus adds a critical increment. Single-cell tracking experiments can again be used to establish the growth and size kinetics of different cellular components and key growth regulators such as ribosomes.

Cell size has important physiological implications, determining both the surface area/volume ratio and the ratio of cytoplasm/DNA, thereby likely impacting nutrient uptake rates, protein concentrations, and transcription frequencies. Cell size and growth rates vary strongly within a plant according to tissue and developmental stage, particularly among cells that follow terminal differentiation paths, such as guard cells and pavement cells. Growth and size are evidently regulated in coordination with the cell cycle. The array of cyclins and the two types of CDKs of *A. thaliana* and their multiple levels of regulation indicate that cell cycle control, as well as its interplay with developmental signals, is complex (52). However, results in yeast suggest that the underpinning molecular features of CDK/cyclin-dependent cell cycle progression are surprisingly simple (53), and the role of CDKs/cyclins is broadly conserved among eukaryotes (52). Our methodology is potentially transferrable not only to other *A. thaliana* tissues and cell cycle fluorescent reporters but also to other plant species, and thus should be able to illuminate features of cell size, growth, and cell cycle control in different multicellular contexts, perhaps identifying conserved strategies

for linking together these controls. The regulation of cell size is a fundamental challenge for all organisms, and its study can ultimately provide insight into the control of multiple processes essential to life.

Materials and Methods

Construction of a YFP Plasma Membrane Marker and Other Transgenic Lines. DNA containing the coding sequence for YFP was amplified by PCR using primers attb1-mYfwd (5'-AAAAAGCAGGCTATGGGAGGATGCTCTAAGA-AGGTGAGC) and attb2-YFPrev (5'-AGAAAGCTGGGTTACTGTACAGCTCG-TCCATGCCAGAGTG).

The total reaction volume was 50 μ L. The forward primer contains a short sequence encoding a motif that is acylated in plant cells (54). Both primers contain a portion of the attB gateway sites. Amplification conditions were 96 °C for 1 min followed by 25 cycles of 96 °C for 30 s, 54 °C for 55 s, and 72 °C for 30 s, and a final elongation of 72 °C for 30 s. After checking for products on a gel, 5 μ L of the PCR was used in a second reaction (40 μ L total) containing primers B1 adapt (5'-GGGGACAAGTTTACAAAAAGCAGGCT) and B2 adapt (5'-GGGGACCCTTGACAGAAAGCTGGT).

Amplification conditions were 95 °C for 2 min followed by five cycles of 94 °C for 30 s, 48 °C for 30 s, and 72 °C for 1 min; 20 cycles of 94 °C for 30 s, 55 °C for 30 s, and 72 °C for 1 min; and a final elongation of 72 °C for 1 min. Products were PCR-purified (Qiagen) and then used in a one-tube format Gateway reaction as per the manufacturer's instructions, with the destination vector pUB-DEST containing the *UBQ10* promoter upstream of the Gateway site (55). The resulting vector, pUBQ10::acyl-YFP, was transformed into *A. thaliana* Col-0 containing pPIN1::PIN1-GFP (56, 57). The pUBQ10::acyl-YFP/pPIN1::PIN1-GFP plants were taken to the second filial (F2) generation and crossed with pCLV3::dsRED-N7 (58), a nuclear-localizing reporter for *CLAVATA3* expression. This cross was taken to the F3 generation, yielding pUBQ10::acyl-YFP/pPIN1::PIN1-GFP/pCLV3::dsRED-N7 *A. thaliana* seeds. The pUBQ10::acyl-YFP reporter localized strongly and uniformly to cell membranes; it was stably expressed without cellular internalization and without affecting plant growth or development. These features permitted the accurate segmentation and tracking of cells. The reporter pCLV3::dsRED-N7, a nuclear-localized *CLAVATA3* reporter, identified the stem cell niche's center and, in a subset of SAM cells, enabled nuclear volume quantification (59) (*SI Appendix, Supplemental Materials and Methods*). The pPIN1::PIN1-GFP reporter was not analyzed as part of this study.

Plant Growth Conditions. NPA-treated pUBQ10::acyl-YFP/pPIN1::PIN1-GFP/pCLV3::dsRED-N7 *A. thaliana* Col-0 plants were grown on plates with *Arabidopsis* medium supplemented with 10 μ M NPA (31) at 20 °C with 16 h of light per day. These plants were later selected for imaging between 24 and 28 d after germination. NPA was used to inhibit organ formation (31)

without substantially slowing proliferation in the SAM's central zone (15) so that time-lapse images could be acquired without dissection, and therefore with minimal disturbance to cell proliferation.

Time-Lapse Image Acquisition and Quantification. NPA-grown plantlets with naked, organ-free meristems were selected and gently transferred to lidded boxes measuring 5 × 5 × 3 cm³ containing room-temperature *Arabidopsis* medium supplemented with 10 μ M NPA to a depth of ~1 cm. Plantlets were screened for the expression of pUBQ10::acyl-YFP, pPIN1::PIN1-GFP, and pCLV3::dsRED-N7 using confocal microscopy, and then left to recover for 12 h in the same 16/8-h light/dark cycle. All three reporters were expressed in each of SAMs 2–6; SAM 1 expressed only pUBQ10::acyl-YFP and pPIN1::PIN1-GFP. Confocal z-stacks were acquired every 4 h for 3–3.5 d at a resolution of 0.22 × 0.22 × 0.26 μ m³ per voxel using a 63×/1.0 N.A. water immersion objective; excitation wavelengths of 488 nm and 561 nm; the corresponding dichroic filters; and a precalibrated spectral unmixing that enabled accurate separation of the YFP, GFP, and RFP signals. The confocal scan speed was no more than 9, and line averaging was set to 2. Each z-stack took ~10 min to acquire. At the end of each high-z-resolution z-stack acquisition, a second low-z-resolution z-stack was rapidly acquired over ~10 s with a z-step of 5–6 μ m (to enable correction of a major artifact, a stretching in the z-direction owing to growth/movement in the stem during image acquisition; *SI Appendix, Supplemental Materials and Methods*). Data on cell size and growth kinetics were extracted by application of our 4D cellular quantification and tracking pipeline using MARS/ALT software (60) (*SI Appendix, Supplemental Materials and Methods* and *Movies S5–S7*).

Statistical Analysis, Modeling, and Simulations. Cellular quantification and tracking data were analyzed with Python 2.7 scripts using the NumPy and SciPy libraries and StatsModels package. Simulations were performed based on a generalization of the models originally proposed (4, 37); simulations are detailed in *SI Appendix, Text S3*.

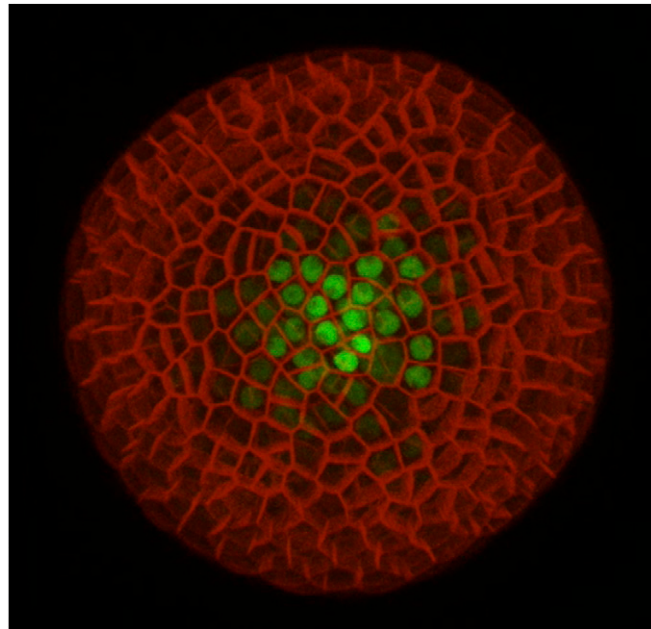
ACKNOWLEDGMENTS. We thank Pau Formosa-Jordan, Daniel McKay, Charles Melnyk, Arun Sampathkumar, and Bruno Martins for stimulating discussions; David Ehrhardt for comments on the manuscript; and Christophe Godin and Gregoire Malandain for use of MARS/ALT software. The data reported in this paper are tabulated in *SI Appendix, Tables S1–S10* and archived at the D-Space Repository database (Cambridge University). This work was supported by the Gatsby Charitable Foundation through Grant GAT3395-PR4 (to H.J.) and Fellowships GAT3272/C and GAT3273-PR1 (to E.M.M.), Swedish Research Council Grant VR2013:4632 and Knut and Alice Wallenberg Foundation Grant KAW2012.0050 (to H.J.), the Howard Hughes Medical Institute and Gordon and Betty Moore Foundation Grant GBMF3406 (to E.M.M.), and National Science Foundation Faculty Early Career Development (CAREER) Program Award MCB-1149328 (to K.C.H.).

1. Ginzberg MB, Kafri R, Kirschner M (2015) Cell biology. On being the right (cell) size. *Science* 348(6236):1245075.
2. Fantes P, Nurse P (1977) Control of cell size at division in fission yeast by a growth-modulated size control over nuclear division. *Exp Cell Res* 107(2):377–386.
3. Fantes PA (1977) Control of cell size and cycle time in *Schizosaccharomyces pombe*. *J Cell Sci* 24(1):51–67.
4. Amir A (2014) Cell size regulation in bacteria. *Phys Rev Lett* 112:208102.
5. Campos M, et al. (2014) A constant size extension drives bacterial cell size homeostasis. *Cell* 159(6):1433–1446.
6. Taheri-Arabi S, et al. (2015) Cell-size control and homeostasis in bacteria. *Curr Biol* 25(3):385–391.
7. Sauls JT, Li D, Jun S (2016) Adder and a coarse-grained approach to cell size homeostasis in bacteria. *Curr Opin Cell Biol* 38:38–44.
8. Soifer I, Robert L, Amir A (2016) Single-cell analysis of growth in budding yeast and bacteria reveals a common size regulation strategy. *Curr Biol* 26(3):356–361.
9. Sompayrac L, Maaloe O (1973) Autorepressor model for control of DNA replication. *Nat New Biol* 241(109):133–135.
10. Ho PY, Amir A (2015) Simultaneous regulation of cell size and chromosome replication in bacteria. *Front Microbiol* 6:662–672.
11. Reddy GV, Meyerowitz EM (2005) Stem-cell homeostasis and growth dynamics can be uncoupled in the *Arabidopsis* shoot apex. *Science* 310(5748):663–667.
12. Dumais J, Kwiatkowska D (2002) Analysis of surface growth in shoot apices. *Plant J* 31(2):229–241.
13. Laufs P, Grandjean O, Jonak C, Kiéu K, Traas J (1998) Cellular parameters of the shoot apical meristem in *Arabidopsis*. *Plant Cell* 10(8):1375–1390.
14. Kwiatkowska D (2004) Surface growth at the reproductive shoot apex of *Arabidopsis thaliana* pin-formed 1 and wild type. *J Exp Bot* 55(399):1021–1032.
15. Reddy GV, Heisler MG, Ehrhardt DW, Meyerowitz EM (2004) Real-time lineage analysis reveals oriented cell divisions associated with morphogenesis at the shoot apex of *Arabidopsis thaliana*. *Development* 131(17):4225–4237.
16. Lyndon RF (1970) Rates of cell division in the shoot apical meristem of *Pisum*. *Ann Bot (Lond)* 34(1):1–17.
17. Green PB, Havelange A, Bernier G (1991) Floral morphogenesis in *Anagallis*: Scanning-electron-micrograph sequences from individual growing meristems before, during, and after the transition to flowering. *Planta* 185(4):502–512.
18. Smith RS, et al. (2006) A plausible model of phyllotaxis. *Proc Natl Acad Sci USA* 103(5): 1301–1306.
19. Jönsson H, Heisler MG, Shapiro BE, Meyerowitz EM, Mjolsness E (2006) An auxin-driven polarized transport model for phyllotaxis. *Proc Natl Acad Sci USA* 103(5): 1633–1638.
20. Dupuy L, Mackenzie J, Haseloff J (2010) Coordination of plant cell division and expansion in a simple morphogenetic system. *Proc Natl Acad Sci USA* 107(6):2711–2716.
21. Serrano-Mislata A, Schiessl K, Sablowski R (2015) Active control of cell size generates spatial detail during plant organogenesis. *Curr Biol* 25(22):2991–2996.
22. Pan KZ, Saunders TE, Flor-Parral I, Howard M, Chang F (2014) Cortical regulation of cell size by a sizer cdr2p. *eLife* 3(e02040):e02040.
23. Godin M, et al. (2010) Using buoyant mass to measure the growth of single cells. *Nat Methods* 7(5):387–390.
24. Wang P, et al. (2010) Robust growth of *Escherichia coli*. *Curr Biol* 20(12):1099–1103.
25. Di Talia S, Skotheim JM, Bean JM, Siggia ED, Cross FR (2007) The effects of molecular noise and size control on variability in the budding yeast cell cycle. *Nature* 448(7156): 947–951.
26. Di Talia S, et al. (2009) Daughter-specific transcription factors regulate cell size control in budding yeast. *PLoS Biol* 7(10):e1000221.
27. Tzur A, Kafri R, LeBleu VS, Lahav G, Kirschner MW (2009) Cell growth and size homeostasis in proliferating animal cells. *Science* 325(5937):167–171.
28. Mir M, et al. (2011) Optical measurement of cycle-dependent cell growth. *Proc Natl Acad Sci USA* 108(32):13124–13129.
29. Baumgärtner S, Tolj-Nørrelykke IM (2009) Growth pattern of single fission yeast cells is bilinear and depends on temperature and DNA synthesis. *Biophys J* 96(10): 4336–4347.

30. Uyttewaal M, et al. (2012) Mechanical stress acts via katanin to amplify differences in growth rate between adjacent cells in *Arabidopsis*. *Cell* 149(2):439–451.
31. Grandjean O, et al. (2004) In vivo analysis of cell division, cell growth, and differentiation at the shoot apical meristem in *Arabidopsis*. *Plant Cell* 16(1):74–87.
32. Lewis FT (1926) The effect of cell division on the shape and size of hexagonal cells. *Anat Rec* 33(5):331–335.
33. Lewis FT (1928) The correlation between cell division and the shapes and sizes of prismatic cells in the epidermis of *Cucumis*. *Anat Rec* 38(3):341–376.
34. Shapiro BE, Tobin C, Mjolsness E, Meyerowitz EM (2015) Analysis of cell division patterns in the *Arabidopsis* shoot apical meristem. *Proc Natl Acad Sci USA* 112(15):4815–4820.
35. Gibson MC, Patel AB, Nagpal R, Perrimon N (2006) The emergence of geometric order in proliferating metazoan epithelia. *Nature* 442(7106):1038–1041.
36. Yoshida S, Mandel T, Kuhlemeier C (2011) Stem cell activation by light guides plant organogenesis. *Genes Dev* 25(13):1439–1450.
37. Tanouchi Y, et al. (2015) A noisy linear map underlies oscillations in cell size and gene expression in bacteria. *Nature* 523(7560):357–360.
38. Nurse P (1975) Genetic control of cell size at cell division in yeast. *Nature* 256(5518):547–551.
39. Johnston GC, Pringle JR, Hartwell LH (1977) Coordination of growth with cell division in the yeast *Saccharomyces cerevisiae*. *Exp Cell Res* 105(1):79–98.
40. Roeder AHK, et al. (2010) Variability in the control of cell division underlies sepal epidermal patterning in *Arabidopsis thaliana*. *PLoS Biol* 8(5):e1000367.
41. Amodeo AA, Skotheim JM (2016) Cell-size control. *Cold Spring Harb Perspect Biol* 8(4):a019083.
42. Dewitte W, et al. (2003) Altered cell cycle distribution, hyperplasia, and inhibited differentiation in *Arabidopsis* caused by the D-type cyclin CYCD3. *Plant Cell* 15(1):79–92.
43. Fidorra J, Melk T, Booz J, Feinendegen LE (1981) Cellular and nuclear volume of human cells during the cell cycle. *Radiat Environ Biophys* 19(3):205–214.
44. Neumann FR, Nurse P (2007) Nuclear size control in fission yeast. *J Cell Biol* 179(4):593–600.
45. Hamant O, et al. (2008) Developmental patterning by mechanical signals in *Arabidopsis*. *Science* 322(5908):1650–1655.
46. Corson F, et al. (2009) Turning a plant tissue into a living cell froth through isotropic growth. *Proc Natl Acad Sci USA* 106(21):8453–8458.
47. Kierzkowski D, et al. (2012) Elastic domains regulate growth and organogenesis in the plant shoot apical meristem. *Science* 335(6072):1096–1099.
48. Lockhart JA (1965) An analysis of irreversible plant cell elongation. *J Theor Biol* 8(2):264–275.
49. Schmoller KM, Turner JJ, Köivomägi M, Skotheim JM (2015) Dilution of the cell cycle inhibitor Whi5 controls budding-yeast cell size. *Nature* 526(7572):268–272.
50. Harashima H, Sugimoto K (2016) Integration of developmental and environmental signals into cell proliferation and differentiation through RETINOBLASTOMA-RELATED 1. *Curr Opin Plant Biol* 29:95–103.
51. Turner JJ, Ewald JC, Skotheim JM (2012) Cell size control in yeast. *Curr Biol* 22(9):R350–R359.
52. Scofield S, Jones A, Murray JAH (2014) The plant cell cycle in context. *J Exp Bot* 65(10):2557–2562.
53. Coudercuse D, Nurse P (2010) Driving the cell cycle with a minimal CDK control network. *Nature* 468(7327):1074–1079.
54. Vermeer JEM, Van Munster EB, Vischer NO, Gadella TWJ, Jr (2004) Probing plasma membrane microdomains in cowpea protoplasts using lipidated GFP-fusion proteins and multimode FRET microscopy. *J Microsc* 214(Pt 2):190–200.
55. Grefen C, et al. (2010) A ubiquitin-10 promoter-based vector set for fluorescent protein tagging facilitates temporal stability and native protein distribution in transient and stable expression studies. *Plant J* 64(2):355–365.
56. Benková E, et al. (2003) Local, efflux-dependent auxin gradients as a common module for plant organ formation. *Cell* 115(5):591–602.
57. Shinohara N, Taylor C, Leyser O (2013) Strigolactone can promote or inhibit shoot branching by triggering rapid depletion of the auxin efflux protein PIN1 from the plasma membrane. *PLoS Biol* 11(1):e1001474.
58. Gruel J, et al. (2016) An epidermis-driven mechanism positions and scales stem cell niches in plants. *Sci Adv* 2(1):e1500989.
59. Green M, Krupinski P, Melke P, Sahlin P, Jönsson H (2008) Constanza: Confocal Stack Analyzer Application. Plant Image Analysis. Available at www.plant-image-analysis.org/software/constanza. Accessed October 1, 2016.
60. Fernandez R, et al. (2010) Imaging plant growth in 4D: Robust tissue reconstruction and lineaging at cell resolution. *Nat Methods* 7(7):547–553.

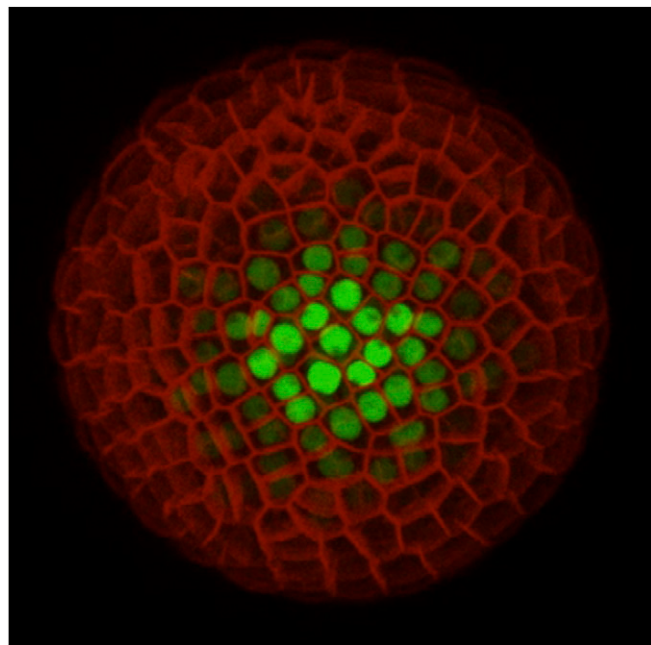
Supporting Information

Willis et al. 10.1073/pnas.1616768113



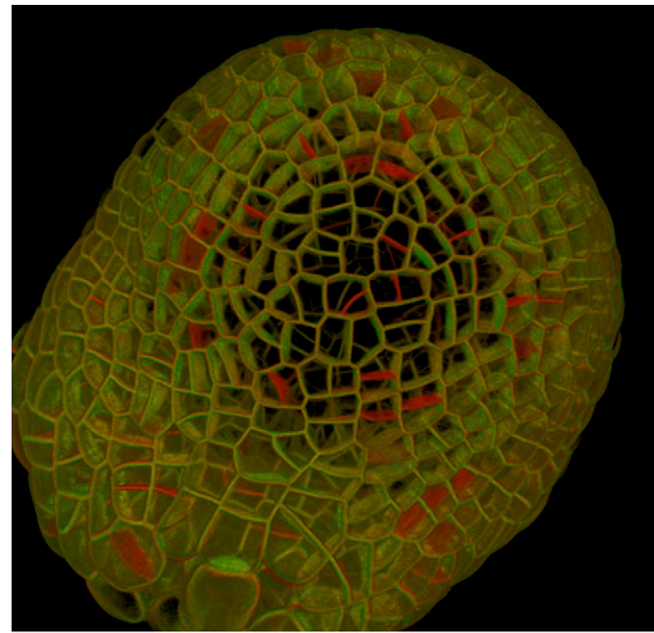
Movie S1. Time-lapse movie showing the membrane reporter (pUBQ10::acyl-YFP) in red and the *CLAVATA3* reporter (pCLV3::dsRED-N7) in green from SAM 4.

[Movie S1](#)



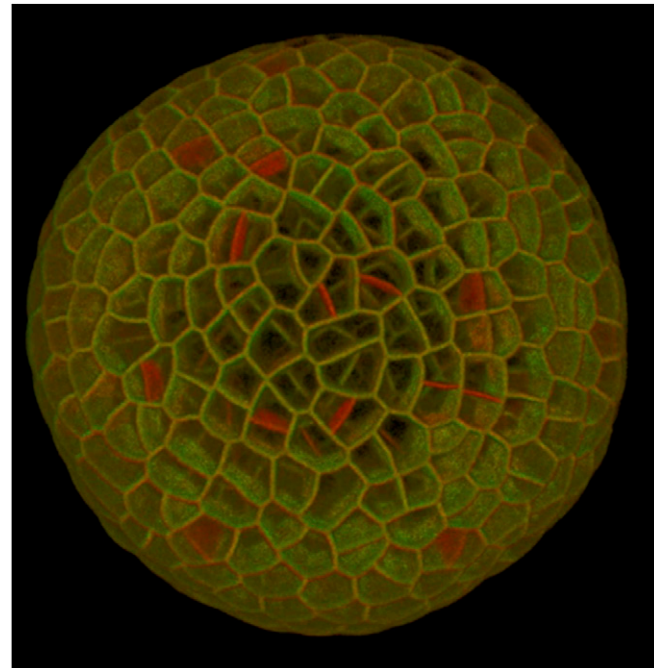
Movie S2. Time-lapse movie showing the membrane reporter (pUBQ10::acyl-YFP) in red and the *CLAVATA3* reporter (pCLV3::dsRED-N7) in green from SAM 5.

[Movie S2](#)



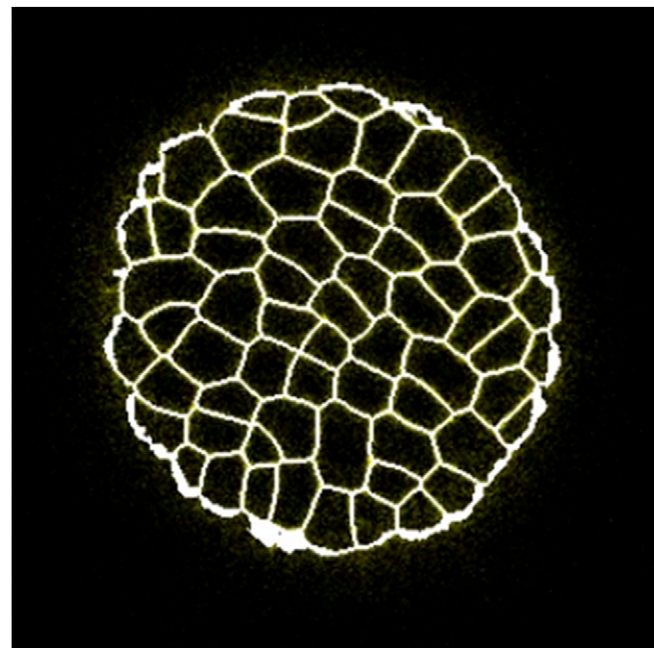
Movie S3. Time-lapse movie showing division patterns in SAMs 1. The new cell walls that appear at each time point are colored red.

[Movie S3](#)



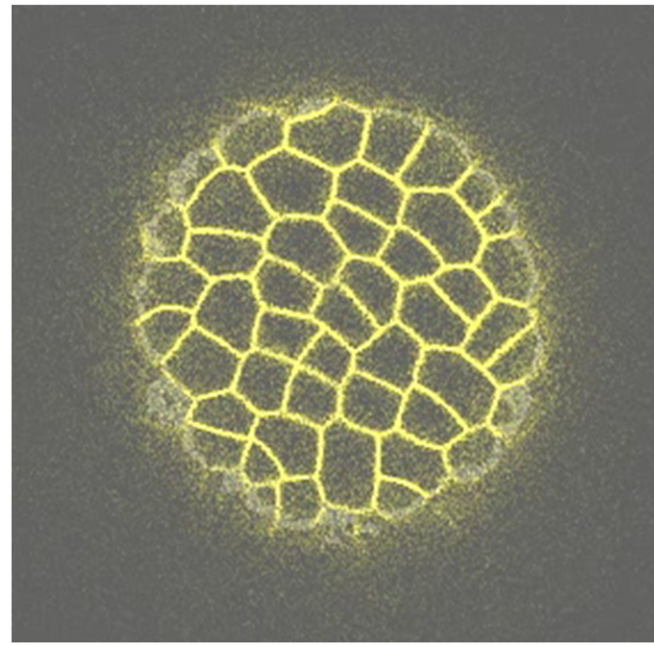
Movie S4. Time-lapse movie showing division patterns in SAM 4. The new cell walls that appear at each time point are colored red.

[Movie S4](#)



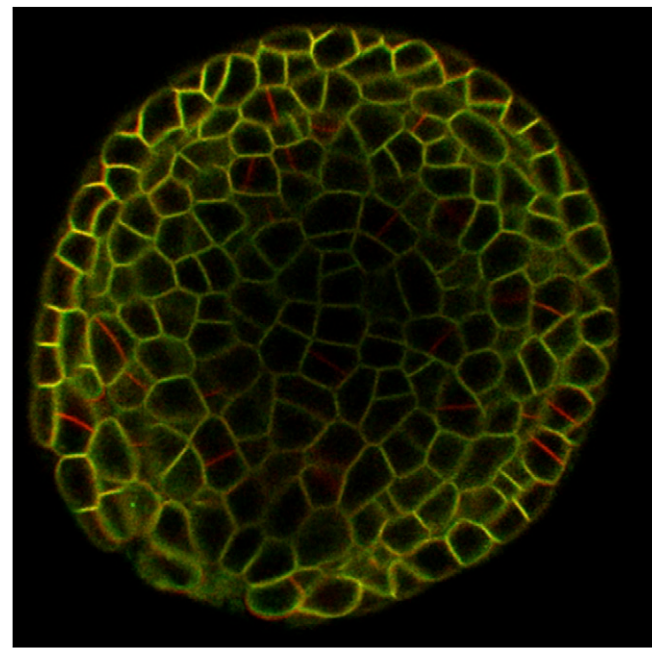
Movie S5. Movie used to check for segmentation errors. The movie shows walls from the segmentation overlaying the confocal z-stack of the pUB10::acyl-YFP membrane reporter of SAM 2 at $t = 68$ h; cells that have been incorrectly merged with one another or the background are evident by the lack of a white line segment. Four L1 cells at the base of the z-stack (start of the movie), which lie outside of the central zone and so were not included in our datasets, have been incorrectly merged with the background. Such movies were generated automatically and then manually checked at each time point to identify segmentation errors and to find optimal segmentation parameters that minimized errors.

[Movie S5](#)



Movie S6. Movie used to check for segmentation errors. The movie shows the inverted walls from the segmentation of SAM 2 at $t = 68$ h overlaying the confocal z-stack of the pUB10::acyl-YFP membrane reporter; one L1 cell has been incorrectly split, whereas all other L1 cells near the central zone are correctly split. Such movies were generated automatically and then manually checked at each time point to identify segmentation errors and to find optimal segmentation parameters that minimized errors.

[Movie S6](#)



Movie S7. The z-stack shows SAM 1 at $t = 0$ h registered onto SAM 1 at $t = 4$ h. The new cell walls are colored red. Such movies were used to check the registration quality.

[Movie S7](#)

Other Supporting Information Files

[SI Appendix \(PDF\)](#)

SI Appendix

“Cell size and growth regulation in the *Arabidopsis thaliana* apical stem cell niche”

Authors: Lisa Willis^{a,b,1}, Yassin Refahi^{a,1}, Raymond Wightman^a, Benoit Landrein^a, José Teles^a, Kerwyn Casey Huang^{b,c}, Elliot M Meyerowitz^{a,d}, Henrik Jönsson^{a,e,f,2}

¹Equal contributions

Author affiliations: ^aThe Sainsbury Laboratory, Cambridge University, Bateman Street, Cambridge, CB2 1LR, UK

^bDepartment of Bioengineering, Stanford University, Stanford, CA 94305, USA

^cDepartment of Microbiology and Immunology, Stanford University School of Medicine, Stanford, CA 94305, USA

^dHoward Hughes Medical Institute and Division of Biology and Biological Engineering 156-29, California Institute of Technology, Pasadena, CA 91125, USA

^eComputational Biology and Biological Physics, Lund University, Sölvegatan 14A, 223 62 Lund, Sweden

^fDepartment of Applied Mathematics and Theoretical Physics, Centre for Mathematical Sciences, Cambridge University, Wilberforce Road, Cambridge, CB3 0DZ, UK

²**Corresponding author:** Henrik Jönsson, The Sainsbury Laboratory, Cambridge University, Bateman Street, Cambridge, CB2 1LR, UK. Tel: +44(0)1223 761100.

Email: Henrik.Jonsson@slcu.cam.ac.uk

Keywords: cell size, cell growth, cell cycle, homeostasis, plant stem cells

Supplementary Materials and Methods

Pipeline for 4D cellular quantification and tracking using MARS/ALT. Confocal z-stacks were processed in a semi-automated pipeline. The ImageJ registration plugin StackReg (61) using the translation transformation was applied to each stack, to correct for misalignments between consecutive z-slices due to stage adjustments. Any z-slices that contained horizontal shifts due to sudden large vibrations or stage movements during z-stack acquisition were identified, then automatically replaced with the closest z-slice that had no horizontal shift (~1-5% slices); this process helped to eliminate segmentation errors. A potential major source of cellular quantitation error is the upward movement of the plantlet during z-stack acquisition due to stem elongation: for most time-points, the plantlet gained height in the z-direction at a velocity comparable to that of the confocal scan-head, which resulted in an artificially stretched SAM by a mean factor of ~1.3, with a maximum stretching factor of ~2.3 (*SI Appendix*, Fig. S24; Table S10). To correct this artifact, z-slices of the low-z-resolution stack (z-step = 5-6 μm), which was not artificially stretched and which was acquired immediately after the high z-resolution stack (z-step = 0.25 μm), were matched with corresponding z-slices of the high-z-resolution z-stack to compute and correct for the stretching.

To remove noise from the processed z-stacks, we applied a Gaussian filter and an alternative-sequential filter (ASF). These filtered z-stacks were segmented (independently of z-stacks at other time-points) using a 3D watershed algorithm from MARS [1]. The watershed seeds were determined using the h-minima operator, which computes local minima regions in the filtered z-stacks. For a visual assessment of segmentation quality, cell boundary stacks were computed from the segmentations using a 3D Laplace filter from the SciPy library then the cell boundary

stacks and processed z-stacks were merged with different colors into a single stack in ImageJ. This merged stack was visually inspected for segmentation errors (Movies S5-S6). In case of a segmentation error (over-segmentation, under-segmentation, missed cell, or shape error), we changed the parameters of the Gaussian and ASF filters as well as the h-minima parameter of the segmentation algorithm to optimize segmentation of the L1 layer. In the optimal segmentations, the lower layers of the central and peripheral zones were also mostly error free.

For this exposition, we define I_t and $I_{t+\Delta t}$ as the processed z-stacks from two consecutive confocal acquisitions, and S_t and $S_{t+\Delta t}$ as the corresponding optimal segmentations. To track cell lineages between S_t and $S_{t+\Delta t}$, we first computed the affine transformation that linearly registered I_t onto $I_{t+\Delta t}$ using the block-matching framework (62-64). The affine transformation was then used to initialize the block-matching algorithm to compute the non-linear transformation $T_{I_t \leftarrow I_{t+\Delta t}}$, a vector field that was used for the final registration between segmentations S_t and $S_{t+\Delta t}$. For a visual assessment of the quality of registration, we imported the reference image $I_{t+\Delta t}$ and the registered floating image $I_t \circ T_{I_t \leftarrow I_{t+\Delta t}}$ into ImageJ and merged them with different colors (red: $I_{t+\Delta t}$, green: $I_t \circ T_{I_t \leftarrow I_{t+\Delta t}}$) into a single image (Movie S7). Registration quality was then visually verified by inspecting this merged image in 3D. Registration was perfect for 138/140 pairs of consecutive images, reflecting the fact that the image-acquisition frequency ($\Delta t = 4$ h) had sufficiently high temporal resolution. To compute mother-daughter cell pairings between consecutive time-points, the non-linear registration was applied to S_t (i.e. $S_t \circ T_{I_t \leftarrow I_{t+\Delta t}}$), then ALT (60) was used to compute the optimal mother-daughter pairing between $S_t \circ T_{I_t \leftarrow I_{t+\Delta t}}$ and $S_{t+\Delta t}$. When ALT failed (2/140 pairs of consecutive time-points), we manually paired mother and daughter cells. The optimal pairing was then used to generate color maps in which the mother

and daughter cells had the same color code. These color maps were used to visualize the segmentations and visually verify computed lineages (Fig. 1A).

Volume and surface area quantification and validation. In the 3D segmented z-stacks, voxels belonging to the same cell were marked by the same label. Cell volumes were computed by counting the number of voxels with the same label, and multiplying this count by the given voxel volume. Accurate estimation of cell surface area was more challenging (65-67). To extract cell surfaces, we used the marching cubes algorithm from the Visualization Toolkit (VTK) version 5.8 (68), which generated triangular meshes of cell surfaces. Cell surface area was computed after decimating the mesh (while preserving cell-cell topology), and then Laplacian smoothing the mesh using algorithms from VTK v. 5.8. To assess the accuracy of surface area quantification, we generated digitized synthetic spheres, cylinders, and cubes of different dimensions on a 3D grid of $0.25 \times 0.25 \times 0.25 \mu\text{m}^3$ voxels to match the resolution of our confocal z-stacks. For different shapes of the same volume as the average cell of the meristem ($\sim 160 \mu\text{m}^3$), the error was <5%.

Nuclear volume quantification. The nuclear-localized pCLV3::dsRED-N7 reporter was used to segment L1 nuclei in the center of SAMs #2-6. Prior to segmentation, the pCLV3::dsRED-N7 channels of all confocal z-stacks were deconvolved to remove fluorescence artifacts due to the confocal microscope's point-spread function (PSF). Deconvolution was performed using Huygens software version 15.05 (Scientific Volume Imaging, Hilversum, Netherlands); the Huygens tool "PSF distiller" was used to create an experimental PSF from images of 100-nm fluorescent beads that were acquired using the same settings as for the SAM time-lapses. The deconvolved z-stacks were corrected for artificial stretching, as described in the pipeline above, then segmented

using the in-house software Constanza (59). The reduction in the signal from the *CLAVATA3* reporter with radial distance from the center of each SAM meant that only the 6-9 cells within a radius of 8 μm of the SAM's center could be accurately segmented (*SI Appendix*, Fig. S23); within this short range, the effect of the diminishing *CLAVATA3* signal on nuclear segmentation accuracy was small (Fig. 3B).

Text S1: Relations between cell volume and surface area growth rates over the cell cycle.

Epidermal (L1) SAM cells expand in the plane of the tissue's surface while maintaining an approximately constant height in the perpendicular direction. These geometric constraints, along with the observation that cells do not substantially alter their shape over the cell cycle (Fig. 1A), necessitate the following power-law relations between a cell's volume, V , and the areas of its anticlinal and inner periclinal walls, A_a and A_{ip} , respectively,

$$A_a \sim V^{1/2}, \quad A_{ip} \sim V$$

as validated in *SI Appendix*, Table S7. Similarly, volume was expected to scale proportionally with the outer periclinal wall area A_{op} ; data in *SI Appendix*, Table S7 show that the scaling is sub-linear ($A_{op} \sim V^{0.8}$). The total area, A , scales as $A \sim V^{2/3}$, as expected. Given these power-law relations and that volume increases exponentially (at a constant relative rate) over the cell cycle, we have for a given size metric $S \sim V^{\lambda}$

$$d(\ln V)/dt = k \Rightarrow d(\ln S^{1/\lambda})/dt = k \Rightarrow d(\ln S)/dt = k\lambda.$$

Therefore, the wall surface areas A , A_{op} , A_{ip} , and A_a should each increase exponentially over the cell cycle at a relative growth rate that is $\sim 2/3$ -fold, ~ 0.8 -fold, ~ 1 -fold, and $\sim 1/2$ -fold the relative growth rate of V respectively. These predictions are corroborated by our data (*SI Appendix*, Fig. S18).

Text S2: Quantitative characterization of cell-size regulation in non-homeostatic

conditions. To quantitatively characterize cell-size regulation, it was important to consider cell-size metrics with mean values that do not vary substantially with space across the SAM or with time during data acquisition, since such variability if not properly accounted for can lead to

incorrect conclusions (*SI Appendix*, Fig. S8). First, among L1 cells in the SAM <30 μm from O (the center of the SAM which coincides with the peak of *CLAVATA3* expression and slowest cell growth rates), we verified that the normalized cell volume (cell volume divided by mean cell volume at the corresponding time-point t denoted μ_V^t) does not vary with space or time (*SI Appendix*, Fig. S3). Second, we reasoned that since sister cells are born simultaneously and at the same position within the SAM, the difference in sister-cell size metrics normalized by the sum of these metrics, $(S - S^{\text{sis}})/(S + S^{\text{sis}})$ where S can correspond to volume V or wall areas including A , A_a , A_{ip} or A_{op} , should have minimal spatiotemporal variation for all cell-size metrics. *SI Appendix*, Table S2 contains validation of this reasoning; there is a weakly significant variation of $(S - S^{\text{sis}})/(S + S^{\text{sis}})$ with time that disappears when cells born late in the time-lapse are removed from the sample, indicating that this correlation is an artifact generated by the finite duration of the experiment. Our results are unaffected by whether or not cells born late in the time-lapse are included in the sample (*SI Appendix*, Table S6).

Under the assumption that within a sample all cells grow to the same mean size, a Taylor expansion around the mean birth size characterizes the rule for cell size regulation. Under the assumption of small fluctuations about the mean birth size, a first-order approximation is valid (4),

$$(1) \quad S_d \approx \mu_d^S + f(S_b - \mu_b^S) \approx f S_b + (\mu_d^S - f \mu_b^S),$$

where S_b , S_d are the cell sizes at birth and division respectively, μ_d^S , μ_b^S are the mean division and birth sizes respectively, and f is the slope of S_b vs. S_d evaluated at $S_b = \mu_b^S$. Substituting Eq. (1) for both a cell and its sister, we obtain a relation between α_d , the sister-size asymmetry at division, and α_b , the sister-size asymmetry at birth,

$$(2) \quad \alpha_d = (S_d - S_d^{\text{sis}})/(S_d + S_d^{\text{sis}}) \approx f \times (S_b + S_b^{\text{sis}})/(S_d + S_d^{\text{sis}}) \times (S_b - S_b^{\text{sis}})/(S_b + S_b^{\text{sis}})$$

$$= f (S_b + S_b^{\text{sis}})/(S_d + S_d^{\text{sis}}) \alpha_b.$$

Therefore, under the assumption that α_b^2 is independent of $(S_b + S_b^{\text{sis}})/(S_d + S_d^{\text{sis}})$ (*SI Appendix*, Fig. S25 shows that, except for A_{ip} , these variables are uncorrelated; the weak correlation for A_{ip} is likely due to outliers; $n = 415$, $p = 0.011\text{-}0.99$),

$$E[\alpha_d \alpha_b] \approx f E[(S_b + S_b^{\text{sis}})/(S_d + S_d^{\text{sis}}) \alpha_b^2] = f E[(S_b + S_b^{\text{sis}})/(S_d + S_d^{\text{sis}})] \times E[\alpha_b^2],$$

where $E[\bullet]$ denotes the mean. The slope of a least-square linear fit to α_b vs. α_d is given by

$$E[\alpha_d \alpha_b]/E[\alpha_b^2] = f E[(S_b + S_b^{\text{sis}})/(S_d + S_d^{\text{sis}})] \approx f/2,$$

due to the observation that for all size metrics, $E[(S_b + S_b^{\text{sis}})/(S_d + S_d^{\text{sis}})] \approx 1/2$ (*SI Appendix*, Table S5). Similarly, the slope of a least-square linear fit to α_b vs. $\alpha_\Delta = (\Delta - \Delta^{\text{sis}})/(\Delta + \Delta^{\text{sis}})$, where Δ , Δ^{sis} are the size increments added between birth and division for a cell and its sister, respectively, is given by

$$E[\alpha_\Delta \alpha_b]/E[\alpha_b^2] = (1 - f) E[(S_b + S_b^{\text{sis}})/(\Delta + \Delta^{\text{sis}})] \approx 1 - f,$$

due to the observation that for all size metrics, $E[(S_b + S_b^{\text{sis}})/(\Delta + \Delta^{\text{sis}})] \approx 1$ (*SI Appendix*, Table S5).

Data from Tables S3 and S5 show that all cell volume statistics, V_b vs. V_d (normalized and non-normalized) and α_b vs. α_d , consistently predict that $f \approx 0.5$. Surface area size metrics A_{op} , A_{ip} , and A_a change strongly with Euclidean distance from O (Fig. 2A, *SI Appendix*, Fig. S5-S7) so the corresponding f parameters cannot be simply extracted from a plot of e.g. $A_{op,b}$ vs. $A_{op,d}$; for wall area size metrics, f was extracted from plots of α_b vs. α_d and α_b vs. α_Δ by applying the relations above. In all cases, we obtained $f \approx 0.5$ (*SI Appendix*, Table S5). We note that for all size metrics, the division size is the sum of the size of both daughter cells at the time when the new cell wall first becomes visible, i.e. when the new cell wall first becomes detectable by the segmentation

algorithm. Asymmetry statistics included all sister-cell pairs that were tracked over a complete cell cycle within 45 μm of O .

Text S3: Simulations of the regulation of cell size and growth. We extended and simulated a stochastic model of cell-autonomous regulation of growth and inter-division timings (4, 37) to compute pairwise correlations among cell-size variables for comparison with our experimental data. In the simulations, each cell from a population of n_{model} cells has a discretized position denoted by x , and is born and divides within a discretized generation denoted by t . For a cell at position x , its dimensionless birth and division sizes are denoted by $S_b(x,t)$ and $S_d(x,t)$, respectively, and the cell grows at a constant relative rate that depends on the degree of asymmetric division of the mother cell for the duration of the cell cycle with an inter-division time of $T(x,t)$. From an initial starting configuration of n_{model} birth sizes at generation $t = 0$, the following equations are iterated for 20 generations, until cell size and inter-division time statistics have reached steady states:

$$(1) \quad S_d(x, t) = f S_b(x, t) + 2 - f + Z(x, t), \quad Z \sim N(0, \sigma)$$

$$(2) \quad T(x, t) = \log_2(S_d/S_b)/(1 - g_{\text{asym}} \alpha_b) \quad \text{where } \alpha_b(x, t) = (S_b - S_b^{\text{sis}})/(S_b + S_b^{\text{sis}})$$

S_b^{sis} being the sister of the cell at (x, t)

for $x = 0, \dots, n_{\text{model}} - 1$,

$$(3) \quad \text{for } x < N_{\text{model}}/2, \quad S_b(2x + 1, t + 1) = S_d(x, t)(1/2 + Z_a(x, t))$$

$$S_b(2x, t + 1) = S_d(x, t)(1/2 - Z_a(x, t)), \quad Z_a \sim N(0, \sigma_a),$$

i.e., cells at $2x$ and $2x+1$ are sisters.

The fixed parameters f (size regulation), σ (noise), g_{asym} (the strength of the dependence of relative growth rate on mother-cell asymmetric division), and σ_a (frequency of asymmetric

division) are described below. We assumed Gaussian distributions for the noise in cell-size regulation and asymmetric divisions, and a mean cell size and a mean relative growth rate that have no spatiotemporal variation. Pairwise correlations and least-square linear fits between S_b vs. S_d , α_b vs. α_d , and α_b vs. $\alpha_T = (T - T^{\text{sis}})/(T + T^{\text{sis}})$, where T , T^{sis} are inter-division times of a cell and its sister, respectively, along with other statistics are computed from the final generation of n_{model} cells only. Each instance of the simulation was run with n_{model} cells to approximately match the sample size of the experimental data ($n_{\text{model}} = 800$ for sister asymmetry statistics; $n_{\text{model}} = 1000$ for non-sister asymmetric statistics). Each of the parameters f , σ , σ_a , and g_{asym} were extracted from cell volume experimental data as described below.

Extracting f (the mode of cell size regulation). f is equal to the slope of V_b/μ_V^t vs. V_d/μ_V^t (normalized volumes; *SI Appendix*, Table S3). Bootstrapping (69) the sample of birth and division normalized volumes for L1 central zone cells tracked over a full cell cycle estimated the median (0.48) and 90% confidence interval ([0.42, 0.55]) of f from least-square linear fits to be (0.48, [0.42, 0.55]). Throughout this work, bootstrapping was performed by sampling with replacement from data until the sample size was matched; sampling was repeated 10,000 times to estimate the distribution of the statistic of interest.

Extracting σ (the noise in cell-size regulation). Computing the variance of each side of the equation labeled (1) in the algorithm above gives $\text{var}(S_d) = f^2 \text{var}(S_b) + \sigma^2$. S_b and S_d are dimensionless size variables corresponding to normalized V_b/μ_b and $V_d/\mu_b \approx V_d/\mu_d \times \mu_d/\mu_b$. Therefore,

$$\sigma^2 \approx (\mu_d/\mu_b)^2 \sigma_d^2 - f^2 \sigma_b^2,$$

where σ_d and σ_b are the coefficients of variation of cell birth and division normalized volumes, respectively. Bootstrapping the normalized birth and division volumes for L1 central zone cells tracked over a full cell cycle provided estimates of the medians and 90% confidence intervals for σ_d , σ_b , and σ to be (0.14, [0.128, 0.147]), (0.25, [0.239, 0.262]), and (0.227, [0.214, 0.243]), respectively.

Extracting σ_a (the frequency of asymmetric division). The pair of equations labeled (3) in the algorithm above together give

$$\sigma_a^2 = \text{var}((S_b - S_b^{\text{sis}})/2(S_b + S_b^{\text{sis}})),$$

(SI Appendix, Table S1). Bootstrapping the L1 central zone sister-cell pair normalized volumes tracked over a full cell cycle provided estimates of the median and 90% confidence interval of σ_a to be (0.105, [0.099, 0.111]).

Extracting g_{asym} (the strength of the dependence of relative growth rate on mother-cell asymmetric division). Our data indicated that cells grow at a constant relative rate or constant rate per unit size over their cell cycles, with small sisters growing at faster rates than their large sisters. To first order, this dependence can be expressed as

$$g_{\text{rel}}/\mu_g = 1 - g_{\text{asym}} a_b,$$

where g_{rel} is the relative growth rate and μ_g is the mean growth rate over the entire sample. The mean relative growth rate of normalized volume over the cell cycle was computed as

$$\langle g_{\text{rel}} \rangle / \mu_g = \langle (V(t+1)/\mu_V^{t+1} - V(t)/\mu_V^t) / 0.5(V(t+1)/\mu_V^{t+1} + V(t)/\mu_V^t) \rangle / \mu_g.$$

Bootstrapping the sample of $(a_b, \langle g_{\text{rel}} \rangle / \mu_g)$ for L1 central zone sister-cell pairs tracked over a full cell cycle estimated the median and 90% confidence interval of g_{asym} , the negative of the slope of

α_b vs. $\langle g_{\text{rel}} \rangle / \mu_g$, from least-square linear fits to be (0.43, [0.365, 0.496]). Note that the deviation in relative growth rates in the relationship between α_b vs. $\langle g_{\text{rel}} \rangle / \mu_g$ from $1 - g_{\text{asym}} \alpha_b$ (inset, Fig. 4A) is partially accounted for by the variation in mean relative growth rate with distance from O (*SI Appendix*, Fig. S16). The statistics pertaining to α_b vs. α_T , with which the model is compared, are independent of this spatial variation, and so this effect was not included in the simulations. The medians and 90% confidence intervals of f , σ , σ_a , and g_{asym} derived from bootstrapping were used to generate the plots of Fig. 5 and data in *SI Appendix*, Table S9.

To produce the statistics in *SI Appendix*, Table S9, 1000 simulations generated medians and 90% confidence intervals of various statistics, including the coefficients of variation in cell birth size and cell division size σ_b , σ_d and the least-square linear fit between α_b and α_T . These statistics were in close agreement with the experimental data (Fig. 5, *SI Appendix*, Table S9). In Fig. 5A, trajectories of the ratios of large to small sister-cell sizes over the cell cycle were plotted for a single instance of the simulation using parameter values for the medians of f , σ , σ_a , and g_{asym} estimated from bootstrapping; the inset shows birth size versus division size for a single instance of the simulation. Fig. 5B shows median values and 90% confidence intervals (grey shaded regions) of the statistic specified in each column, as generated by the simulations. In panels (i)-(iii), parameters $\sigma = 0.227$ and $\sigma_a = 0.105$ were held at their experimentally measured values while f (horizontal axes) and g_{asym} (different grey shades; dark to light shades correspond to $g_{\text{asym}} = -0.03 - 0.1 \times i$ for $i = 0, \dots, 8$) were varied. In panels (iv)-(vi), parameters $f = 0.48$ and $\sigma_a = 0.105$ were held at their experimentally measured values while σ (horizontal axes) and g_{asym} (different grey shades; dark to light shades correspond to $g_{\text{asym}} = -0.03 - 0.1 \times i$ for $i = 0, \dots, 8$) were varied. The dashed blue lines (blue shaded regions) denote experimentally measured

medians (90% confidence intervals) for parameters estimated by bootstrapping, and the dashed red lines (red shaded regions) denote experimentally measured medians (90% confidence intervals) for the statistic specified in each column.

Our simulations indicate that the experimental data is consistent with a cell-autonomous model of the regulation of growth and size, and that the dependence of relative growth rate on the mother-cell asymmetric division, parametrized by g_{asym} , is required to account for the statistical trends in the experimental data.

References:

61. Thevenaz P, Ruttimann UE, & Unser M (1998) A pyramid approach to subpixel registration based on intensity. *IEEE Trans. Image Process.* 7(1):27-41.
62. Ourselin S, Roche A, Prima S, & Ayache N (2000) Block matching: A general framework to improve robustness of rigid registration of medical images. in *International Conference on Medical Image Computing and Computer-Assisted Intervention*. (Springer Berlin Heidelberg), pp 557-566.
63. Commowick O, Grégoire V, & Malandain G (2008) Atlas-based delineation of lymph node levels in head and neck computed tomography images. *Radiother. Oncol.* 87(2):281-289.
64. Michelin G, et al. (2016) Spatiotemporal registration of 3D microscopy image sequences of Arabidopsis floral meristems. In *IEEE 13th International Symposium on Biomedical Imaging (ISBI)* pp. 1127-1130.
65. Thompson KE (2007) Computing particle surface areas and contact areas from three-dimensional tomography data of particulate materials. *Part. Part. Syst. Charact.* 24(6):440-452.
66. Lindblad J (2005) Surface area estimation of digitized 3D objects using weighted local configurations. *Image Vis. Comput.* 23(6):111-122.
67. Windreich G, Kiryati N, & Lohmann G (2003) Voxel-based surface area estimation: from theory to practice. *Pattern Recogn.* 36(11):2531-2541.
68. Schroeder W, Martin K, & Lorensen B (2006) *The Visualization Toolkit* (Kitware, Inc., New York) 4th Ed.
69. Efron B (1979) Bootstrap methods: Another look at the jackknife. *Ann. Stat.* 7(1):1-26.

Supplementary Figures:

In all supplementary figures and tables, N is the sample size; sl., int. are the slope and intercept, respectively, of a least-square linear fit; R is the Pearson correlation coefficient with a corresponding p -value denoted by p .

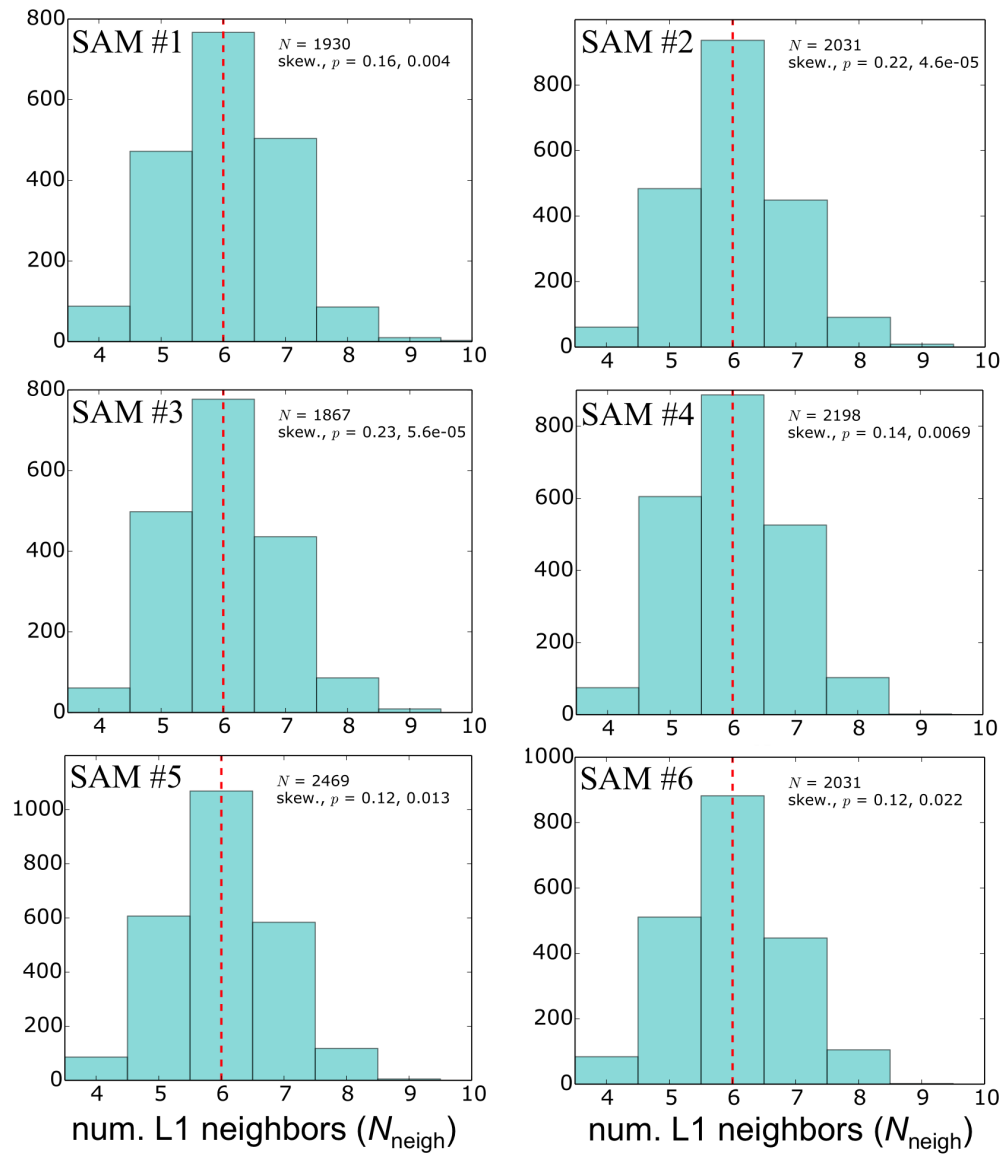


Fig. S1: Number of neighbor distributions in the meristem epidermis. The time-averaged distributions of number of L1 neighbors (N_{neigh}) for cells in the central zone are similar to those of other studies (32, 33), with medians (red dashed lines) of six L1 neighbors for all SAMs. Number of L1 neighbors for cells $<30 \mu\text{m}$ from O and for all time-points were amalgamated to generate these histograms.

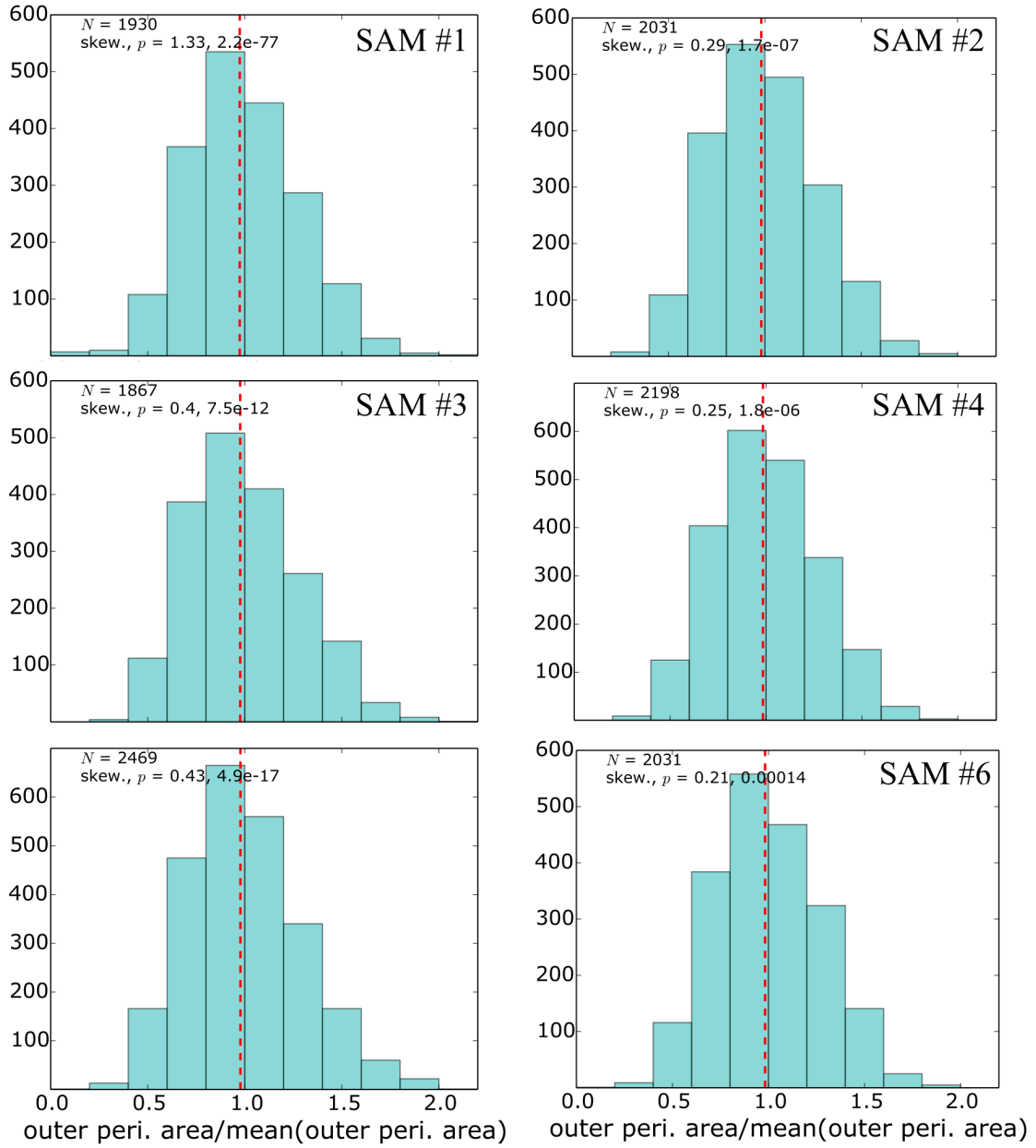


Fig. S2: Periclinal wall area distributions. The time-averaged distributions of outer periclinal wall areas of L1 central zone cells that are similar to other studies (34), with weighted left tails as demonstrated by the significant positive skewnesses,. All cells <30 μm from O and all time-points were amalgamated to generate these histograms.

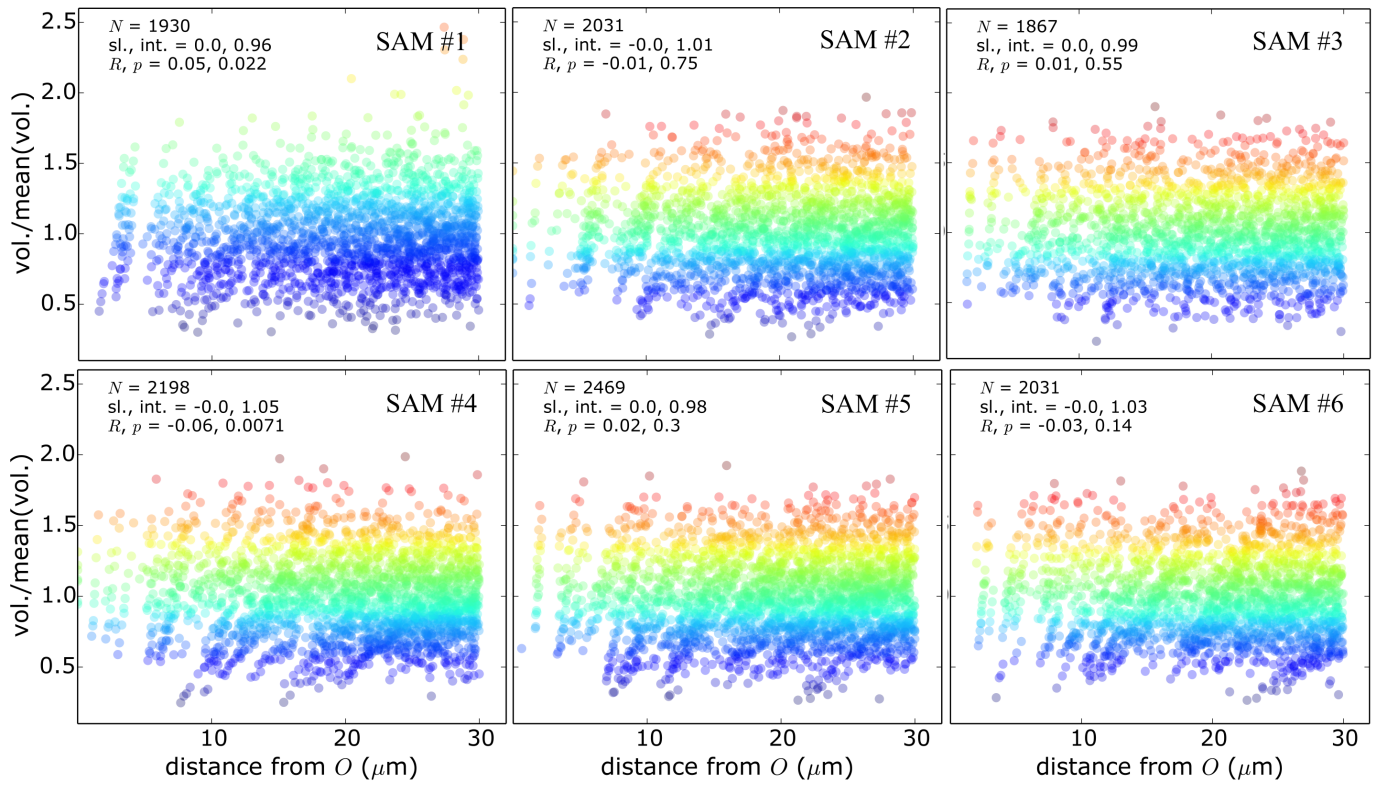


Fig. S3: Mean cell volume did not vary with position in SAM central zones. For each SAM central zone (cells within radius 30 μm of the SAM center at O), cell volumes (V) are constant with Euclidean distance from O. Data from each time-point were amalgamated to generate these plots. Cells are colored according to cell volume, with each panel corresponding to a distinct SAM.

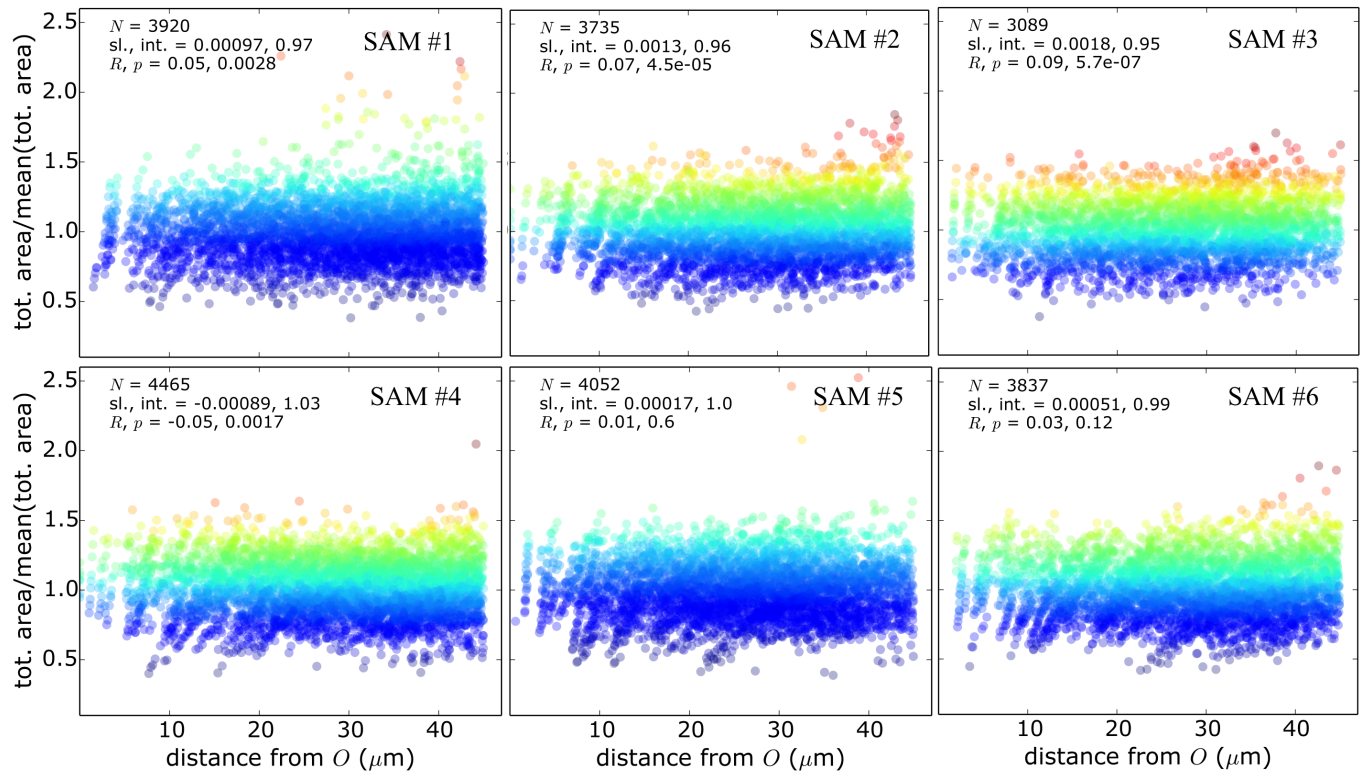


Fig. S4: Mean total cell wall area did not vary with position in SAM central zones. For each SAM central zone, total surface areas (A) are constant with Euclidean distance from O . Data from each time-point were amalgamated to generate these plots. Cells are colored according to volume (as in Fig. S3), with each panel corresponding to a distinct SAM.

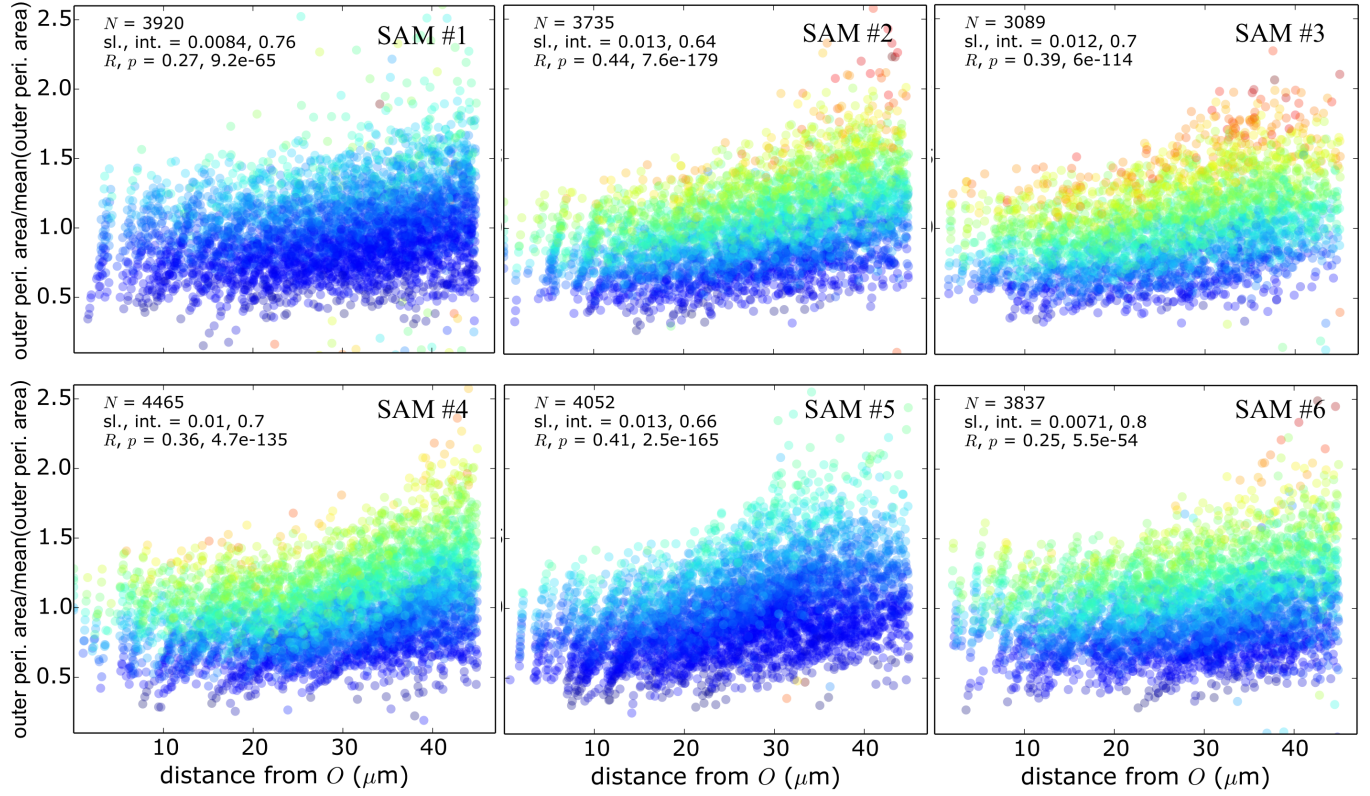


Fig. S5: Mean outer periclinal wall area increased with distance from the SAM center. For each SAM central zone, outer periclinal wall areas (A_{op}) increase with distance from O . The slope from a least-square linear fit indicated that outer periclinal wall areas change by ~1.6-fold between the center and the periphery of the SAM, with most of the change occurring between 30 and 45 μm . Data from each time-point were amalgamated to generate these plots. Cells are colored according to volume (as in Fig. S3), with each panel corresponding to a distinct SAM.

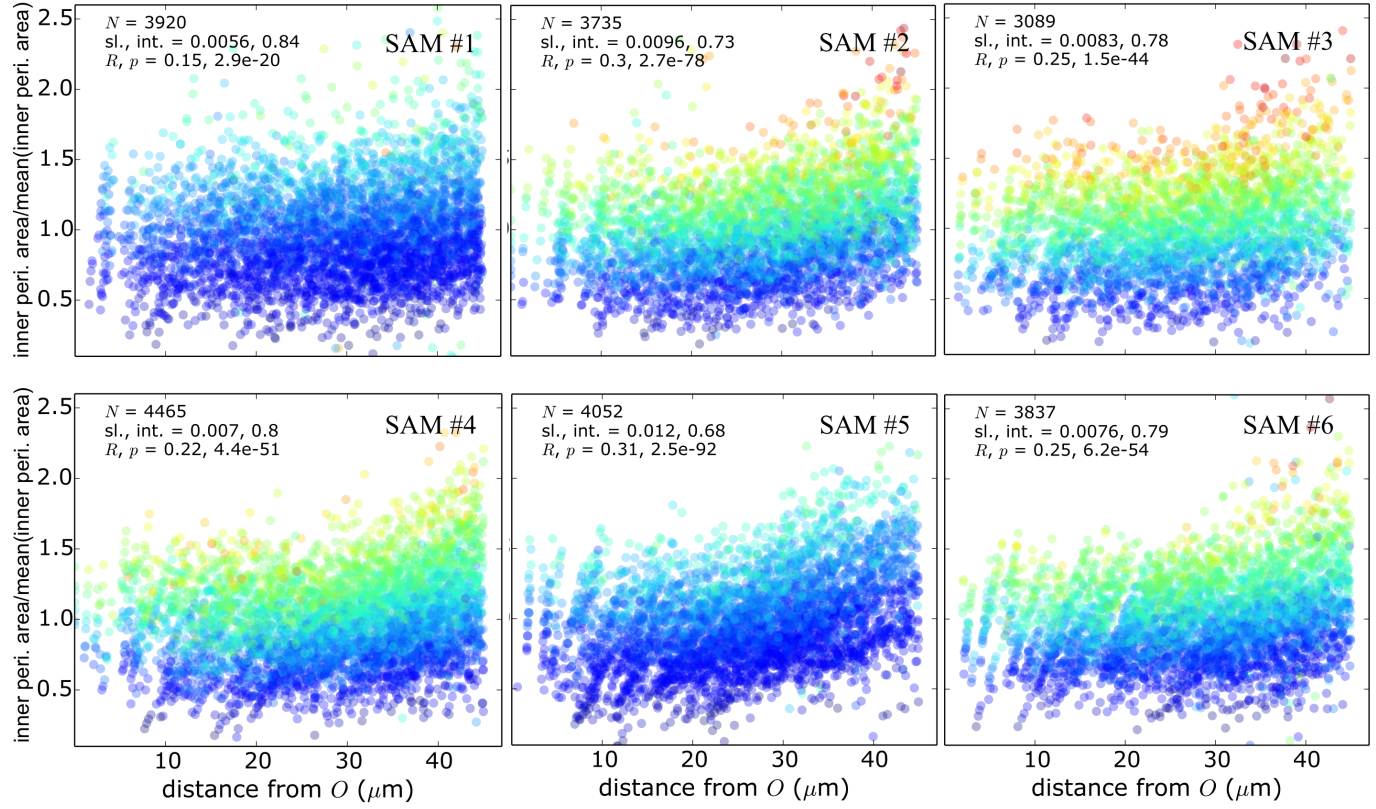


Fig. S6: Mean inner periclinal wall area increased with distance from the SAM center. For each SAM central zone, inner periclinal wall areas (A_{ip}) change by ~ 1.6 -fold between the center and the periphery of the SAM, with most of the change occurring between 30 and 45 μm . Data from each time-point were amalgamated to generate these plots. Cells are colored according to volume (as in Fig. S3), with each panel corresponding to a distinct SAM.

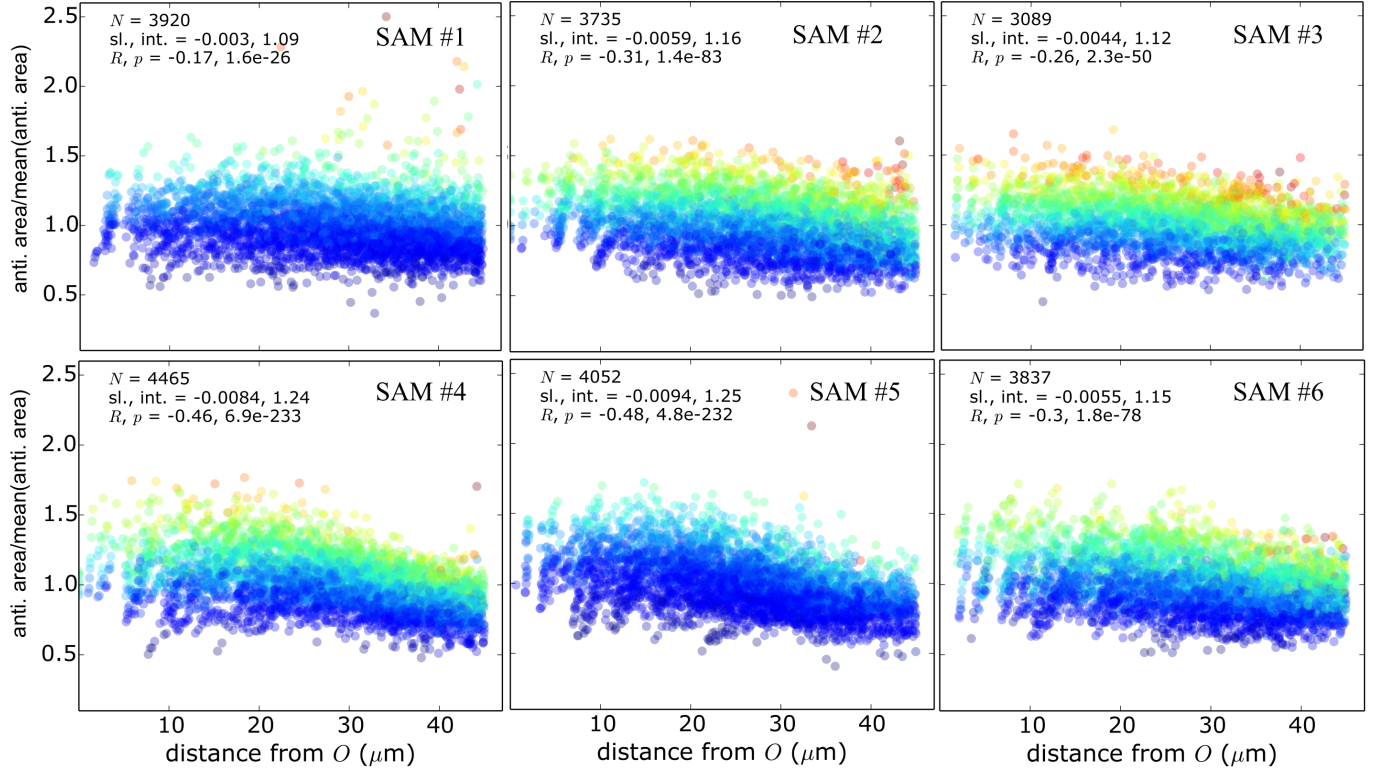
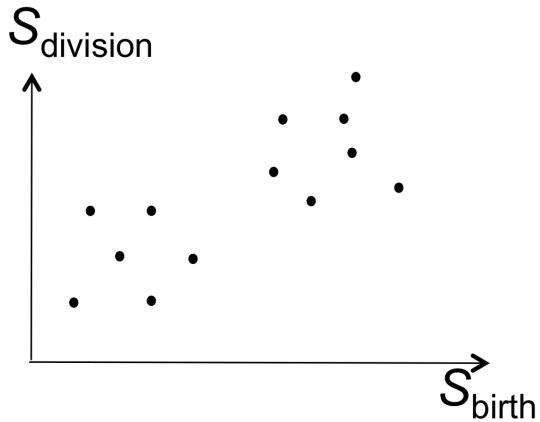


Fig. S7: Mean anticalinal wall area decreased with distance from the SAM center. For each SAM central zone, anticalinal wall areas (A_a) change by ~0.8-fold, with most of the change occurring between 30 and 45 μm . Data from each time-point were amalgamated to generate these plots. Cells are colored according to volume (as in Fig. S3), with each panel corresponding to a distinct SAM.

observed data



shows correlation > 0

true data



has correlation 0 for each population

Fig. S8: Previous studies relied on cell size homeostasis to infer the rule for size regulation. In studies of single-celled organisms in homeostatic environments, to determine whether cells regulate their size according to a critical size, critical increment, or fixed time mode, birth size is compared against division size/size increment: a positive/zero correlation implies a critical increment mode, while a zero/negative correlation implies a critical size mode. However, if the data set is comprised of two or more populations with some cells growing to a larger mean target size, the presence of multiple populations may generate correlations among birth and division size metrics, potentially leading to incorrect conclusions about the mode of size regulation. Therefore, since in our data some cell size metrics have spatiotemporal variation, it was important to focus on cell size statistics chosen to eliminate this variation.

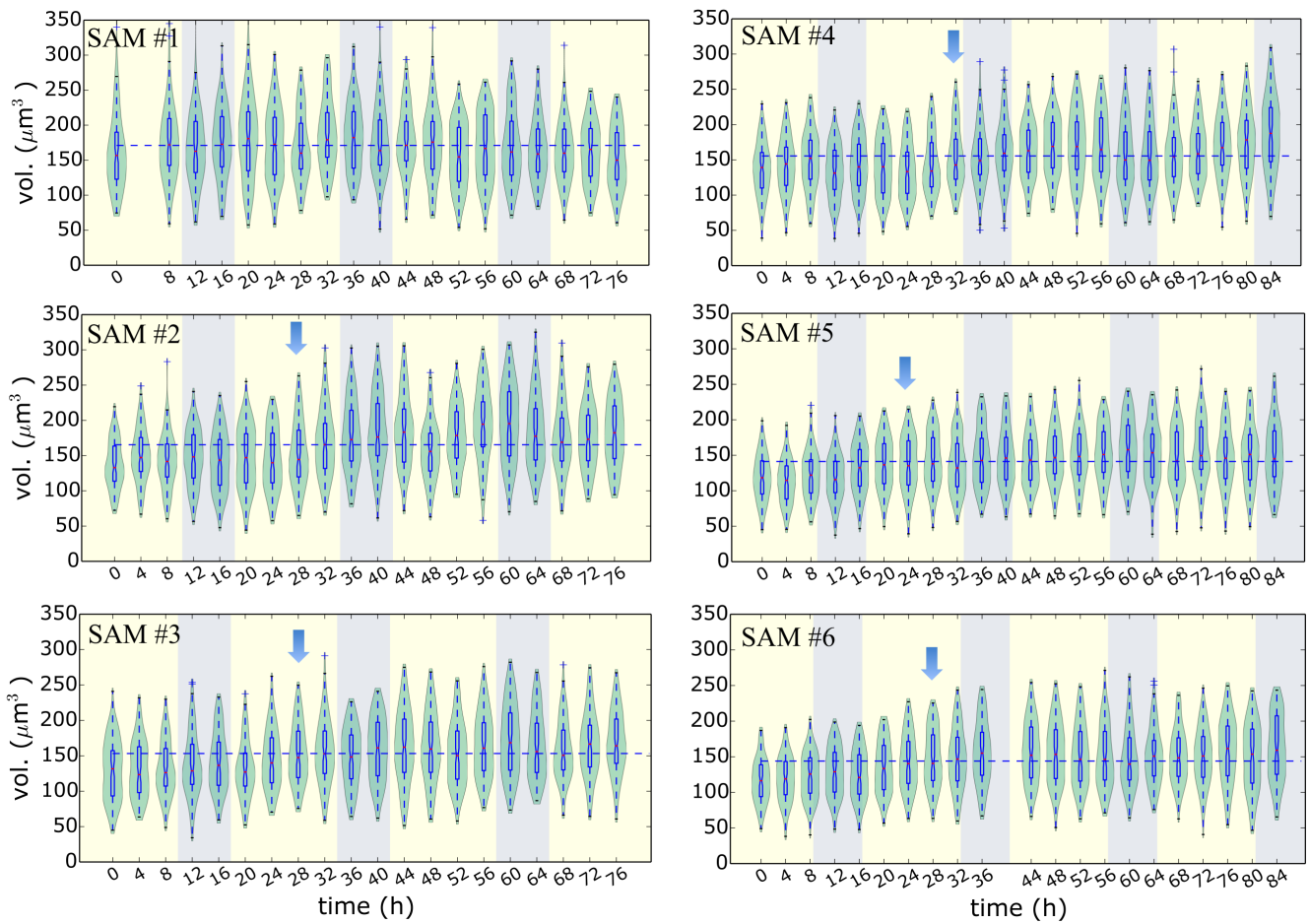


Fig. S9: Cell volume varied over time in individual SAMs. In 5/6 SAMs, a ~20% increase in mean volume of L1 cells in the central zone (blue arrows) occurred 16–32 h into the time-lapse. The horizontal blue dashed line indicates the mean volume of the time-averaged distribution of central zone L1 cell volumes. Yellow/blue shading corresponds to 16 h/8 h periods of light/dark.

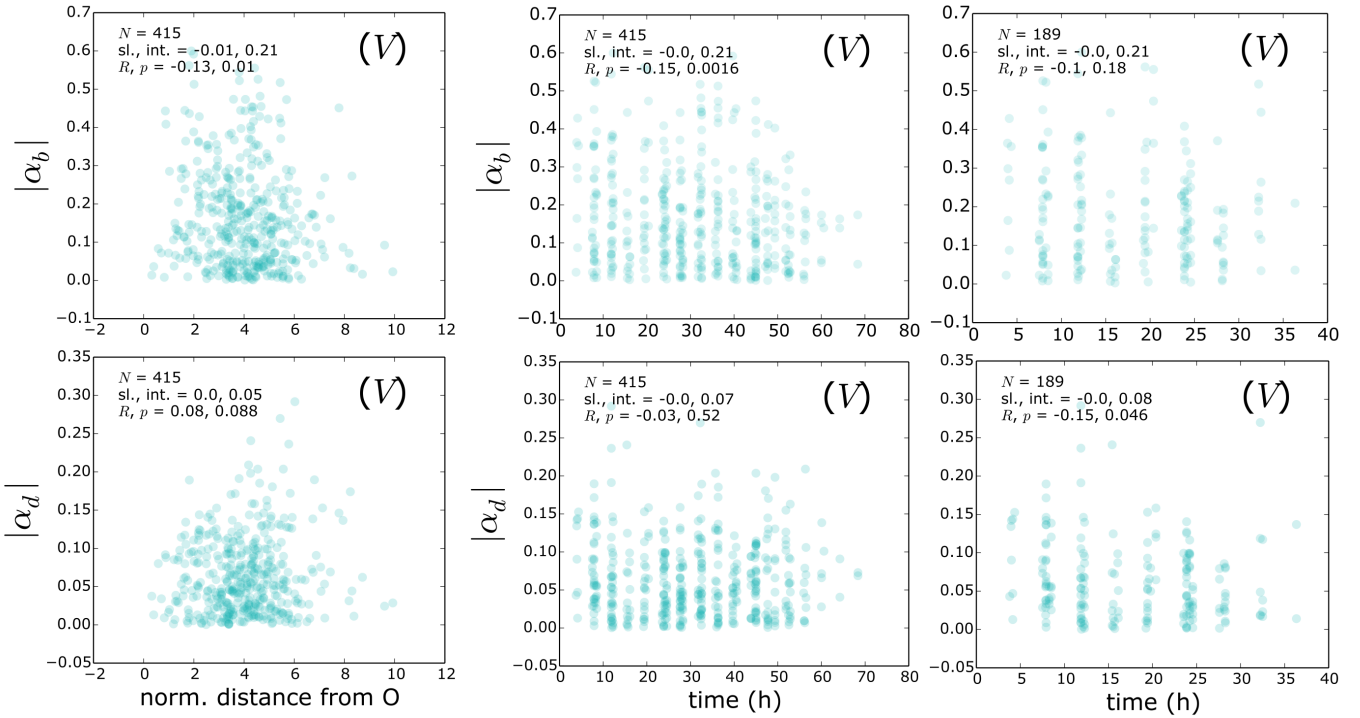


Fig. S10: Sister-volume asymmetry statistics have minimal spatiotemporal variation that does not affect results. There is no correlation between Euclidean distance from O , measured for each SAM in units of $(\text{median cell volume})^{1/3}$, and sister-volume asymmetry $(|(V-V^{\text{sis}})/(V+V^{\text{sis}})|)$. This conclusion is valid at both birth (top row, $|\alpha_b|$) and division (bottom row, $|\alpha_d|$), see also Table S2. There is a weak correlation with time at birth. However, this correlation is an artifact due to the finite duration of the experiment, and it disappeared when cells born late in the time-lapse were removed from the data set (removing cells born after $t_{\text{med}} \sim 35$ h leaves $\sim 50\%$ of data points; right column), while the correlations among these statistics, from which the mode of cell size regulation were inferred, were unaffected (Table S6). The plots show data from all pairs of sisters that completed cell cycles that began < 45 μm from O .

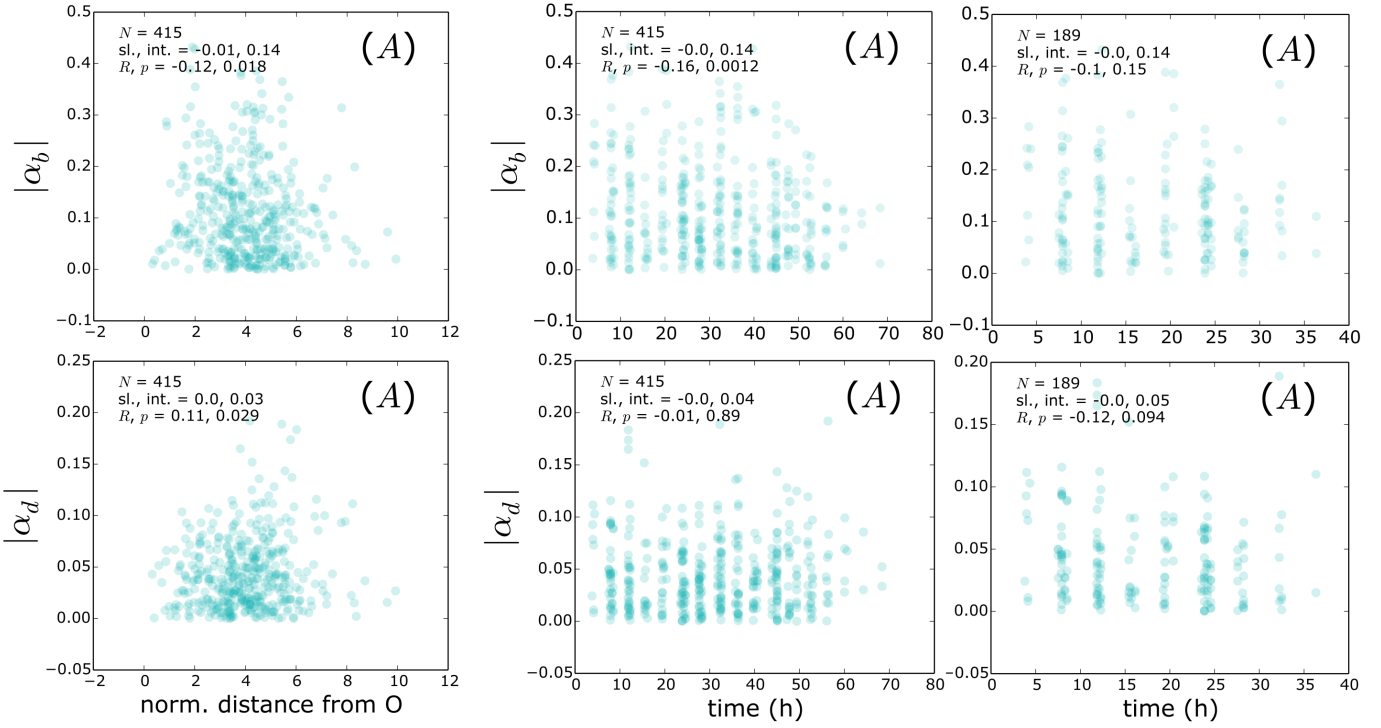


Fig. S11: Sister-wall surface area asymmetry statistics have minimal spatiotemporal variation that does not affect results. There is no correlation between Euclidean distance from O , measured for each SAM in units of $(\text{median cell volume})^{1/3}$, and the sister-total wall area asymmetry ($|(A-A^{\text{sis}})/(A+A^{\text{sis}})|$) at both birth (top row, $|\alpha_b|$) and division (bottom row, $|\alpha_d|$), see also Table S2. As in Fig. S10, the weak correlation with time at birth is an artifact due to the finite duration of the experiment; it disappeared when cells born late in the time-lapse were removed from the data set (right column), while the correlations among these statistics, from which the mode of cell size regulation were inferred, were unaffected (Table S6). The plots show data from all pairs of sisters that completed cell cycles that began $<45 \mu\text{m}$ from O .

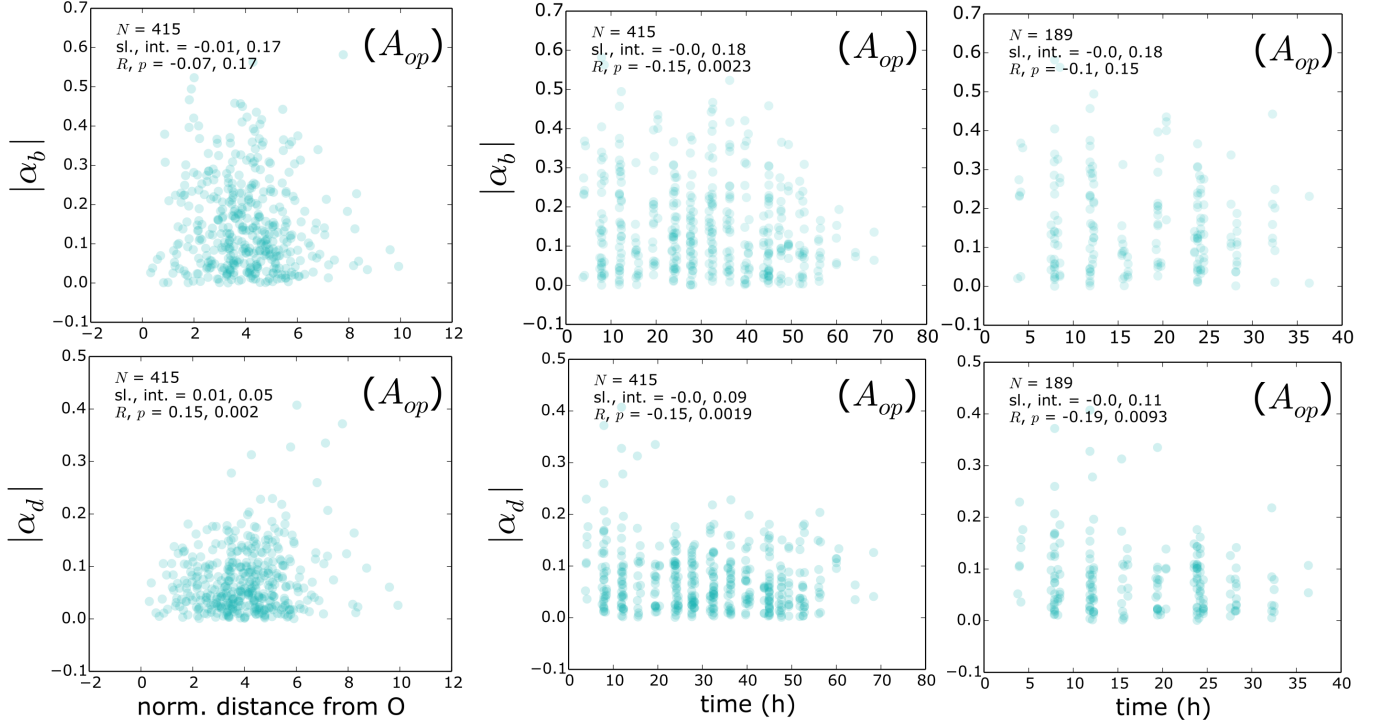


Fig. S12: Sister-outer periclinal wall area asymmetry statistics have minimal spatiotemporal variation that does not affect results. There is a weak correlation between Euclidean distance from O , measured for each SAM in units of $(\text{median cell volume})^{1/3}$, and the sister-outer periclinal wall area asymmetry statistics $(|(A_{op} - A_{op}^{\text{sis}})/(A_{op} + A_{op}^{\text{sis}})|)$. There is no correlation at birth (top row, $|\alpha_b|$), and a weak correlation at division owing to a small number of data points (bottom row, $|\alpha_d|$), see also Table S2. As in Fig. S10, the weak correlation with time at birth is an artifact due to the finite duration of the experiment; it disappeared when cells born late in the time-lapse were removed from the data set (right column), while the correlations among these statistics, from which the mode of cell size regulation were inferred, were unaffected (Table S6). The plots show data from all pairs of sisters that completed cell cycles that began $<45 \mu\text{m}$ from O .

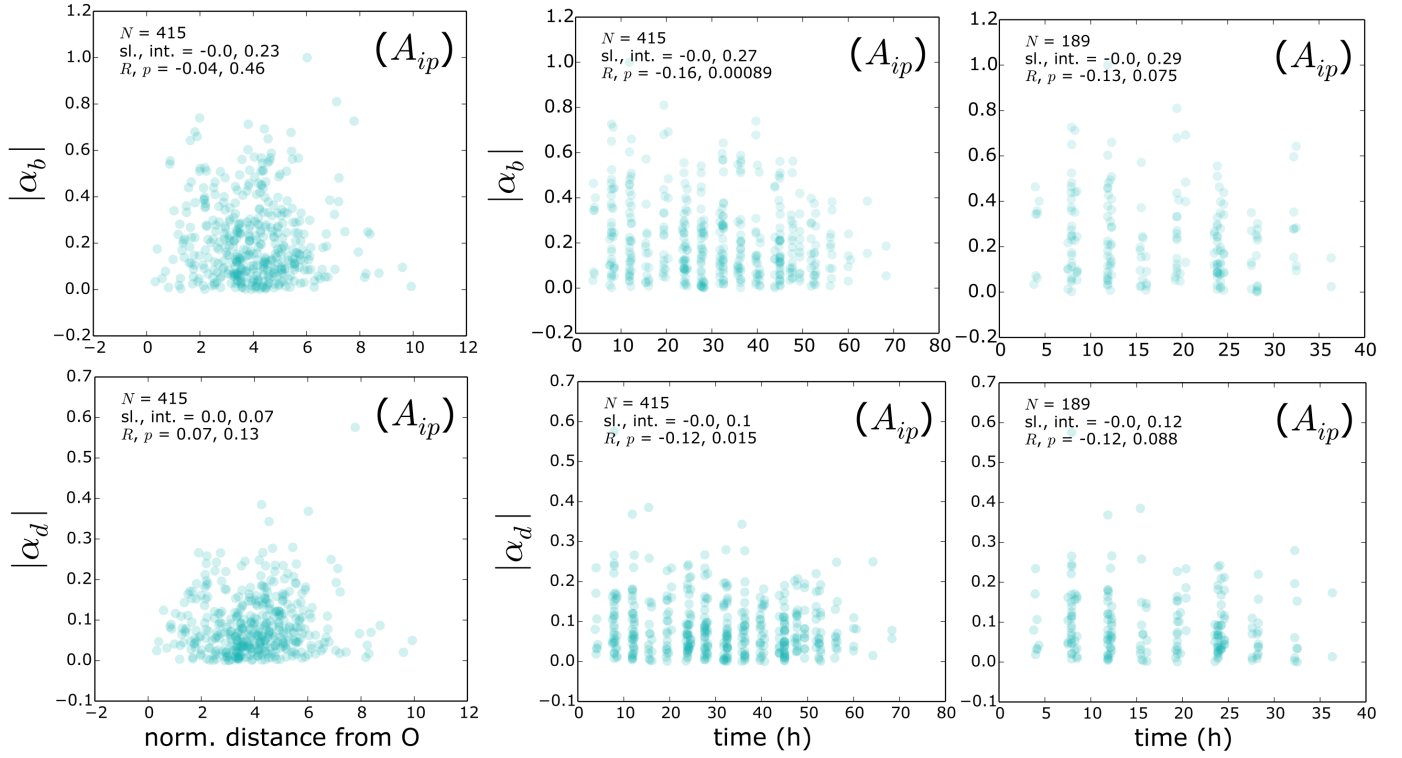


Fig. S13: Sister-inner periclinal wall area asymmetry statistics have minimal spatiotemporal variation that does not affect results. There is no correlation between Euclidean distance from O, measured for each SAM in units of $(\text{median cell volume})^{1/3}$, and the sister-inner periclinal wall area asymmetry statistics $(|(A_{ip} - A_{ip}^{\text{sis}})/(A_{ip} + A_{ip}^{\text{sis}}})|$ at both birth (top row, $|\alpha_b|$) and division (bottom row, $|\alpha_d|$), see also Table S2. As in Fig. S10, the weak correlation with time at birth is an artifact due to the finite duration of the experiment; it disappeared when cells born late in the time-lapse were removed from the data set (right column), while the correlations among these statistics, from which the mode of cell size regulation were inferred, were unaffected (Table S6). The plots show data from all pairs of sisters that completed cell cycles that began $<45 \mu\text{m}$ from O.

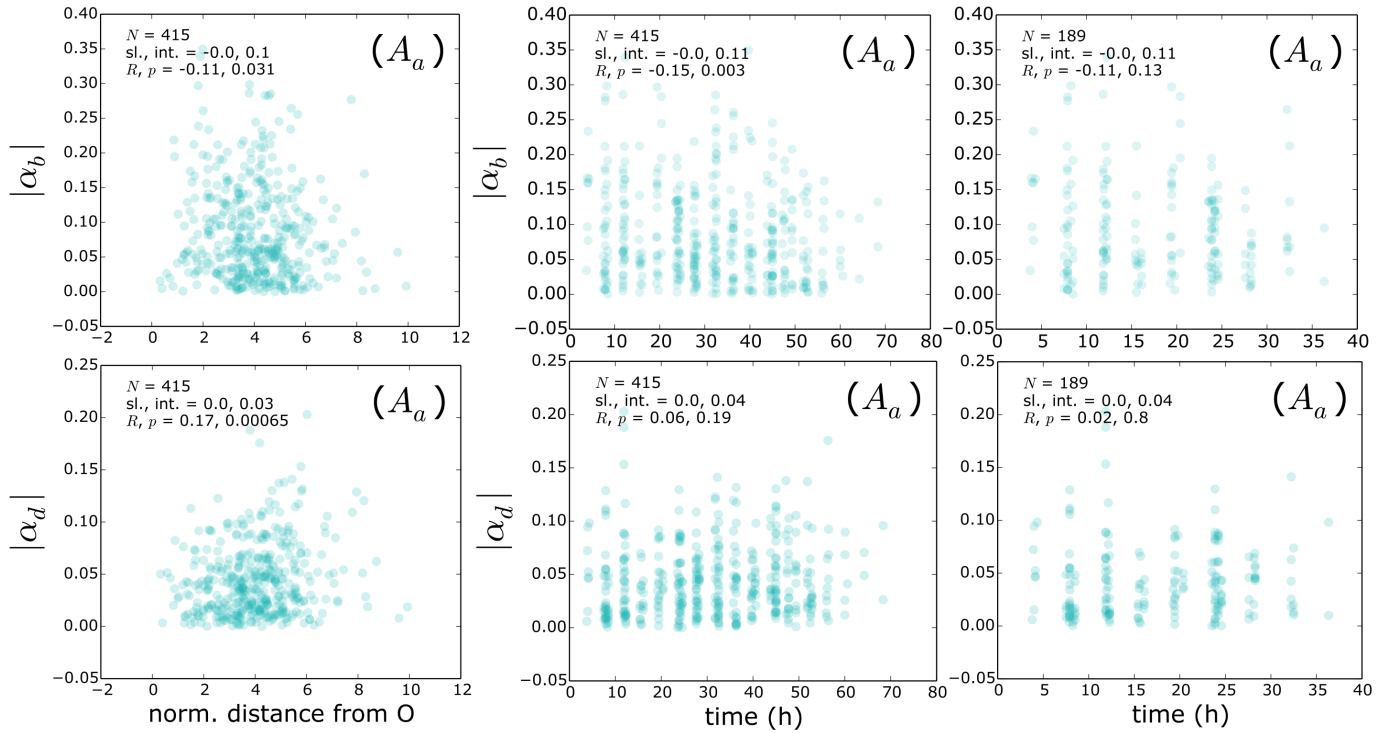


Fig. S14: Sister-anticlinal wall area asymmetry statistics have minimal spatiotemporal variation that does not affect results. There is no correlation between Euclidean distance from O , measured for each SAM in units of $(\text{median cell volume})^{1/3}$, and the sister-anticlinal wall area asymmetry statistics $(|(A_a - A_a^{\text{sis}})/(A_a + A_a^{\text{sis}}}|)$ at both birth (top row, $|\alpha_b|$) and division (bottom row, $|\alpha_d|$), see also Table 2. As in Fig. S10, the weak correlation with time at birth is an artifact due to the finite duration of the experiment; it disappeared when cells born late in the time-lapse were removed from the data set (right column), while the correlations among these statistics, from which the mode of cell size regulation were inferred, were unaffected (Table S6). The plots show data from all pairs of sisters that completed cell cycles that began $<45 \mu\text{m}$ from O .

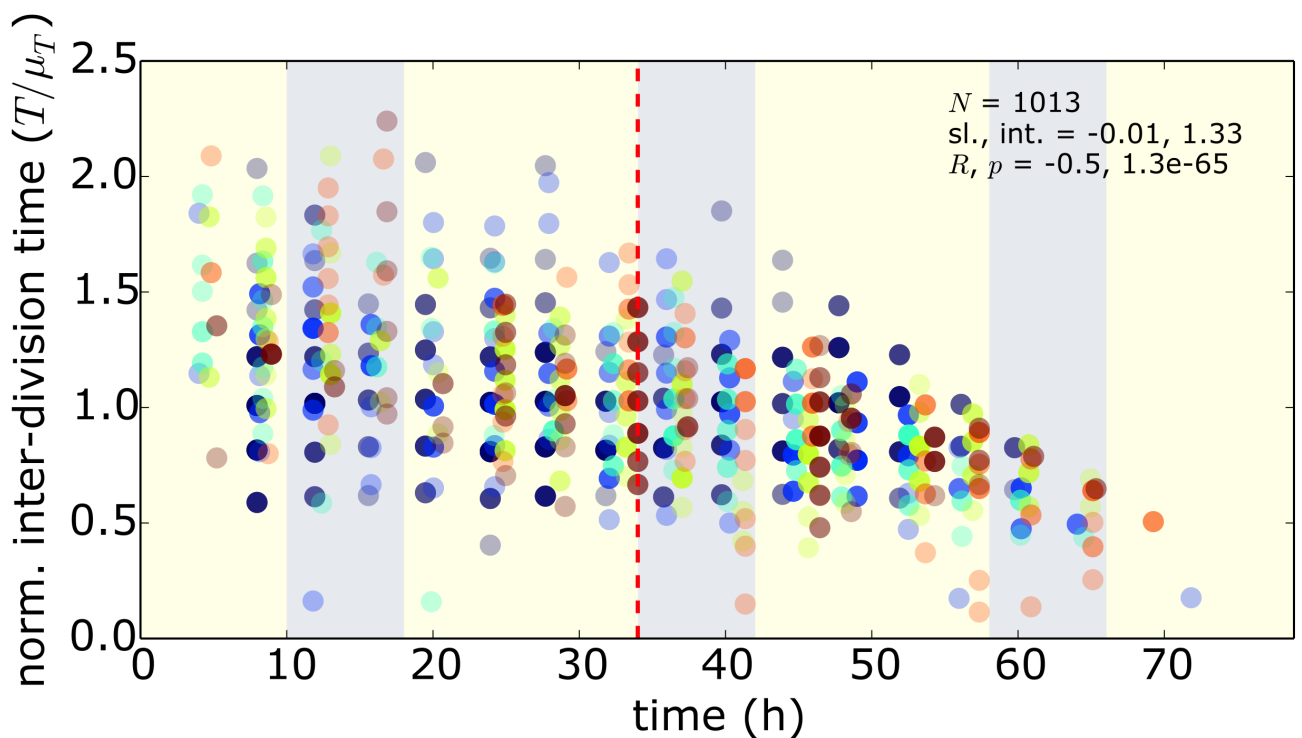


Fig. S15: The mean inter-division time of L1 central zone cells decreases over the time-lapse from ~35 h onward (red dashed line). This decrease occurred because within ~1 cell cycle of the end of the time-lapse, cells with rapid cell cycles are more likely to be sampled. This bias did not affect any of our conclusions (Table S6). Data points are colored according to SAMs.

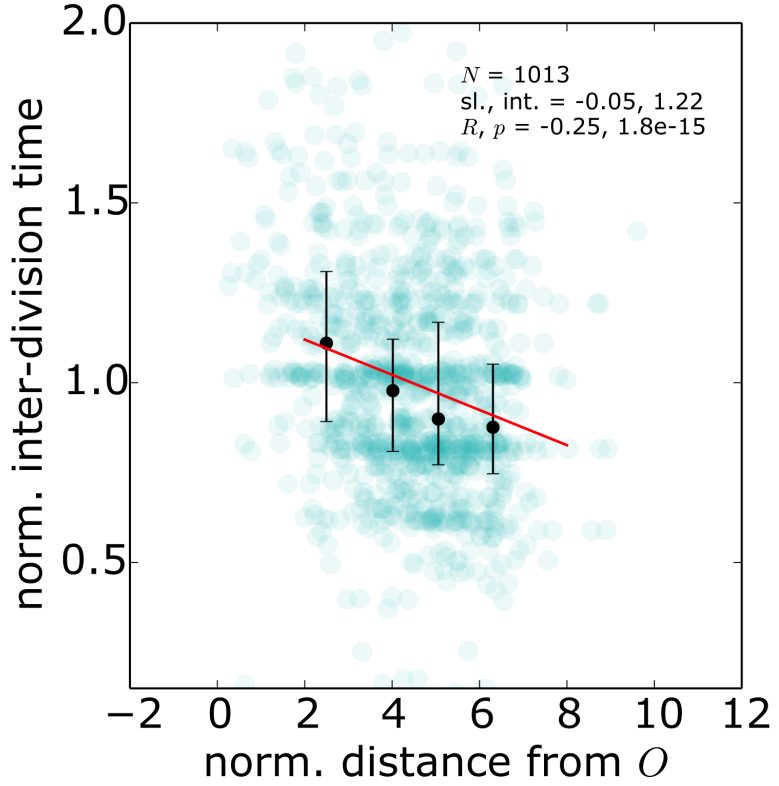


Fig. S16: Quantitative relation between cell growth rate and distance from the SAM center. The inter-division times among L1 central zone cells decrease with distance from the center of the SAM at O , normalized by $(\text{median cell volume})^{1/3}$, at a rate of $\sim 5\%$ between neighboring cells. The red line is the least-square linear fit and the error bars show medians of inter-division times when binned according to normalized distance.

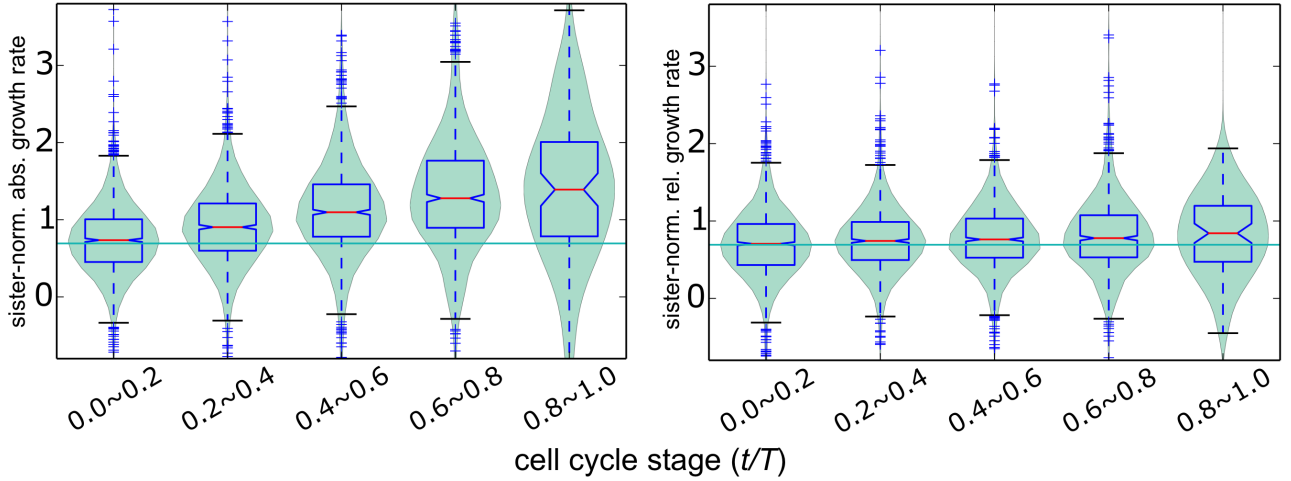


Fig. S17: Cell volume grows proportionally to volume. The volumetric absolute growth rate normalized by the average inter-division time of a cell and its sister (T^{sis}) increases by ~ 2 -fold over the cell cycle (absolute growth rate = $dV/dt \times T^{\text{sis}}/\mu_b$), while the volumetric relative growth rate normalized by the average inter-division time of a cell and its sister (T^{sis}) remains constant (relative growth rate = $dV/dt \times T^{\text{sis}}/V$) throughout the cell cycle (as a function of t/T , where $t = 0$ is the time of cell birth and T is the inter-division time) at the expected value of $\ln(2)$ (green horizontal line) for normalized volume V/μ_V^t . The purpose of normalizing by T^{sis} was to partially eliminate the effect of the spatiotemporal variation in growth rates on these statistics: the statistic provides a local measure of cell doubling time, since sister cells, which are often generated by asymmetric divisions, are born in the same position and at the same time. In sum, the plots demonstrate that cell volume grows proportionally to volume.

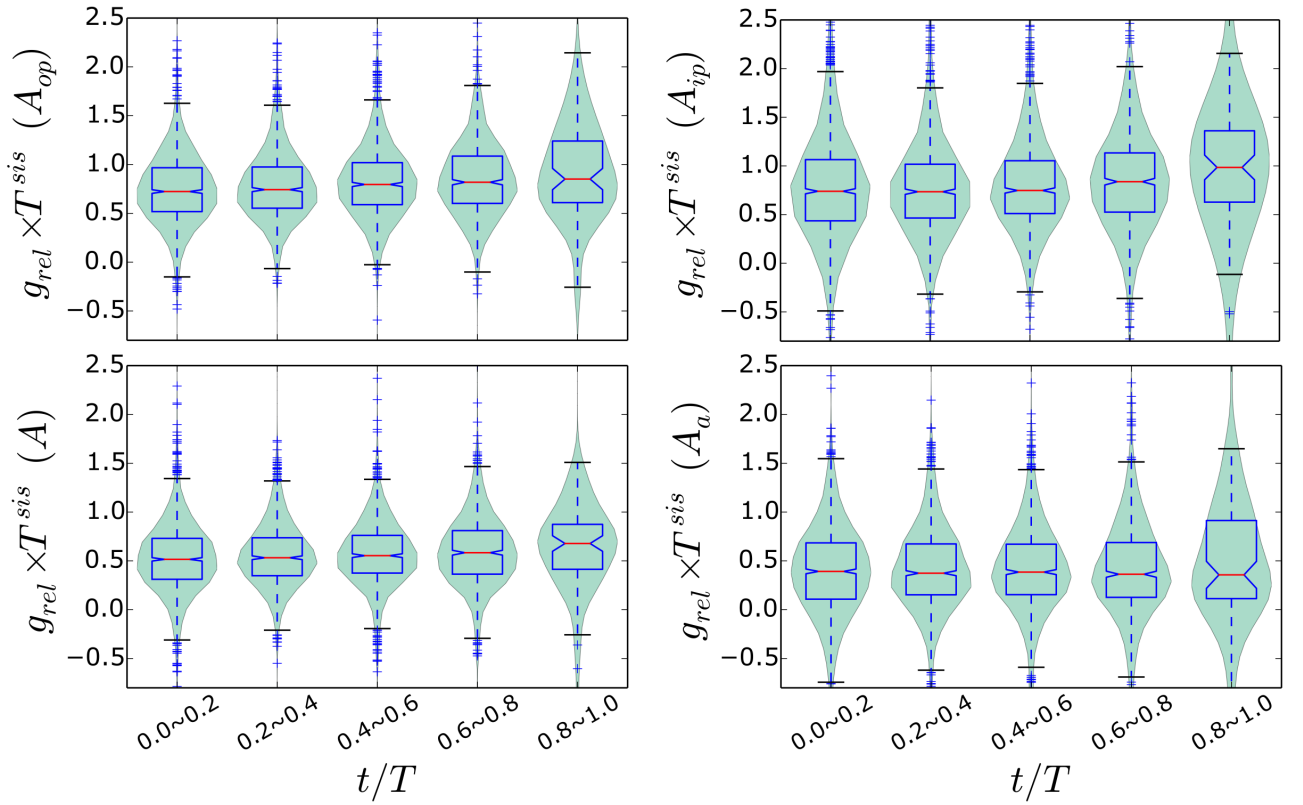


Fig. S18: Cell size grows at a constant relative rate for different wall area cell size metrics. The constant relative volumetric growth rate over the cell cycle and the power-law relationships between cell volume and wall surface area measurements (total surface area $A \sim V^{2/3}$, outer periclinal wall surface area $A_{op} \sim V^{0.8}$, inner periclinal wall surface $A_{ip} \sim V$, and anticlinal wall area $A_a \sim V^{0.5}$) predict that each measure of wall surface area S also grows at a constant relative rate over the cell cycle: $g_{rel} = dS/dt \times 1/S = \text{constant}$. The plots show that the sister-normalized relative growth rates $g_{rel} \times T^{sis}$ (where T^{sis} , the average inter-division time of the cell and its sister, partially factors out the increase in growth rates with radial distance from the SAM's center at O) are approximately constant over the cell cycle (as a function of t/T , where $t = 0$ is the time of cell birth and T is the inter-division time) for each wall surface area measurement as predicted.

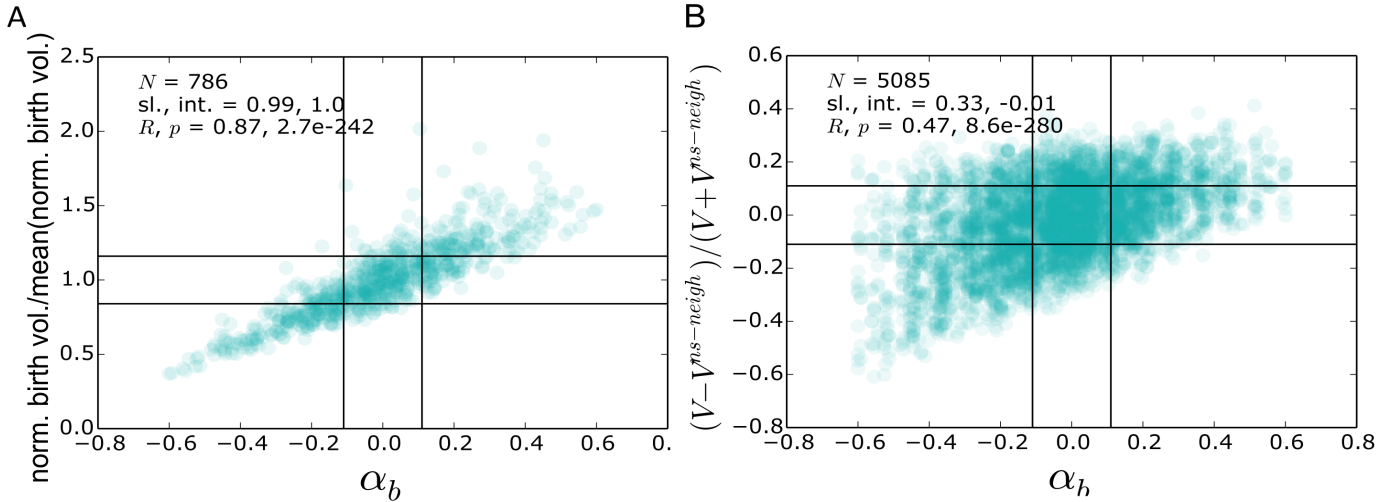


Fig. S19: Asymmetric division is correlated with cell-size and the size of a cell compared with its non-sister neighbors. There is a strong correlation between the degree of asymmetric division, measured by $\alpha_b = (V_b - V_b^{\text{sis}})/(V_b + V_b^{\text{sis}})$, and (A) normalized birth volume $(V_b/\mu_V^t)/\text{mean}(V_b/\mu_V^t)$ ($R = 0.87, p = 10^{-242}$), and (B) the relative volume of a cell compared with its *non-sister* neighbors, quantified by $(V - V^{\text{ns-neigh}})/(V + V^{\text{ns-neigh}})$, where V is the cell's volume and $V^{\text{ns-neigh}}$ is the average volume of its non-sister neighbors ($R = 0.47, p = 10^{-280}$). The plots show data from all pairs of sisters that completed cell cycles that began $<30 \mu\text{m}$ from O. Vertical lines correspond to $\alpha_b = -0.11$ and $\alpha_b = 0.11$; cells that have $|\alpha_b| \leq 0.11$ or $|\alpha_b| > 0.11$ were considered to have been born from a symmetric or asymmetric division of the mother cell, respectively; using this definition, the data were split ~50:50 according to whether cells were born of a symmetric or asymmetric division. Similarly, the horizontal lines in (A) split the data ~50:50 according to whether cells were born with intermediate volumes, $|V_b/\mu_V^t/\text{mean}(V_b/\mu_V^t) - 1| \leq 0.16$, or small/large volumes, $|V_b/\mu_V^t/\text{mean}(V_b/\mu_V^t) - 1| > 0.16$; the horizontal lines in (B) split the data ~50:50 according to whether cells of volume V have similarly sized non-sister neighboring cells on average $|(V - V^{\text{ns-neigh}})/(V + V^{\text{ns-neigh}})| \leq 0.11$, or differently sized non-sister neighboring cells $|(V - V^{\text{ns-neigh}})/(V + V^{\text{ns-neigh}})| > 0.11$.

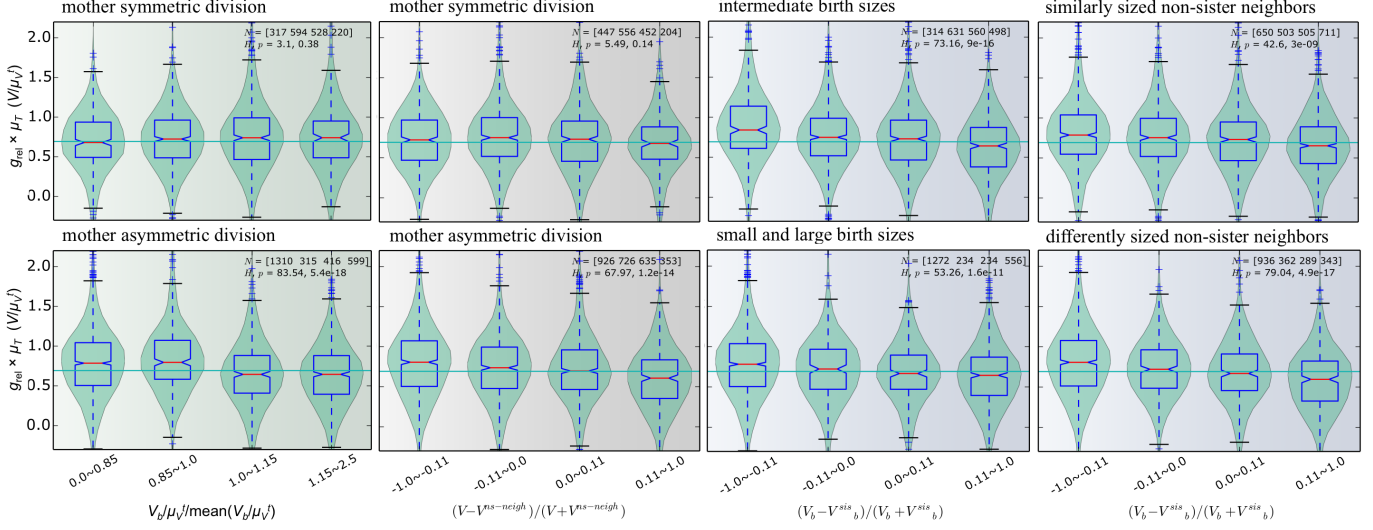


Fig. S20: Different relative growth rates between sisters result from asymmetric divisions of the mother cell. Cells generated by a symmetric division ($|a_b| \leq 0.11$) grow at the same relative rate regardless of their birth volume (top row, left panel; Kruskal-Wallis $H = 3.1, p = 0.38$) or the relative size of their non-sister neighbors (top row, middle-left panel; Kruskal-Wallis $H = 5.5, p = 0.14$), while cells generated by asymmetric divisions have relative growth rates that depend on both birth volume and the relative size of their non-sister neighbors (bottom row, left and middle-left panel; Kruskal-Wallis $p < 10^{-13}$). The dependence of relative growth rate on mother-cell division asymmetry persists for cells born with intermediate volumes ($|V_b / \mu_V^t / \text{mean}(V_b / \mu_V^t) - 1| \leq 0.16$, top row, middle-right; Kruskal-Wallis $H = 73, p = 10^{-15}$) and for cells with non-sister neighbors of similar volumes ($|(V - V^{ns-neigh}) / (V + V^{ns-neigh})| \leq 0.11$, top row, right; Kruskal-Wallis $H = 43, p = 10^{-9}$). The dependence also persists for cells born with excessively small or large volumes ($|V_b / \mu_V^t / \text{mean}(V_b / \mu_V^t) - 1| > 0.16$, bottom row, middle-right; Kruskal-Wallis $H = 53, p = 10^{-11}$) and cells with non-sister neighbors of significantly different relative sizes ($|(V - V^{ns-neigh}) / (V + V^{ns-neigh})| > 0.11$, bottom row, right; Kruskal-Wallis $H = 79, p = 10^{-16}$). The data points included/excluded from each plot are presented in Fig. S19. In the upper right corner of each panel, the sample size N is

given for each violin, with left → right values corresponding to left → right violins. Together, these results indicate that differently sized sisters grow at different rates owing primarily to the asymmetric division of the mother cell, rather than to their being smaller/larger or their increased likelihood of neighboring comparatively smaller/larger cells.

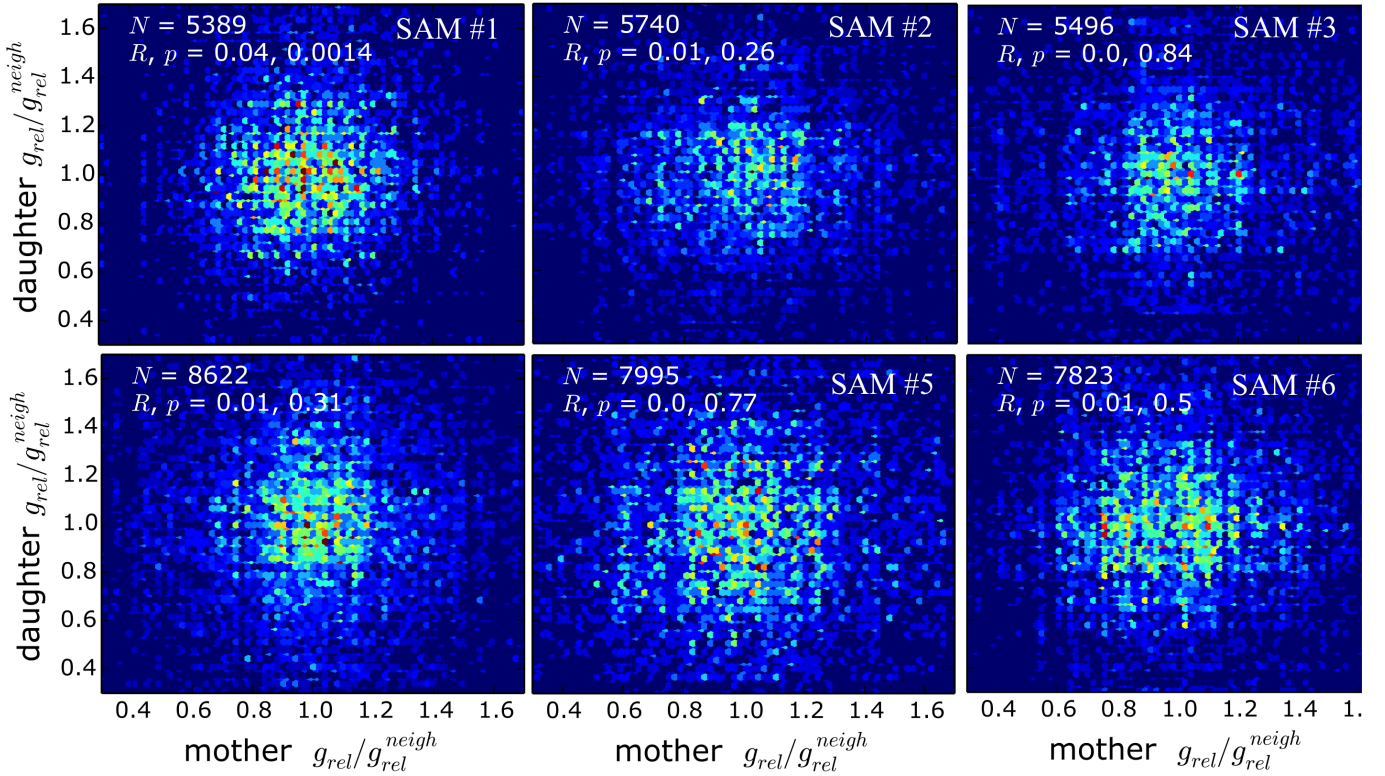


Fig. S21: Daughter relative growth rates are uncorrelated with mother relative growth rates. For the L1 central zone cells of each SAM, the volumetric relative growth rates of mother cells are not correlated with the volumetric relative growth rates of their progeny. Each cellular volumetric relative growth rate $g_{rel} = (V(t+\Delta t) - V(t))/\Delta t \times 2/(V(t+\Delta t) + V(t))$ was normalized by the mean relative growth rate of the neighboring cells, g_{rel}^{neigh} , to eliminate the correlation that would otherwise result purely as a consequence of the mother and daughter cells being located the same radial distance from O. In the heat map of each panel, red corresponds to high frequency and blue corresponds to low frequency.

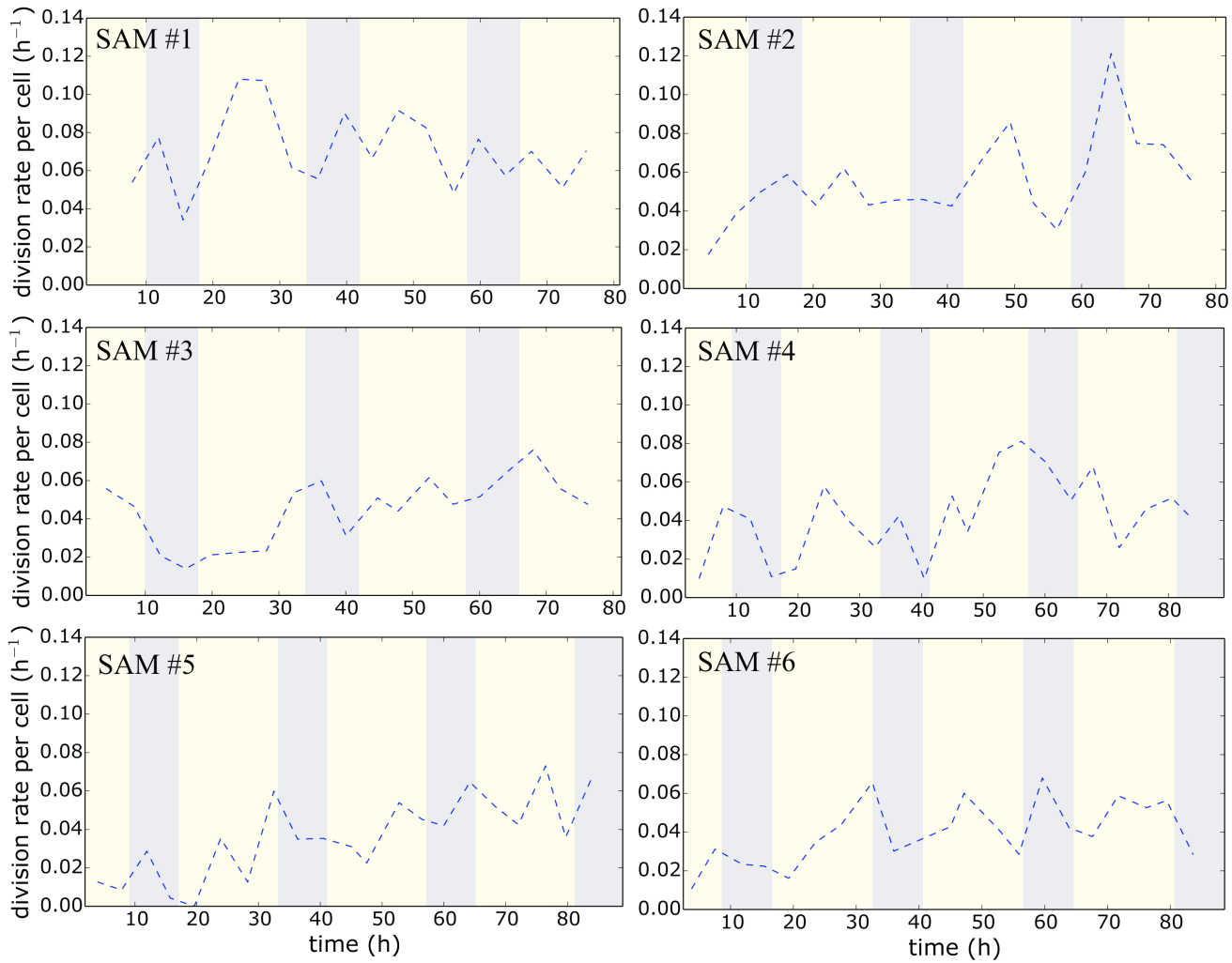


Fig. S22: There is no consistent discernible effect of light/dark cycles on the division rate. In each SAM, the division rate per cell varies over time throughout the time-lapse among the ~100 cells <30 μm from O, but there is no consistent discernible effect of light/dark cycles on the division rate (light/dark cycles shown by yellow/blue regions respectively). The higher division rate in SAM #1 may have been due to a small wound at the edge of the peripheral zone.

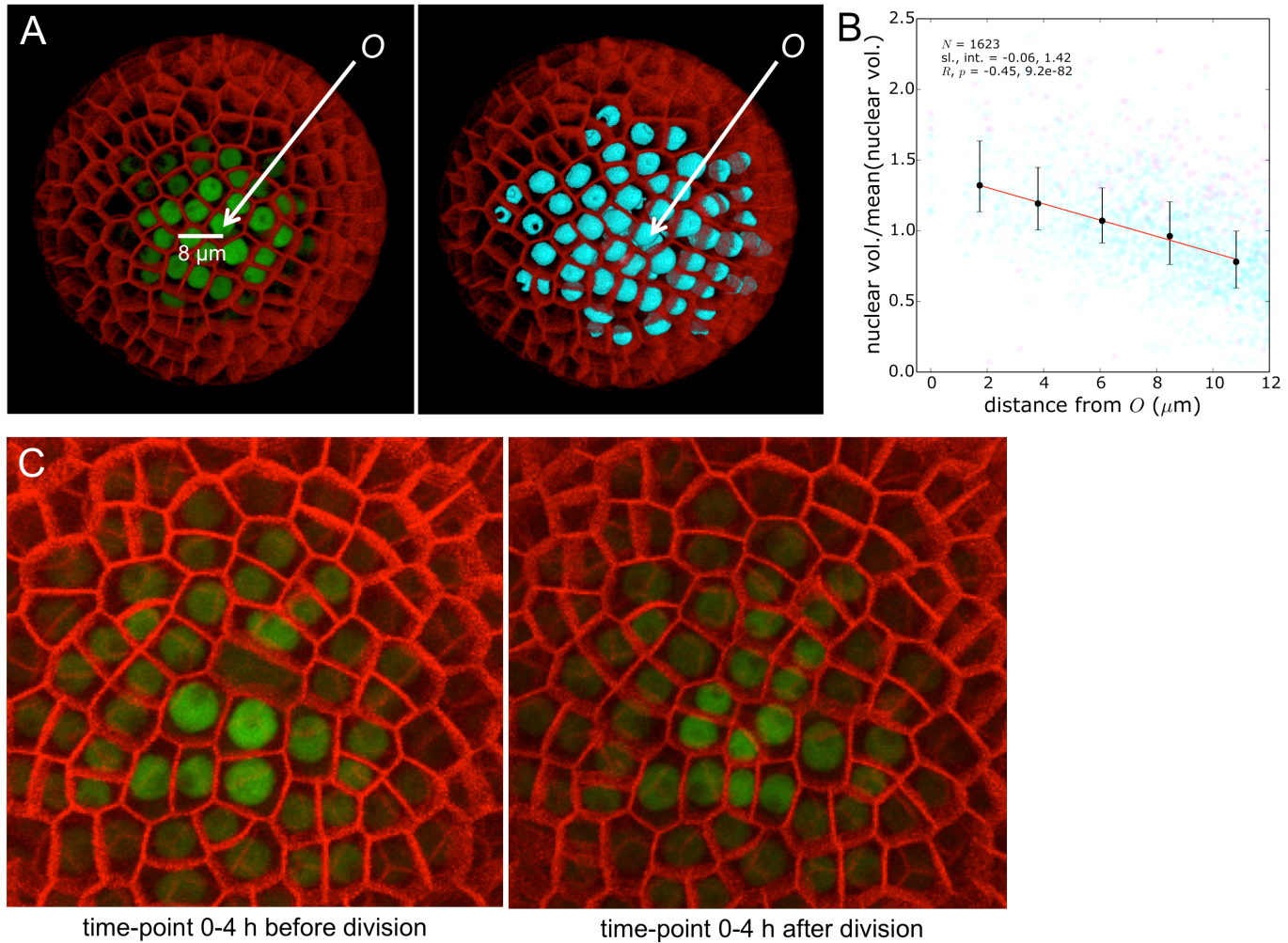


Fig. S23: Nuclear volume segmentations and quantification. (A-B) The nuclear-localized pCLV3::dsRED-N7 reporter permitted 6-9 nuclei, within a 3D Euclidean distance of 8 μm from the center of the SAM at O, to be accurately segmented (Materials and Methods). (A) The CLAVATA3 (green) and membrane (red) reporters (left), and the corresponding nuclear segmentation (right). (B) The reduction in nuclear volume with distance from O is an artifact due to the effect of the decreasing CLAVATA3 signal on the segmentations. Pink data points correspond to nuclei of cells that divide within the following ~0-4 h period. (C) The nuclear-localized CLAVATA3 reporter was used to manually count the number of cell divisions in which the corresponding nuclei were diffuse in the preceding ~0-4 h; from this, the duration of mitosis

was estimated to be \approx 40 min (Table S4). The panels show one example of a diffuse nucleus \sim 0-4 h prior to division. Segmentations of nuclei that are undergoing mitosis lead to computation of a nuclear volume that is close to zero (e.g. several pink data points in (B)).

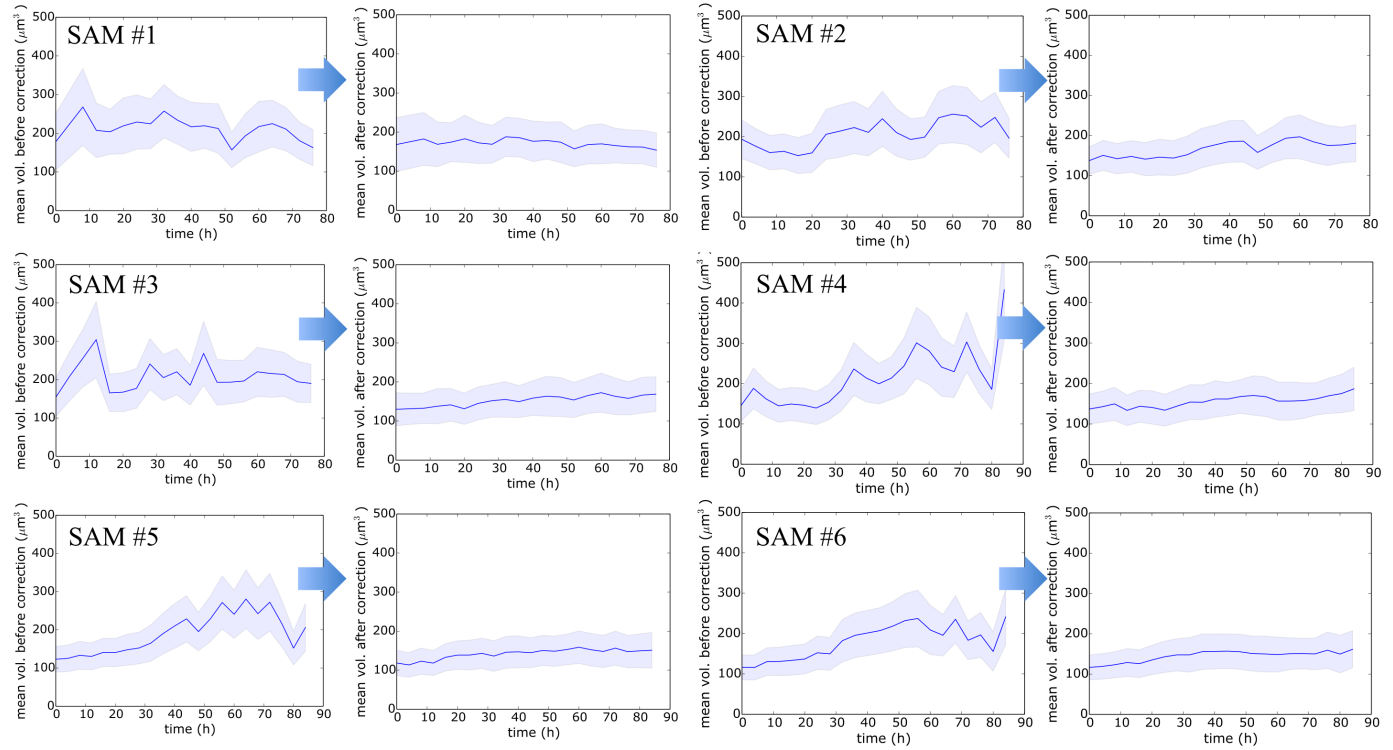


Fig. S24: The bias and noise in measurements of cell-size metrics from 3D segmentations of confocal z-stacks was strongly reduced by our method for correcting the artificial stretching of cells in the z-direction due to stem growth/SAM movement during time-lapse imaging (Materials and Methods). Compare the change in mean cell volume during the time-lapse before versus after the correction (left vs. right graphs for each SAM; blue lines enclosed by shaded regions represent mean volumes \pm one standard deviation).

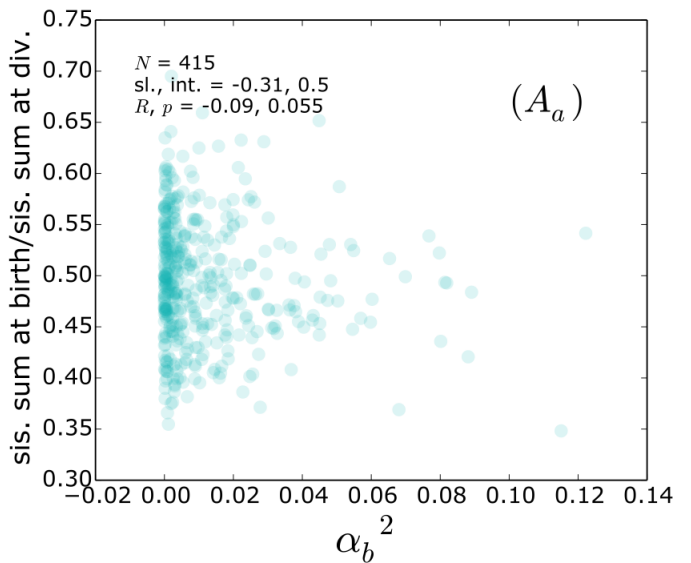
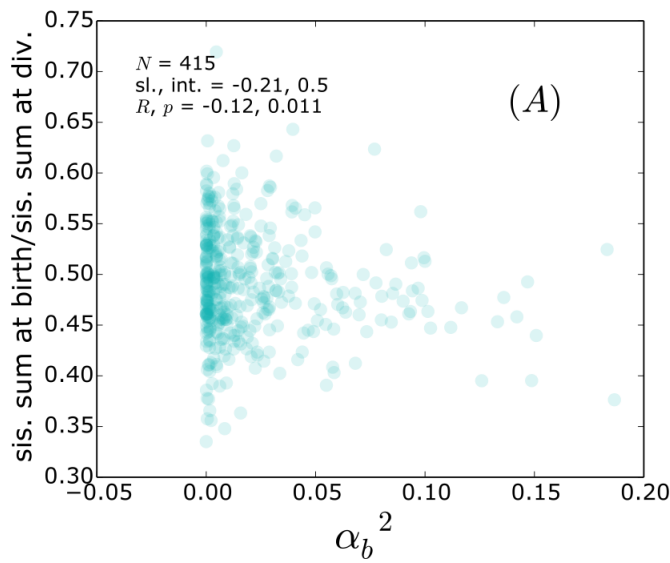
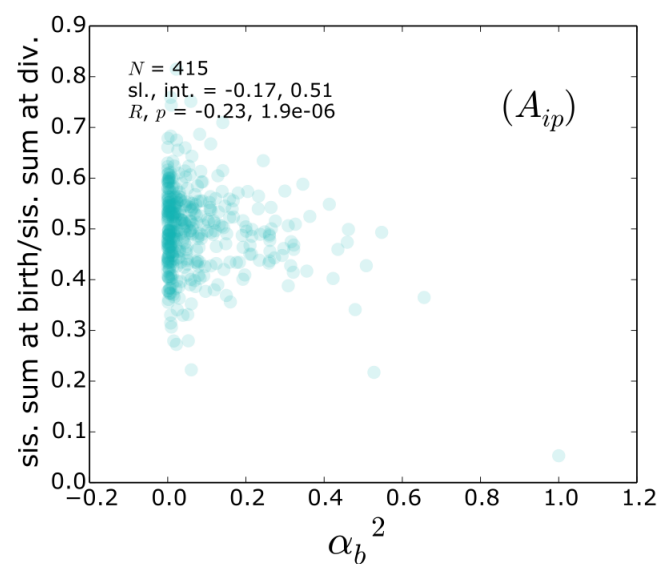
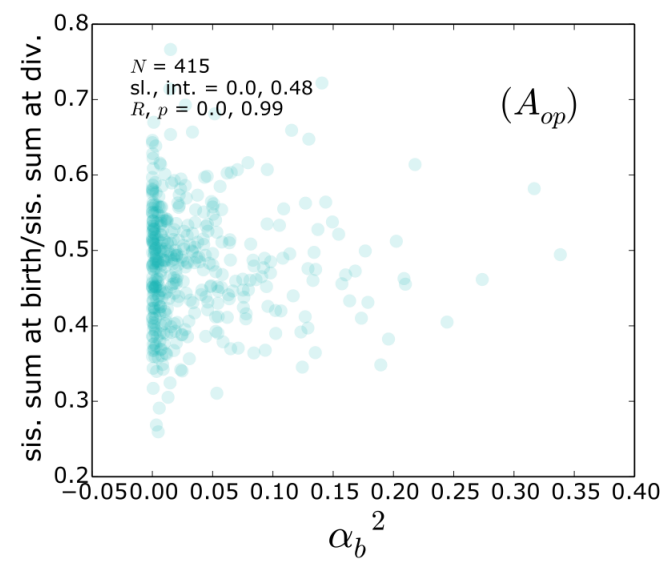
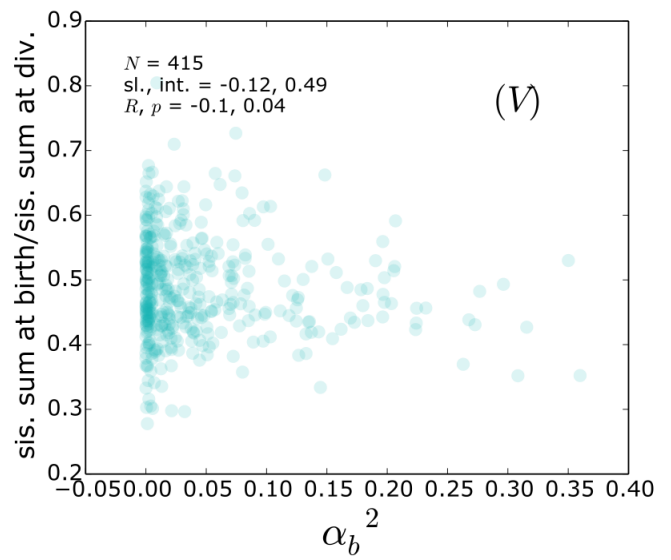
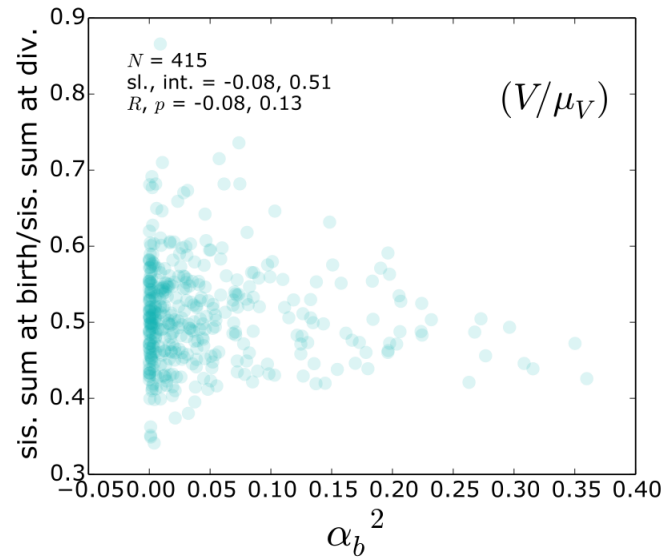


Fig. S25: The degree of asymmetric division, quantified by α_b^2 , is uncorrelated with the ratio of the sum of sister-size metrics at birth versus division, $(S_b + S_b^{\text{sis}})/(S_d + S_d^{\text{sis}})$, for cell-size metrics normalized volume V/μ_V^t (upper left), volume V (upper right), outer periclinal wall area A_{op} (middle left), total wall area A (bottom left), and anticlinal wall area A_a (bottom right). The correlation between α_b^2 and inner periclinal wall area A_{ip} (middle right) is significant; however, examination of the corresponding plot suggests that this correlation is due to a single outlier.

Supplementary Tables:

Table S1: Cell-size distributions and cell-cycle statistics for SAMs #1-6. In all SAMs, the coefficient of variation of cell volumes (σ_V) is similar (~0.3), while the mean cell volume (μ_V) varies by 1.2-fold from $141 \text{ } \mu\text{m}^3$ to $171 \text{ } \mu\text{m}^3$ and the mean outer periclinal surface area ($\mu_{A_{op}}$) of $35 \text{ } \mu\text{m}^2$. The mean inter-division time (μ_T) varies from 21 h to 31 h. Among all SAMs, the mean cell volume is 1.3-1.4x the mean cell birth volume. The coefficients of variation in volume at birth (σ_b), volume at division (σ_d), and asymmetric cell division (σ_a = standard deviation of $(V_b - V_b^{\text{sis}})/2(V_b + V_b^{\text{sis}})$) were highly consistent among the SAMs. Histograms of the number of neighbors in the L1 layer (N_{neigh}) were positively skewed, with a peak at $N_{\text{neigh}} = 6$ (Fig. S1). The time-averaged distribution of outer periclinal wall area was significantly non-normal with a positive skewness (Fig. S2). Slopes and intercepts from least-square linear fits of number of neighbors (N_{neigh}) vs. outer periclinal wall area (A_{op}) were consistent with Lewis's Law (32, 33).

	μ_V (μm^3)	$\mu_{A_{op}}$ (μm^2)	σ_V	V skew., p	μ_T (h)	μ_V/μ_b	σ_b	σ_d	σ_a	N_{neigh} vs. A_{op} slope, int.
#1	171	34	0.31	$0.76, 10^{-34}$	21	1.3	0.26	0.17	0.11	0.19, -0.16
#2	165	35	0.30	$0.33, 10^{-9}$	25	1.4	0.29	0.13	0.11	0.18, -0.10
#3	153	35	0.30	$0.26, 10^{-5}$	27	1.3	0.28	0.11	0.11	0.20, -0.22
#4	156	35	0.29	$0.26, 10^{-6}$	29	1.3	0.25	0.12	0.11	0.18, -0.11
#5	141	33	0.29	$0.21, 10^{-5}$	31	1.3	0.28	0.11	0.12	0.18, -0.19
#6	144	36	0.29	$0.27, 10^{-6}$	31	1.3	0.25	0.14	0.10	0.19, -0.12
Median	155	35	0.30	0.27	28	1.3	0.27	0.13	0.11	0.19, -0.14

Table S2: The degree of asymmetry between sister cells $|\alpha_b| = |(S_b - S^{sis}_b)/(S_b + S^{sis}_b)|$ for different cell-size metrics does not depend on Euclidean 3D distance from O , where distance is measured in units of $(\text{mean cell volume})^{1/3}$. This lack of dependence is evident based on the slopes of least-square linear fits (sl.) to distance vs. $|\alpha_b|$ being close to zero and the corresponding absent or weak correlations; see also Fig. S10-S14. Similar relationships hold for $|\alpha_d| = |(S_d - S^{sis}_d)/(S_d + S^{sis}_d)|$. There was a weak dependence of $|\alpha_b|$ on time from the start of data acquisition; however, this correlation disappeared when 50% of data points, corresponding to cells born late in the time-lapse ($t > t_{med}$), are removed. Removing these data did not impact other statistics and therefore any of our conclusions (Table S6). Moreover, $|\alpha_T| = |(T - T^{sis})/(T + T^{sis})|$, where T is a cell's inter-division time and T^{sis} is the corresponding sister cell's inter-division time, did not depend on distance or time: for distance vs. $|\alpha_T|$, $R = 0.04$ and $p = 0.39$; for time vs. $|\alpha_T|$, $R = -0.1$ and $p = 0.04$. Our analysis includes all pairs of L1 sisters with complete cell cycles that began $<45 \mu\text{m}$ from O ($N = 415$).

var.	distance vs. $ \alpha_b $		distance vs. $ \alpha_d $					
	sl., int.	R, p	sl., int.	R, p				
V/μ_V^t	-0.01, 0.21	0.13, 0.01	0.00, 0.05	0.08, 0.09				
V	-0.01, 0.21	-0.13, 0.01	0.00, 0.05	0.08, 0.09				
A	-0.01, 0.14	-0.12, 0.02	0.00, 0.03	0.11, 0.03				
A_{op}	-0.01, 0.17	-0.07, 0.2	0.01, 0.05	0.15, 0.002				
A_{ip}	0.00, 0.23	-0.04, 0.5	0.00, 0.07	0.07, 0.1				
A_a	0.00, 0.10	-0.11, 0.03	0.00, 0.03	0.17, 0.0007				
	time vs. $ \alpha_b $		time vs. $ \alpha_d $		time $< t_{\text{med}}$ vs. $ \alpha_b $		time $< t_{\text{med}}$ vs. $ \alpha_d $	
	sl., int.	R, p	sl., int.	R, p	sl., int.	R, p	sl., int.	R, p
V/μ_V^t	0.00, 0.21	-0.15, 0.002	0.00, 0.07	-0.03, 0.5	0.0, 0.21	-0.1, 0.2	0.0, 0.08	-0.15, 0.05
V	0.0, 0.21	-0.15, 0.002	0.00, 0.07	-0.03, 0.5	0.0, 0.21	-0.1, 0.2	0.0, 0.08	-0.15, 0.05
A	0.0, 0.14	-0.16, 0.001	0.00, 0.04	-0.01, 0.9	0.0, 0.14	-0.1, 0.15	0.0, 0.05	-0.12, 0.09
A_{op}	0.00, 0.18	-0.15, 0.002	0.00, 0.09	-0.15, 0.002	0.0, 0.18	-0.1, 0.15	0.0, 0.11	-0.19, 0.01
A_{ip}	0.00, 0.27	-0.16, 0.0009	0.00, 0.1	-0.12, 0.02	0.0, 0.29	-0.13, 0.08	0.0, 0.12	-0.12, 0.09
A_a	0.00, 0.11	-0.15, 0.003	0.00, 0.04	0.06, 0.2	0.0, 0.11	-0.11, 0.13	0.0, 0.04	0.02, 0.8

Table S3: Cell size statistics among L1 central zone cells tracked over ~3 generations indicate that neither division nor the G2/M transition are triggered when the cell reaches a critical volume or adds a critical volume increment ($N = 1013$ cells). Normalized birth volume (V_b/μ_V^t) was positively correlated with normalized division volume (V_d/μ_V^t) and negatively correlated with normalized volume increment (Δ/μ_V^t). The results were similar for non-normalized birth and division volumes (V_b/μ_b and V_d/μ_b , where μ_b is the mean birth volume among all cells tracked through a complete cell cycle in each SAM). The slopes (sl.) and intercepts (int.) from least-square linear fits between variables are given, along with Pearson R correlation coefficients and corresponding p-values. The parameter f that characterizes the size regulation rule is estimated by the slopes of normalized birth size vs. normalized division size (see also Table S5). Outliers beyond 2.5 standard deviations (~3% of data) were removed for SAMs #1-6 but not for pooled data; removing these outliers does not significantly affect the correlations.

SAM	N	V_b/μ_V^t vs V_d/μ_V^t		V_b/μ_V^t vs Δ/μ_V^t	
		sl., int.	R, p	sl., int.	R, p
#1	296	0.48, 1.2	$0.47, 10^{-17}$	-0.52, 1.2	$-0.50, 10^{-20}$
#2	183	0.36, 1.3	$0.37, 10^{-7}$	-0.64, 1.3	$-0.58, 10^{-17}$
#3	113	0.45, 1.2	$0.53, 10^{-9}$	-0.55, 1.2	$-0.61, 10^{-12}$
#4	154	0.57, 1.0	$0.59, 10^{-15}$	-0.43, 1.0	$-0.48, 10^{-10}$
#5	100	0.35, 1.2	$0.44, 10^{-5}$	-0.65, 1.2	$-0.67, 10^{-14}$
#6	122	0.50, 1.1	$0.49, 10^{-8}$	-0.50, 1.1	$-0.50, 10^{-9}$
pooled data	1013	0.48, 1.2	$0.47, 10^{-56}$	-0.52, 1.2	$-0.50, 10^{-64}$
	N	V_b/μ_b vs V_d/μ_b		V_b/μ_b vs Δ/μ_b	
		sl., int.	R, p	sl., int.	R, p
#1	296	0.48, 1.4	$0.46, 10^{-16}$	-0.52, 1.4	$-0.49, 10^{-19}$
#2	183	0.37, 1.9	$0.40, 10^{-8}$	-0.63, 1.85	$-0.60, 10^{-18}$
#3	113	0.43, 1.7	$0.50, 10^{-8}$	-0.57, 1.7	$-0.61, 10^{-13}$
#4	154	0.53, 1.5	$0.54, 10^{-12}$	-0.47, 1.5	$-0.50, 10^{-10}$
#5	100	0.32, 1.6	$0.41, 10^{-5}$	-0.68, 1.6	$-0.69, 10^{-15}$
#6	122	0.41, 1.6	$0.50, 10^{-6}$	-0.59, 1.6	$-0.55, 10^{-10}$
pooled data	1013	0.45, 1.5	$0.40, 10^{-41}$	-0.55, 1.5	$-0.48, 10^{-58}$

Table S4: Mitosis and subsequent formation of the new membrane/cell wall took place over \approx 40 min. The nuclear-localized pCLV3::dsRED-N7 signal enabled clear visualization of cell nuclei within 10 μ m of the SAM's center at O. Within this region, we manually counted the number of cell divisions for which the nuclei appeared diffuse (Fig. S23C), and therefore were undergoing mitosis, in the confocal z-stack acquired between 0 and \sim 4 h prior to each division. Using this data, we estimated the duration of M-phase as (number of divisions with diffuse nuclei)/(total number of divisions) \times 4 h = 13/80 \times 4 h = 0.65 h \approx 40 min. pCLV3::dsRED-N7 was not expressed in SAM #1.

SAM	total num. divisions <10 μ m from O	num. divisions with diffuse nuclei <10 μ m from O
#2	16	2
#3	16	2
#4	17	4
#5	18	1
#6	13	4
Total	80	13

Table S5: Cell-cycle statistics of L1 sister cells indicate that there is neither a critical size nor a critical increment checkpoint that triggers division or G2/M. Asymmetry between sister-cell sizes ($N = 415$ sister pairs) at birth, $\alpha_b = (S_b - S_b^{\text{sis}})/(S_b + S_b^{\text{sis}})$ for e.g. $S = V$ corresponding to volume, correlates strongly with division asymmetry, $\alpha_d = (S_d - S_d^{\text{sis}})/(S_d + S_d^{\text{sis}})$, and asymmetry in sister-size increments, $\alpha_\Delta = (\Delta - \Delta^{\text{sis}})/(\Delta + \Delta^{\text{sis}})$. These statistics are independent of a cell's position in the SAM and the time at which the data point was collected (Table S6). The medians and means of the ratios $(S_b + S_b^{\text{sis}})/(S_d + S_d^{\text{sis}}) \approx 0.5$ and $(S_b + S_b^{\text{sis}})/(\Delta + \Delta^{\text{sis}}) \approx 1$ indicate that, for each size metric, on average across the sample cells double in size over the cell cycle. These means and the slopes fitted to α_b vs. α_d and α_b vs. α_Δ were together used to estimate f , the parameter characterizing the mode of cell size regulation (SI Appendix, Text S3). The analysis includes all sisters born within 45 μm of O.

var.	med., mean $(S_b + S_b^{\text{sis}})/(S_d + S_d^{\text{sis}})$	med., mean $(S_b + S_b^{\text{sis}})/(\Delta + \Delta^{\text{sis}})$	α_b vs. α_d			α_b vs. α_Δ			α_b vs. α_f	
			sl., int.	R, p	est. f	sl., int.	R, p	est. f	sl., int.	R, p
V/μ_V^t	0.50, 0.50	1.01, 1.08	0.23, 0.0	$0.61, 10^{-43}$	0.46	-0.55, 0.0	$-0.64, 10^{-48}$	0.45	-0.71, 0.0	$-0.82, 10^{-103}$
V	0.48, 0.49	0.92, 1.00	0.23, 0.0	$0.61, 10^{-42}$	0.46	-0.48, 0.0	$-0.59, 10^{-40}$	0.52	-0.71, 0.0	$-0.82, 10^{-103}$
A	0.49, 0.49	0.95, 0.99	0.21, 0.0	$0.55, 10^{-34}$	0.42	-0.52, 0.0	$-0.62, 10^{-45}$	0.48	-1.03, 0.0	$-0.82, 10^{-102}$
A_{op}	0.48, 0.48	0.93, 0.97	0.23, 0.0	$0.46, 10^{-22}$	0.46	-0.48, 0.0	$-0.48, 10^{-25}$	0.52	-0.74, 0.0	$-0.77, 10^{-82}$
A_{ip}	0.50, 0.50	0.99, 1.05	0.29, 0.0	$0.69, 10^{-61}$	0.58	-0.39, 0.0	$-0.52, 10^{-29}$	0.61	-0.48, 0.0	$-0.72, 10^{-67}$
A_a	0.49, 0.49	0.97, 1.01	0.21, 0.0	$0.55, 10^{-34}$	0.42	-0.50, 0.0	$-0.47, 10^{-23}$	0.50	-1.3, 0.0	$-0.79, 10^{-91}$

Table S6: Cell-cycle statistics from volumes of all sister cells born within 45 μm of O ($N = 415$ sister pairs) are robust when the data were split for each SAM into the following categories: random splitting; cells born in the first/second half of the experiment (early times/late times); cells born closer/farther than the median distance from O (central zone/peripheral zone); cells born with larger/smaller volume than the median of L1 neighboring cells (large/small neighbor volume); cells born in the first 0-8 h light period/8-16 h light period/8 h dark period (born in morning/afternoon/dark); cells with a mother volume upon division that is larger/smaller than the median; cells born from symmetric/asymmetric divisions with $|\alpha_b| \leq 0.11$ or $|\alpha_b| > 0.11$. Statistics from all cells born within 30 μm of O ($N = 1013$ cells) pertaining to normalized birth volume versus normalized division volume (V_b/μ_V^t vs. V_d/μ_V^t) were robust when the data were split for each SAM into the following categories: cells born closer/farther than the median distance from O of cells within the 30- μm radius (inner central zone/outer central zone); cells born closer/farther than a 15- μm radius; cells born smaller/larger than the median birth volume; cells born with 5 or less/7 or more neighbors in the epidermal L1 cell layer; cells that divide with 5 or less/7 or more neighbors in the epidermal L1 cell layer; cells born in the first/second half of the experiment (early times/late times).

Data set split according to:	N	α_b vs. α_Δ (<45 μm)			α_b vs. α_T (<45 μm)	
		sl., int.	R, p	est. f	sl., int.	R, p
random	222	-0.45, 0.0	$-0.56, 10^{-19}$	0.55	-0.68, 0.0	$-0.79, 10^{-49}$
early times	189	-0.44, 0.0	$-0.38, 10^{-8}$	0.56	-0.67, 0.0	$-0.78, 10^{-40}$
late times	226	-0.51, 0.0	$-0.6, 10^{-23}$	0.49	-0.73, 0.0	$-0.82, 10^{-56}$
central zone (for 45- μm radius)	207	-0.50, 0.0	$-0.67, 10^{-30}$	0.50	-0.68, 0.0	$-0.86, 10^{-61}$
peripheral zone (for 45- μm radius)	208	-0.46, 0.0	$-0.52, 10^{-15}$	0.54	-0.73, 0.0	$-0.79, 10^{-45}$
large neighbor vol.	208	-0.45, 0.0	$-0.54, 10^{-17}$	0.55	-0.72, 0.0	$-0.78, 10^{-44}$
small neighbor vol.	207	-0.51, 0.0	$-0.64, 10^{-25}$	0.49	-0.70, 0.0	$-0.86, 10^{-63}$
born in morning	140	-0.39, 0.0	$-0.59, 10^{-14}$	0.61	-0.68, 0.0	$-0.68, 10^{-34}$
born in afternoon	148	-0.54, 0.0	$-0.6, 10^{-16}$	0.46	-0.71, 0.0	$-0.81, 10^{-35}$
born in dark	127	-0.51, 0.0	$-0.59, 10^{-13}$	0.49	-0.73, 0.0	$-0.84, 10^{-34}$
large mother vol.	208	-0.5, 0.0	$-0.54, 10^{-16}$	0.50	-0.74, 0.0	$-0.81, 10^{-48}$
small mother vol.	207	-0.47, 0.0	$-0.66, 10^{-26}$	0.53	-0.68, 0.0	$-0.84, 10^{-56}$
symmetric birth	174	-0.58, 0.0	$-0.23, 10^{-3}$	0.42	-0.85, 0.0	$-0.44, 10^{-9}$
asymmetric birth	241	-0.48, 0.0	$-0.69, 10^{-35}$	0.52	-0.7, 0.0	$-0.88, 10^{-77}$
	N	V_b/μ_V^t vs. V_d/μ_V^t (< 30 μm)		N	V_b/μ_b vs. V_d/μ_b (< 30 μm)	
		sl., int.	R, p		sl., int.	R, p
inner central zone (split 50:50 for 30- μm radius)	505	0.45, 1.2	$0.52, 10^{-36}$	505	0.44, 1.6	$0.55, 10^{-26}$
outer central zone (split 50:50 for 30- μm radius)	508	0.51, 1.1	$0.44, 10^{-25}$	508	0.44, 1.5	$0.36, 10^{-17}$
inner central zone (for 15- μm radius)	190	0.45, 1.2	$0.6, 10^{-19}$	190	0.43, 1.6	$0.49, 10^{-13}$
outer central zone (for 15- μm radius)	823	0.49, 1.2	$0.45, 10^{-42}$	823	0.46, 1.5	$0.39, 10^{-31}$
large birth vol.	508	0.63, 1.0	$0.45, 10^{-26}$	508	0.66, 1.1	$0.42, 10^{-22}$

small birth vol.	505	0.49, 1.2	$0.32, 10^{-13}$	505	0.42, 2.0	$0.20, 10^{-6}$
num. neighbors at birth ≤ 5	383	0.43, 1.2	$0.34, 10^{-11}$	383	0.39, 2.0	$0.27, 10^{-7}$
num. neighbors at birth ≥ 7	183	0.59, 1.0	$0.47, 10^{-11}$	183	0.63, 1.0	$0.47, 10^{-11}$
num. neighbors at division ≤ 6	346	0.54, 1.1	$0.46, 10^{-19}$	346	0.45, 1.5	$0.34, 10^{-10}$
num. neighbors at division ≥ 8	191	0.47, 1.2	$0.53, 10^{-15}$	191	0.49, 1.5	$0.47, 10^{-11}$
early times	439	0.52, 1.2	$0.50, 10^{-28}$	439	0.49, 1.7	$0.38, 10^{-16}$
late times	574	0.47, 1.1	$0.47, 10^{-32}$	574	0.48, 1.36	$0.46, 10^{-30}$

Table S7: The power-law scalings of volume with inner periclinal wall area and anticlinal wall area are $V \sim A_{ip}$ and $V \sim A_a^{0.5}$, as expected for L1 cells in the central zone given that these cells grow within the plane of the epidermis. The outer periclinal wall area scaled with volume like $V \sim A_{op}^{0.8}$ and the total wall area scaled like $V \sim A^{0.66}$. Each entry displays the least-square linear fitted slope (Pearson's R , p).

SAM	$\log(V)$ vs. $\log(A)$	$\log(V)$ vs. $\log(A_a)$	$\log(V)$ vs. $\log(A_{ip})$	$\log(V)$ vs. $\log(A_{op})$
#1	0.67 (0.99, 0.0)	0.52 (0.92, 0.0)	1.03 (0.85, 0.0)	0.77 (0.75, 0.0)
#2	0.66 (0.99, 0.0)	0.55 (0.91, 0.0)	0.98 (0.89, 0.0)	0.79 (0.88, 0.0)
#3	0.66 (1.0, 0.0)	0.51 (0.91, 0.0)	1.02 (0.92, 0.0)	0.82 (0.9, 0.0)
#4	0.67 (0.99, 0.0)	0.53 (0.9, 0.0)	0.98 (0.89, 0.0)	0.82 (0.82, 0.0)
#5	0.66 (0.99, 0.0)	0.51 (0.85, 0.0)	1.0 (0.88, 0.0)	0.88 (0.82, 0.0)
#6	0.67 (1.0, 0.0)	0.53 (0.86, 0.0)	0.88 (0.88, 0.0)	0.85 (0.89, 0.0)

Table S8: Sister cells generated by an asymmetric division grow at different relative rates with the smaller cell growing at a faster relative rate. Left two columns: the proportion of the size metric S inherited from the mother cell upon division, quantified by the value of $\alpha_b = (S_b - S_b^{sis})/(S_b + S_b^{sis})$ at birth, is strongly negatively correlated with the relative growth rate g_{rel} divided by its mean (α_b vs. $g_{rel}/\text{mean}(g_{rel})$). If sisters grew at the same relative rate, there would be no correlation. Right four columns: among cells born from a symmetric division (similar volumes between sisters; $|(V_b - V_b^{sis})/(V_b + V_b^{sis})| \leq 0.11$, representing ~50% of data), for all size metrics there was no significant dependence of relative growth rate on either cell birth volume ($p > 0.01$) or the relative volume of their non-sister neighbors ($p > 0.01$). In contrast, for cells of intermediate birth volumes ($|V_b/\text{mean}(V_b) - 1| \leq 0.16$, representing ~50% of the data) and with non-sister neighbors of a similar volume ($|(V - V^{ns-neigh})/(V + V^{ns-neigh})| \leq 0.11$, representing ~50% of the data), the relative growth rates of volume, outer periclinal, and inner periclinal wall areas did depend on mother-cell asymmetric division (Fig. S20). Data points include relative growth rates for all cells born $<30 \mu\text{m}$ from O ($N = 393$ sister pairs).

	α_b vs. $g_{\text{rel}}/\text{mean}(g_{\text{rel}})$		Kruskal-Wallis H-test (H, p) for g_{rel} for the given size metric and group			
			~50% data with symmetric division of mother cell		grouped by asymmetric division of mother cell	
var. S	sl., int.	R, p	grouped by cell vol. at birth	grouped by non- sister neighbor vols.	~50% data with intermediate vols. at birth	~50% data with vols. similar to non-sister neighbors
V/μ_V^t	-0.50, 0.99	-0.36, 10^{-24}	3.1, 0.4	5.5, 0.1	$73, 10^{-15}$	$43, 10^{-9}$
V	-0.34, 0.99	-0.30, 10^{-17}	4.6, 0.2	8.5, 0.04	$18, 4.10^{-4}$	$12, 6.10^{-3}$
A	-0.45, 0.98	-0.26, 10^{-13}	3.7, 0.3	4.2, 0.2	8.9, 0.03	8.0, 0.04
A_{op}	-0.38, 0.99	-0.25, 10^{-12}	14, 0.003	9.4, 0.02	$49, 10^{-10}$	$49, 10^{-10}$
A_{ip}	-0.56, 0.98	-0.19, 10^{-7}	2.4, 0.5	7.0, 0.07	$51, 10^{-10}$	$58, 10^{-12}$
A_a	-0.53, 1.0	-0.16, 10^{-5}	3.0, 0.4	7.6, 0.06	1.1, 0.8	0.81, 0.9

Table S9: Simulations of cell-autonomous size and growth regulation recapitulate statistics. Simulations of n_{model} cell cycles, where n_{model} was chosen to approximately match the sample size of our data, assuming cell-autonomous regulation of division size according to Eq. (1) and growth at a constant relative rate over the cell cycle that depended linearly on the fraction of volume inherited from the mother cell at birth. 1000 instances of the simulation were used to compute median values of various statistics and 90% confidence intervals. Simulation parameters were extracted from experimental data ($f = 0.48$, $g_{\text{asym}} = 0.43$, $\sigma = 0.227$, $\sigma_a = 0.105$, correspond to medians computed by bootstrapping; *SI Appendix, Text S3*). The experimental least-square linear fitted slopes (sl.), intercepts (int.), Pearson correlation coefficients (R), and p -values (p) were also estimated by medians from bootstrapping. There are no free fitting parameters, and the simulation predictions are in close agreement with our experimental data.

	σ_b, σ_d	normalized vol.: V_b/μ_V^t vs. $V_d/\mu_V^t/\text{mean}(V_b/\mu_V^t)$ ($n_{\text{model}} = 1000$)	
		sl., int.	R, p
<i>simulation</i>	(0.25, [0.24, 0.26]), (0.13, [0.12, 0.13])	(0.48, [0.43, 0.53]), (1.52, [1.47, 1.57])	(0.47, [0.42, 0.51]), (10^{-56} , [10^{-53} , 10^{-34}])
<i>experiments</i>	0.25, 0.13	0.48, 1.43	0.47, 10^{-57}
		α_b vs. α_d ($n_{\text{model}} = 800$)	
		sl., int.	R, p
<i>simulation</i>	(0.24, [0.21, 0.27]), (0.00, [0.00, 0.00])	(0.53, [0.48, 0.58]), (10^{-30} , [10^{-37} , 10^{-23}])	
<i>experiments</i>	0.23, 0.00	0.61, 10^{-43}	
		α_b vs. α_T ($n_{\text{model}} = 800$)	
		sl., int.	R, p
<i>simulation</i>	(-0.69, [-0.75, -0.65]), (0.0, [-0.01, 0.01])	(-0.75, [-0.78, -0.70]), (10^{-72} , [10^{-82} , 10^{-61}])	
<i>experiments</i>	-0.71, 0.0	-0.82, 10^{-102}	
		normalized vol.: α_b vs. $V_b/\mu_V^t/\text{mean}(V_b/\mu_V^t)$ ($n_{\text{model}} = 800$)	
		sl., int.	R, p
<i>simulation</i>	(1.00, [0.95, 1.05]), (1.00, [0.99, 1.01])	(0.85, [0.82, 0.87]), (10^{-120} , [10^{-125} , 10^{-100}])	
<i>experiments</i>	0.99, 1.00	0.87, 10^{-245}	

Table S10. Correction factors strongly reduce the bias and noise in measurements of cell-size metrics. Bias and noise resulted from plant stem growth/upward movement of SAMs during image acquisition, which produced artificial stretching of cells in the z-direction by the factor given in the table for each time-point; see also Fig. S24. Correction factors were computed by comparing rapidly acquired low-z-resolution confocal stacks with slowly acquired high-z-resolution confocal stacks, with the latter being used for segmentation (Materials and Methods).

Time-point (h)	SAM #1	SAM #2	SAM #3	SAM #4	SAM #5	SAM #6
0	1.07	1.41	1.19	1.06	1.04	1.00
4	2.77	1.17	1.58	1.32	1.11	0.98
8	1.47	1.13	1.93	1.08	1.08	1.06
12	1.23	1.10	2.21	1.08	1.11	1.02
16	1.17	1.08	1.17	1.04	1.06	1.06
20	1.20	1.09	1.27	1.04	1.01	1.01
24	1.33	1.43	1.22	1.04	1.07	1.07
28	1.33	1.40	1.59	1.07	1.07	1.01
32	1.37	1.32	1.32	1.19	1.21	1.24
36	1.26	1.19	1.47	1.54	1.30	1.26
40	1.23	1.32	1.17	1.32	1.43	1.28
44	1.23	1.13	1.64	1.24	1.58	1.32
48	1.22	1.22	1.20	1.28	1.30	1.40
52	1.00	1.13	1.26	1.43	1.54	1.54
56	1.15	1.28	1.19	1.80	1.78	1.58
60	1.28	1.30	1.28	1.80	1.52	1.41
64	1.36	1.37	1.32	1.53	1.84	1.30
68	1.30	1.27	1.35	1.46	1.64	1.56
72	1.12	1.40	1.17	1.87	1.74	1.22
76	1.06	1.08	1.13	1.39	1.47	1.24
80				1.06	1.02	1.04
84				2.32	1.37	1.50

Other Supplemental Material:

External Database S1. The processed confocal z-stacks, segmented z-stacks, and cell quantification and tracking data files can be downloaded from Cambridge University D-space Repository (<https://www.repository.cam.ac.uk/>).